Innovations in Urban Noise Mapping

Innovaties in stadsgeluidsbelastingskaarten

Weigang Wei

Promotoren: prof. dr. ir. D. Botteldooren, prof. dr. ir. T. Van Renterghem
Proefschrift ingediend tot het behalen van de graad van
Doctor in de Ingenieurswetenschappen

Vakgroep Informatietechnologie
Voorzitter: prof. dr. ir. D. De Zutter
Faculteit Ingenieurswetenschappen en Architectuur
Academiejaar 2014 - 2015

UNIVERSITEIT
GENT

ISBN 978-90-8578-771-6
NUR 910, 950
Wettelijk depot: D/2015/10.500/15

Universiteit Gent
Faculteit Ingenieurswetenschappen en Architectuur
Vakgroep Informatietechnologie

Promotoren:

Prof. Dr. Ir. Dick Botteldooren
Prof. Dr. Ir. Timothy Van Renterghem

Examencommissie:

Prof. Dr. Ir. Luc Taerwe (voorzitter)	Universiteit Gent
Prof. Dr. Ir. Gaetano Licitra	ARPAT and University of Pisa
Prof. Dr. Ir. Maarten Hornikx	Eindhoven University of Technology
Prof. Dr. Ir. Kristiaan Neyts	Universiteit Gent
Prof. Dr. Ir. Dries Vande Ginste (secretaris)	Universiteit Gent
Prof. Dr. Ir. Bert De Coensel	Universiteit Gent
Prof. Dr. Ir. Timothy Van Renterghem (promotor)	Universiteit Gent
Prof. Dr. Ir. Dick Botteldooren (promotor)	Universiteit Gent

Universiteit Gent
Faculteit Ingenieurswetenschappen en Architectuur
Vakgroep Informatietechnologie
Sint-Pietersnieuwstraat 41, B-9000 Gent, België

Tel.: +32-9-264.99.95
Fax.: +32-9-264.99.69

Proefschrift tot het behalen van de graad van
Doctor in de Ingenieurswetenschappen
Academiejaar 2014-2015

Dankwoord

How time flies! Four-year's study is coming to its end. Without the great support from my promoters and friends, I would not finish it.

First of all, I would like to express my sincere respect and gratitude to my promoter prof. ir. dr. Dick Botteldooren. He helped me to choose this interesting topic and gave me clear and helpful guides. It was my great honour and luck to have the chance to learn and work together with professor Botteldooren. His brilliant mind would continue guiding my attitude towards research and my career.

Moreover, I would also express my great gratitude to my co-promoter prof. ir. dr, Timothy Van Renterghem. He is an excellent acoustician and gives me a lot of nice and helpful suggestions to my work. Thanks to post-doc Annelies Bockstael and prof. ir. dr Bert De Coensel. They helped me with my first publication which was a fantastic first step.

Furthermore, many thanks to my friends in the acoustics group, Gemma, Mimma, Luc, Pieter, Lei, Xiaodong, Samuel, Damiano, Michiel, Karlo, Kang and Vincent. They are the key part of the friendly working environment. Many thanks to ir. dr. Huaxin Wang. I will benefit from his wisdom and courage for ever. Thanks to many other friends, my family and my family-in-law.

Finally, I would like to express my endless and invaluable gratitude to my wife Mrs Lei Zhao. She gave me extremely patience and great support for my PhD. Without that, I cannot imagine how can I finish it.

Weigang Wei
Gent, December 10th 2014

Table of Contents

List of Acronyms

A_{diffr}	Attenuation caused by diffraction and reflections over buildings [dB]
A_{free}	3 D free field divergence [dB]
A_{bar}	Attenuation caused by a thick barrier including the presence of the ground [dB]
$A_{bar,flat}$	Attenuation of a rigid thick barrier with flat roof including the presence of the ground [dB]
$A_{bar,flat,0}$	Attenuation from source to receiver of a rigid thick barrier with flat roof excluding the ground [dB]
$A_{bar,flat,1}$	Attenuation from source to image receiver of a rigid thick barrier with flat roof excluding the ground [dB]
$A_{bar,flat,2}$	Attenuation from image source to receiver of a rigid thick barrier with flat roof excluding the ground [dB]
$A_{bar,flat,3}$	Attenuation from image source to image receiver of a rigid thick barrier with flat roof excluding the ground [dB]
$A_{bar,roof}$	Correction for roof shape [dB]
A_{can}	Attenuation caused by reflections inside a canyon [dB]
A_{inter}	Attenuation caused by intermediate canyons [dB]
a	The number of image sources
b	The number of image receivers
$C(x), S(x)$	Fresnel integrals
D	Diffraction function
FDTD	Finite-Difference Time Domain method
GIS	Geographic Information System
h_r	Receiver height
h_s	Source height
H_s	Height of source-canyon building
H_i	Height of intermediate building
H_r	Height of receiver-canyon building
i	Equals $\sqrt{-1}$ indicating the imaginary part
j	A local index indicating the change of diffraction edges, for example $W_{j,j+1}$ is the distance from the j^{th} edge to $(j+1)^{th}$ edge
L	Length of diffraction path

L_{pb}	Background sound level [dB]
L_{pdb}	Background sound level excluding turbulent scattering [dB]
$L_{p,scatter}$	Sound pressure level caused by scattering [dB]
l	The number of diffraction edge, for example, D_l indicates the diffraction function at the l^{th} edge
$p_{a,b}$	Sound pressure caused by source a at receiver b
R	Distance from source to receiver
r_s	Distance from the source to the closest diffraction edge
r_r	Distance from the receiver to the closest diffraction edge
$r_{s,l}$	Distance of the propagation path from the source to the l^{th} diffraction edge
$r_{r,l}$	Distance of the propagation path from the l^{th} diffraction edge to the receiver. The receiver can be the real receiver or can be the next diffraction edge
$r_{a,s}$	Distance of the a^{th} image source to the closest diffraction edge
$r_{b,r}$	Distance of the b^{th} image receiver to the closest diffraction edge
W_s	Width of the source canyon
W	Width of the intermediate building, or the width of a thick barrier, or the width between two diffraction edges
W_r	Width of the receiver canyon
$W_{i,j}$	Width of between diffraction edge i and j
β	The angle of the diffraction wedge, such as β_S is the angle of the diffraction edge closest to the source and β_l is the angle of the l^{th} diffraction edge
θ_s	The angle from the right face of the first diffraction edge to the connecting line from the source to the diffraction edge
θ_r	The angle from the right face of the last diffraction edge to the connecting line from the receiver to the diffraction edge
$\theta_{a,s}$	The angle from the right face of the first diffraction edge to the connecting line from the a^{th} image source to the diffraction edge
$\theta_{b,r}$	The angle from the right face of the last diffraction edge to the connecting line from the b^{th} image receiver to the diffraction edge
$\theta_{s,l}$	The angle from the right face of the l^{th} diffraction edge to the connecting line from the source to the diffraction edge
$\theta_{r,l}$	The angle from the right face of the l^{th} diffraction edge to the connecting line from the receiver to the diffraction edge

θ_{l+}	$\theta_{s,l} + \theta_{r,l}$
θ_{l-}	$\theta_{s,l} - \theta_{r,l}$
λ	Wave length

Nederlandse samenvatting

–Summary in Dutch–

Lawaai heeft reeds eeuwen een negatieve invloed op de levenskwaliteit van de bevolking. Onder de negatieve effecten van omgevingslawaai vinden we naast hinder ook slaapverstoring en een reductie van werk- en leerefficintie. Op lange termijn kunnen hypertensie en ischemische hartziekte optreden. Verkeer vormt in Europa de grootste bron van lawaai en diverse toekomstverkenningen wijzen erop dat dit verkeer de komende decennia nog sterk zal toenemen. Ondanks de reductie van de geluidsemissie per voertuig kan men dan ook verwachten dat de negatieve effecten van geluid nog zullen toenemen gedurende de komende 20 jaar. Om een effectief en efficint beleid te kunnen voeren rond (verkeers)lawaai zijn accurate voorspellingsmethodes nodig voor zowel geluidsniveaus als effecten van geluid.

Sinds enkele tientallen jaren hebben verschillende onderzoekers numerieke methodes gezocht om het geluidsklimaat in een stad in kaart te brengen. Deze berekening wordt ook vandaag nog in belangrijke mate beperkt door de beschikbare computerkracht. Bij directe oplossing van de golfvergelijking worden het interessedomein of de randen ervan opgedeeld in voldoend kleine cellen, typisch kleiner dan de interessante golflengte. De berekening van de geluidsdruk in deze cellen vraagt zoveel cpu-tijd dat methodes gebaseerd op het rechtstreeks oplossen van de golfvergelijking onbruikbaar zijn voor het voorspellen van geluidsniveaus in een volledige stad of stadsdeel. Zogenoemde engineering modellen zoals ISO9613, Harmonoise/Imagine en CNOSSOS werden ontwikkeld als een balans tussen nauwkeurigheid en berekeningsefficintie. Bronnen van verkeersgeluid worden opgesplitst in puntbronnen of lijnbronnen. De verzwakking van het geluid tussen deze bronnen en de waarnemingsposities wordt berekend op basis van geometrische relaties tussen bronnen, waarnemers en objecten. Het bepalen van deze geometrische informatie is doorgaans veel sneller dan berekeningen op basis van een rooster van cellen. Hierdoor kunnen berekeningen op het schaalniveau van de stad uitgevoerd worden.

Sinds 2002 legt de Europese Richtlijn Omgevingsgeluid aan de lidstaten op om vijfjaarlijks geluidskaarten op te stellen. Onder impuls van deze verhoogde geluidskaart-activiteit werden een aantal meetcampagnes opgezet om de nauwkeurigheid van de berekende kaarten te verifiren. Voor het directe geluidsveld komen berekeningen en metingen doorgaans vrij goed overeen. In afgeschermde zones onderschatten de berekeningen het geluidsniveau meestal. In het eerste hoofdstuk van dit doctoraat komt met een oplossing voor deze onderschatting. De onderschatting

is vooral het gevolg van de verwaarlozing van meervoudige reflecties tussen gebouwen. Alhoewel engineering modellen veel sneller rekenen dan golfmodellen, blijft de berekening van een geluidskaart voor een volledige stad een rekenintensieve aangelegenheid. Daarom kiest men er meestal voor om het aantal reflecties te beperken tot 1 of 2. De rekenlast neemt immers meer dan lineair toe met het aantal reflecties. Om hieraan tegemoet te komen en de onderschatting te vermijden zonder significante toename van de vereiste cpu-tijd, werd in dit doctoraat een nieuw engineering model ontwikkeld: het QSIDE model, genoemd naar het Europese project waarbinnen dit onderzoek viel.
Het QSIDE model steunt op de vereenvoudiging van de formules die de diffractie over brede schermen beschrijven. Met deze vereenvoudigde formules en enkele bijkomende veronderstellingen kunnen de bijdragen van alle spiegelbronnen tot het geluidsniveau in de afgeschermde ruimte expliciet gesommeerd worden tot de Hurwitz-Lerch transcendent. Deze sommatie wordt bekomen voor perfect vlakke en evenwijdige gevels. In werkelijkheid reflecteren gevels het geluid deels diffuus. Daarom worden in de formules een aantal te fitten cofficinten toegevoegd die op basis van een groot aantal eindige differentie tijdsdomein (FDTD) simulaties. Een database van FDTD berekeningsresultaten voor typische afmetingen van gebouwen en breedte van straten werd hiervoor doorgerekend. Het finale QSIDE model werd gevalideerd aan de hand van een langdurige meetcampagne in Gent.
Het QSIDE model gaat voor het kwantificeren van het effect van de straat canyon uit van een vlak dak en introduceert een afzonderlijke correctie voor dakvorm en tussenliggende canyons. Om de onzekerheden ten gevolge van deze benadering te reduceren werd in een volgend hoofdstuk van dit doctoraat een veralgemeende functie voor meervoudige diffractie afgeleid. Deze formulering werd gevalideerd door vergelijking met meer gedetailleerde analytische modellen en eindige differentie tijdsdomein simulaties. Dit hoofdstuk introduceert ook een verfijnde benadering in het geval de gebouwen aan beide zijden van de straat significant in hoogte verschillen. Het verschil tussen de voorgestelde benaderingen en FDTD simulaties zijn beperkt tot 1.5 dB voor de meeste frequenties en de meeste ontvangerposities en weg van de lijn die zichtbare en onzichtbare zones scheidt.
Ondanks de hiervoor vermelde verbeteringen kunnen strategische geluidskaarten nog significant afwijken van de werkelijkheid omwille van de onzekerheid op bronvermogens, propagatiecondities, additionele niet gekarteerde bronnen, en vooral de temporele variaties hierin. Daarenboven wijzen studies naar geluidslandschappen, slaapverstoring en andere effecten van geluid op het belang van temporele fluctuaties zowel op de tijdschaal van de dag (schouderuren voor slaap) als op de kortere tijdschaal (L_{10} en L_{90} in geluidshindermodellen). Om deze temporele effecten mee te nemen, wordt de dynamische geluidskaart in dit doctoraat gentroduceerd. De term “dynamische geluidskaart” refereert naar een geluidskaart die in korte tijdstappen up-to-date gebracht wordt (b.v. om de 15 minuten) op basis van metingen in een dicht, maar beperkt netwerk van sensoren. Complementair aan energie gebaseerde indicatoren zoals LAeq kan de dynamische geluidskaart ook andere indicatoren bevatten die relevant zijn voor de beoordeling van effecten op de mens zoals de statistische geluidsniveaus L_{10} en L_{90}.

De methodologie die in dit doctoraat voorgesteld wordt voor het berekenen van dynamische geluidskaarten gaat uit van een vrij goede theoretische kennis van bronvermogens en propagatie. Op beide termen worden vervolgens kleine correcties voorzien die op basis van het afstemmen van kaart en metingen in een beperkt aantal locaties worden bepaald. In een stedelijk gebied vind je letterlijk duizenden geluidsbronnen. Het spreekt voor zich dat al deze bronnen en hun propagatie bijsturen tot een ondergedetermineerd probleem aanleiding geeft. Daarom wordt het aantal vrijheidsgraden gereduceerd door groeperen van bronnen en propagatiepaden. Binnen elke categorie wordt verondersteld dat de correcties dezelfde zijn. Het aantal vrijheidsgraden wordt hierdoor beperkt tot het aantal categorien van bronnen en propagatiepaden eerder dan tot het aantal bronnen en propagatiepaden. Het probleem wordt hierdoor oplosbaar en een gradueel adaptief systeem uit de signaalverwerking, het LMS algorithme, wordt gebruikt om de correctietermen te bepalen. Als gevalstudie wordt deze methodiek toegepast op het district Katendrecht in Rotterdam. Hieruit bleek dat convergentie bekomen wordt en dat ook in een aantal onafhankelijke validatiepunten de correspondentie tussen kaart en metingen in 75% van de observatieintervallen verbetert. Ook de voorspelling van statistische niveaus zoals L_{10} en L_{90} verbetert door introductie van de dynamische geluidskaart.

Samengevat zijn in dit doctoraat een aantal innovaties op het vlak van het opstellen van geluidskaarten gentroduceerd die moeten toelaten enerzijds strategische geluidskaarten efficinter en nauwkeuriger op te stellen, anderzijds beter rekening te houden met dynamische aspecten van het geluidsklimaat. Het achtergrondmodel dat via drie afzonderlijke bijdragen de predictie van geluidsniveaus in afgeschermde zones nauwkeuriger bepaalt kan op een vlotte manier gecombineerd worden met de klassieke benadering en zou zodoende aan de nieuwe CNOSSOS methodologie toegevoegd kunnen worden. Dynamisch geluidskarteren opent nieuwe mogelijkheden voor interpolatie tussen geluidsmonitoringsstations en zal een essentieel onderdeel vormen van een state-of-the-art “internet of sound observatories” dat deel kan uitmaken van de toekomstige slimme stad.

English summary

For centuries, noise has resulted in a negative impact on the quality of life of inhabitants, such as sleep disturbance, cardiovascular diseases and the cognitive impairment in children. Surveys in Europe show that the number of vehicles, as the most prominent noise sources, will not decrease. Despite the reduction of the noise emission per vehicle, one can expect that the negative effects of noise will hardly improve within the next 20 years. In order to conduct an effective and efficient policy on road traffic noise, accurate prediction methods are therefore required, at least to estimate the impact.

For several decades, researchers have been developing numerical methods to map sound pressure levels in a city. The direct solution of the wave equation, either solved in time domain, such as the finite-difference time-domain method, or in frequency domain, such as the finite element method, needs to divide the calculation region into a large number of very small cells. The calculation of the sound pressure in these cells requires so much CPU time that are incapable of predicting noise levels in an entire city or district. Therefore, some engineering-type models such as ISO9613, HARMONOISE/IMAGINE and CNOSSOS-EU have been developed as a balance between accuracy and computational efficiency. In these engineering models, traffic noise sources are represented by point sources or line sources. Reflections and diffraction in the horizontal plane can be calculate by ray/beam tracing method, whilst the insertion loss of an obstacle in the vertical plane can be calculated based on the geometrical relationship between the sources and observers. Such methods are able to produce city-wide maps.

Since 2002, the European Noise Directive has required its member states to make noise maps every 5 years. Spurred by this increased activities of noise mapping, several campaigns were launched to verify the accuracy of the calculated maps. For the direct sound field, calculations and measurements usually match well. However, calculations often largely underestimate the noise in shielded areas. The underestimation is mainly due to the insufficiently consideration of multiple reflections between buildings. Although engineering models run much faster than wave-based models, the calculation of a noise map for an entire city is still a computational intensive task. The number of reflections is therefore usually limited to 1 or 2. To address these issues and avoid such underestimation without a significant increase in the required CPU time, a general model for background noise mapping was developed in this dissertation.

The background noise model is based on the simplification of formulas describing diffraction over wide barriers. With these simplified formulas and some additional

assumptions, contributions from all the image sources to the noise levels in the shielded area can be summed explicitly by the Hurwitz-Lerch transcendent. This summation is obtained for perfectly flat and parallel walls. In reality, reflected sounds from façades are partly diffuse. Therefore, some coefficients are added to the formulas to include this effect as well. These coefficients are based on a large number of finite-difference time-domain (FDTD) simulations. A database of FDTD calculations for typical building heights and streets widths was build-up for this purpose. The final background noise model was validated by a long-term measurement campaign in Ghent.

The background noise model for quantifying the effect of street canyons is extracted based on flat roofs and introduces separate adjustments for the presence of intermediate canyons and roof shapes. To reduce the uncertainties resulting from assuming the flat roofs, a generalized form for multiple diffraction was derived afterwards. This formulation has been validated by comparison with more detailed analytical models and FDTD simulations. Additionally, a sophisticated approach in case the buildings on both sides of the street significantly differ in heights was presented. The difference between the proposed approaches and FDTD simulations are limited to 1.5 dB for most of the frequencies and most of the receiver positions, on condition that they are far away from the line separating visible and invisible zones.

Despite the improvements mentioned above, strategic noise maps can still be significantly different from live measurement because of the uncertainties in source power, propagation and additional non-traffic related sources, as well as the neglect of the temporal variations. Furthermore, studies of soundscape, sleep disturbance and other effects of noise on humans strongly depend on the temporal fluctuations both on a daily basis and on a shorter time scale percentile levels (such as L_{10} and L_{90} in noise measurement). To predict short-term noise levels and take these temporal effects into consideration, the concept of a “dynamic noise map” was introduced in this thesis. The term “dynamic noise map” is used to refer to a noise map that is updated in short time intervals (e.g. every 15 minutes) based on measurements made in a measurement network of noise sensors. As a complement to an energy-based noise level indicator as L_{Aeq}, the proposed methodology can also include other indicators that could be relevant for the evaluation of the effect of noise on people such as the percentile levels L_{10} and L_{90}.

The proposed methodology to calculate dynamic noise maps assumes that there is a reasonable good theoretical approximation of source power and propagation. Based on this assumption, the offset from the modelled sources to the true sources and the offset from modelled attenuation to the true attenuation can be supposed as only minor adjustments that are determined by matching the calculated indicators and measurements in a limited number of locations. When mapping the noise in an urban area, there are usually thousands of sources. Clearly, adjusting all of these sources and their propagation paths makes the problem strongly under-determined. Therefore, the number of degrees of freedom is reduced by grouping sources and propagation paths into a limited number of categories. Within each category, it is assumed that the corrections are the same. The number of degrees of freedom is

thus limited to the number of categories of sources and propagation paths rather than the number of sources and propagation paths themselves. By this, the underdetermined problem becomes determined. A gradually fitting system adapted from the signal processing field, the LMS algorithm, was used to determine these correction terms. By a case study, this method was applied to the district Katendrecht in Rotterdam, the Netherlands. The results of the case study showed that convergence was obtained and the equivalent sound pressure levels between calculations and measurements in the independent validation points were improved more than 75% of the observation intervals. The prediction of percentile levels, L_{10} and L_{90}, were also improved by introducing the concept of dynamic sound updating.

In summary, this doctoral thesis presents some innovations in noise mapping techniques helping on one hand to calculate strategic noise maps efficiently and accurately, and on the other hand to take the dynamic aspects of the sound environment into consideration. The background model, improving predictions of noise levels in shielded areas, can be combined smoothly with the traditional noise mapping approach and could thus be added to e.g. the new CNOSSOS methodology. Dynamic sound mapping provides interpolation strategies between noise monitoring stations and could form an essential part of a state-of-the-art “website of sound observatories” that could be part of the smart city in the future.

1

Introduction

1.1 Noise situation and strategic noise mapping

The industrial revolution of vehicles in the 20^{th} century brought people convenience together with noise. According to [1, 2, 3], 20% of the European residents are exposed to noise over 65 dB(A) during day time and more than 30% are exposed to noise over 55 dB(A) at night. The major contribution to these noise levels comes from the traffic. The number of vehicles in Europe would still increase with 31% and 17% for light-duty vehicles and heavy-duty vehicles when comparing 2030 data of 2010 [4]. Although electronic cars have quieter engines than the traditional cars with internal combustion engines, the purchased traditional vehicles would still be travelling on the street. Besides, the electronic vehicles still produce rolling noise. As a result, noise pollution from road traffic sources would still be very serious in the near future.

Noise pollution jeopardises the quality of life in many aspects [5], such as sleep disturbance [6], noise annoyance [7, 8, 9] and even risks for cardiovascular diseases [10]. Not only high level noise, but also traffic noise below $55\mathrm{dB(A)}$ could cause changes in the endocrine system [11, 12] and may further cause health risks [13] (page 67). For long-term noise exposure, the situation is even worse than the short-term dose-response relation [11]. A study showed that morning tiredness is associated with long-term traffic noise exposure [14]. Many studies also show that long-term traffic noise is strongly related to sleep disturbance [15, 16] and may lead to cardiovascular risks [17, 18, 19, 20].

To have a quiet and sustainable environment, the European Council has started their noise policy since 1993 [21]. Member states have made their noise policies even earlier. From 2002, the European Environmental Noise Directive called for noise maps and action plans for agglomerations, major roads, railways and airports every 5 years to identify the environmental problems and develop a long-term EU strategy.

A strategic noise map should provide an overall noise prediction in a long term of an area employing the major indicators L_{den}, L_{day}, $L_{evening}$ and L_{night}. Till now, two rounds of noise mapping have been performed and prediction accuracies at e.g. completely shielded urban locations were shown to strongly deviate from measurements. Additionally, not only the strategic noise mapping is interesting, but also an increasing demands for short term predictions rise for noise annoyance studies and sleep disturbance studies. These problems are the main motivation of this research work.

1.2 Numerical approaches for noise mapping

To predict the urban noise climate, numerical simulations are widely used. The approaches based on direct solution of wave equations either in time domain such as FDTD (finite-difference time-domain) [22, 23, 24] or in frequency domain such as FEM (finite element method) [25] require densely divided grids to get satisfactory accuracy. For computers nowadays, these approaches need too much CPU time to calculate a noise map in a city. Therefore, some engineering models such as ISO9613 [26], HARMONOISE/IMAGINE [27, 28], NMPB2008 [29] and CNOSSOS-EU [30], were developed to balance the accuracy and efficiency. Based on these engineering models, calculating a noise map with a city size is possible.

These engineering models are mainly based on models of sources, propagation and digital terrain. The digital terrain model is used to determine the geometrical relation between sources and receivers. The predicted sound pressure level at a receiver position from a source is generally described as:

$$L_p = L_W - A$$

where L_p is the sound pressure level at the receiver position, L_W is the source power level of the source and A is the attenuation. A may consist the attenuation from the ground, barriers and geometrical divergence etc. If more than one source propagates to the receiver, the total sound pressure level then is the sum of contributions from all these sources. The source and propagation models often differ considerably from each other. In chapter 2 and chapter 3, the propagation models are analysed in detail. In the appendix, a comparison between different source models are listed. The same relation among source power level, attenuation and the sound pressure level at receivers, as stated in the above equation, are also applied to the study in the following chapters.

In noise mapping, the contributions from many sources to a receiver are usually separated in horizontal plane and vertical plane. In the horizontal plane, reflections and diffraction from sources to a receiver are traced by sound rays or beams. Whilst, the contributions in the vertical plane are quantified by twisted sections linking a source to the receiver. The buildings or barriers in the section are assigned heights directly without considering the roof shapes in the vertical dimension. The total sound pressure level at the receiver then should include all these contributions. This approach, 2.5D method, is widely used in strategic noise mapping.

Many case studies of the noise maps have been calculated around the European Union [31, 32, 33] and even some Asian [34, 35] and South America countries [36] follow the EU to make noise maps. Meanwhile some measurement campaigns were also carried out [37, 38, 39]. Compared to measurements, the noise levels at the most exposed façades are usually predicted in a satisfactory way, however, for the completely shielded yards, the predicted noise level are usually lower than the measurement [40, 41].

The underestimation is mainly due to the neglect of multiple reflections between parallel buildings and the contribution of distant sources. This is done to prevent the calculation time increasing tremendously. A reflection can be treated as sound coming from a mirror source. The number of mirror sources increases exponentially as the number of reflections due to the surrounded reflectors. Additionally, the sound ray may reach a receiver that could not be reached without this additional reflection. The difficulty of detecting the geometrical relations between images sources and the receiver would also increase considerably. Therefore, the reflection number is often set to 1 in noise mapping activities. The underestimation caused by using 1 reflection compared to multiple reflections is often more than 5 dB in typical urban geometrical conditions. A comparison figure was presented in chapter 3 and similar comparison can also be found in [42].

Due to the above mentioned reasons, it is very useful to develop an engineering model including multiple reflections and diffraction in a concise and explicit term. In chapter 2, such an engineering model was derived based on theoretical analysis and some parameters are then fitted from FDTD simulations for street canyon propagations to correct for façade roughness and diffusion. This model includes all the reflections in one term and then the total increased simulation time is independent from the number of reflections in the vertical sections.

Moreover, increasing the radius of the affected sources also considerably drags down the calculation efficiency. To save calculating time, most of the distant sources are excluded in classical noise mapping. However, all distant sources together can still strongly affect the background levels especially in places that are completely shielded from direct sound, although the contribution of a single distant source is often small. Therefore, the concept of background noise mapping was introduced in chapter 2 to include the contribution of distant sources.

1.3 Urban background noise mapping

Background noise mapping is useful to determine whether a quiet side is present. The European Environmental Noise Directive (END) specifies that a quiet side is present if the noise level at the shielded façades is at least 20 dB lower than the noise level at the most exposed façades of the dwelling (Directive 2002/49/EC). Although different researchers may not agree completely with this definition, surveys show that inhabitants of dwellings exposed to high road traffic noise levels can benefit from having access to a quiet side [43, 44, 45, 46]. This effect can be efficiently implemented in architecture design and urban planning by putting the noise sensitive rooms such as bedrooms at a quiet side. Even with modern sensor network technology, it would still be very costly to launch a dense measurement network in large cities to evaluate a quiet area or quiet side for a long term. As a result, marking a quiet side is still mainly based on noise maps. The accuracy of the noise mapping would then strongly affect the noise effect study.

Compared to tracing the sound rays in the horizontal 2D plane in the strategic noise maps, the background noise map focuses on the contributions from the roof top due to multiple reflections and distant sources. For some shielded areas where traced beams cannot reach these kinds of places, the background noise mapping dominates the noise levels (as shown in chapter 2). The distant sources, such as sources inside 1500 m were all included in the noise level calculation. By energetically summing the background noise maps to the strategic noise maps , the noise prediction could be corrected. To avoid over weighting the correction, the strategic noise map here should not include the diffraction from the roof top. In case it is difficult to re-calculate the strategic noise map, the background level can also be added as a first approximation since contributions of reflections from 2nd to infinite is usually 5 dB larger than the 1st reflection as shown in chapter 3.

To sum up the reflections in a canyon, it is too difficult to use the existing theoretical solutions, such as Pierce's method. Therefore, a simpler but still accurate method to calculate the sound diffraction over a thick barrier is developed based on Pierce's method, which is presented in chapter 2. Besides, the details of the background noise model is also presented in chapter 2. Since the background noise model has high accuracy and calculating efficiency, it may offer some ideas for the future CNOSSOS-EU model to calculate the background noise level after more validations and modifications.

The geometrical condition in a real urban area is much more complicated than the simplified assumptions made by the above mentioned models. Therefore these models often neglect effects such as the attenuation caused by roof shapes and propagating over multiple canyons etc. In the above mentioned background noise model, building roofs are supposed to be flat and the intermediate canyons are not considered when summing the multiple reflection effects. Although additional correction terms for the roof shape and intermediate canyon effect were proposed, more accurate calculations for these effect are still very important. In chapter 3, a generalized form was derived to calculate the sound propagating over non-flat roofs together with multiple reflections. The validation cases well matched this model, however, to implement it in a noise mapping software, one still needs to consider how to trace the roof shapes and canyon details between source and receiver. This part of work is much more difficult than the 2.5 D tracing strategy. Therefore, the model in chapter 3 appears as a future option instead of using it in current background noise mapping. The uncertainties of the background mapping will be further corrected with the dynamic mapping concept, an interpolation between measurement stations, in chapter 4.

1.4 Dynamic noise mapping

Although the strategic noise maps can be corrected by the background noise maps, uncertainties caused by the source model and propagation model are still in the predictions. In the source model, a vehicle is assumed to be simplified to a single point such as CNOSSOS-EU model or combination of a few point sources such as HARMONOISE model. Vehicles are classified to a few categories by the characteristics of noise emission. In every category, the vehicles are assumed to be identical with each other. The source power is split into a rolling noise part which is generated by the tire-road interaction and a propulsion noise part which is mainly generated by the engine and exhaust. The power emission of a single vehicle is related to the driving speed, vehicle category and other driving and road conditions. The total power emission level is also related to the traffic flow which is often a long-term average value. For minor roads, the traffic flow is often not available and also fluctuates considerably. In the propagation model [30, 28], the uncertainties mainly come from the indirect propagation paths, where objects exist isolating the source and receiver to be invisible. The sound has to travel through reflections, diffraction or their combinations to reach to a receiver. Additionally, some uncertainties could also be due to the simplification of ground and terrain characteristics. Reflections by the vertical obstacles are considered by the image sources strategy and very small (< 0.5 m for [30]) object would be ignored. The diffraction over a thick barrier (a building with flat roof) is calculated due to the geometrical relation among sources, receivers and the building itself, as well as the wave length. A detailed comparison between different engineering models can be found in the appendix. Another calculation uncertainty during the propagation is refraction and scattering by the meteorological turbulence.

Not only the long-term strategic noise map, but also the short-term dynamic pattern is very interesting, which is proved to be related to noise annoyance. Therefore dynamically predicting the sound level is becoming an increasing desire for soundscape and sound perception studies. Additionally, calculations of strategic noise maps do not include the dynamic pattern of temporary sources, such as loud temporary activities, loud (un)loading noise, the short-term traffic patterns and the one-way roads. Some other dynamically changed parameters, such as strong meteorological fluctuations are also not included in the strategic noise mapping. Therefore, it is motivated to develop a method to dynamically predict the sound levels by interpolating the noise maps between measurements, as shown in chapter 4.

A dynamic noise map is used to refer to a noise map that is updated in short time intervals (e.g. every 15 minutes) based on measurements made in a measurement network of noise sensors which is not necessary very dense. In addition to the usual L_{Aeq}, the map can also include other indicators that could be relevant for the evaluation of the effect of noise on people such as L_{10} or L_{90}. A dynamic noise map is usually obtained by tuning the noise calculations between measurement positions based on the strategic noise maps. One solution is to monitor the dynamic pattern of the sources and correct the immission levels proportionally to the changes of the sources [47, 48]. This solution implies that the propagation is fixed. This assumption will fail when the effect of meteorological condition cannot be ignored. Another solution is to interpolate the sound pressure levels directly from measurements taken at the sound observatories [49]. The measurement grids must be sufficiently density, otherwise the interpolation would cause large errors. Micro traffic simulations are not discussed since this method would not be possible to be updated in a short time interval [50, 51]. A noise map could be tuned by updating both the sources and propagations. Considering correcting every source and propagation, the calculation of sound pressure level at a measurement station could be proportional to the product of the number of sources N_s and number of propagation paths N_h: $N_s \cdot N_h$. Updating this number of corrections would require too much CPU time and is anyhow only statistically valid. The degree of freedom in this kind of system would also be too large to be determined. Therefore, the sources and the propagation "paths" are grouped to a few categories. If the correction in every category is supposed to be the same, the updating task then reduced to be proportional to the product of the number of source category and number of receiver category: $N_m \cdot N_n$, where N_m is the number of source category and N_n is the number of category of propagation paths.

Updating the sound levels per 15 min is suitable for capturing typical activity patterns and resulting in low standard errors at the same time among different measurement days. In an urban environment, the short-term dynamics are mainly determined by passing of vehicles. A few minutes could be a suitable time interval to balance the stability and representability. Therefore, the goal of the fitting is updating the fitting system per 15 min, which also require a small number of degrees of freedom.

The discussion on the underlying model and reduction of degrees of freedom explicitly depends on frequency. Although in principle there are no fundamental constrains in performing the fit to measurements on a frequency per frequency basis, the additional freedom jeopardizes the uniqueness of the solution and thus could easily lead to over-fitting. The corrections on both sound power and propagation are assumed to be independent on frequency.

1.5 Outline of the research

In this doctoral dissertation, the main tasks are to develop a background noise model for the shielded areas and an interpolation method to dynamically predict the urban noise map. The dissertation will be presented as follows. In chapter 1, traffic noise and its effect are briefly reviewed. The motivation of this work and the basic improvement are also introduced. In chapter 2, the general model to correct the background noise mapping is discussed. In this chapter, a simplified diffraction function over a thick barrier is developed. Besides, the effect of multiple reflections is studied. The main formula is deduced based on the simplified diffraction function and the main correction coefficients are fitted from finite-difference time domain (FDTD) simulations. In chapter 3, this background noise model is generalized to solve more common urban situations as propagating over multiple building roofs. Additionally, the sum of multiple reflections over one building (a thick barrier) is generalized to over many buildings. The generalization was also validated by FDTD simulations. In chapter 4, the dynamic noise mapping model is developed based on the models mentioned in the previous chapters. The dynamic mapping method is validated by a case study in Katendrecht of Rotterdam. In chapter 5, conclusions and suggestions for future work are discussed. In the appendix, the HARMONOISE and CNOSSOS-EU source model are compared. The diffraction functions among commonly used theoretical and engineering models are also compared. The FDTD configurations used for extracting the parameters in the QSIDE model are listed.

1.6 Publications

1.6.1 Publications in international journals

- Weigang. Wei, A. Bockstael, B. De Coensel, D. Botteldooren. *Interference of Speech and Interior Noise of Chinese High-Speed Trains with Task Performance*. ACTA ACUSTICA UNITED WITH ACUSTICA, 88(5):790-799, SEP-OCT 2012.

- Weigang. Wei, D. Botteldooren, T. Van Renterghem, M. Hornikx, J. Forssén, E. Salomons, M. Ögren. *Urban Background Noise Mapping: The General Model*. ACTA ACUSTICA UNITED WITH ACUSTICA, 100(6):1-1, NOV-DEC 2014.

- M. Hornikx, J. Forssén, D. Botteldooren, T. Van Renterghem, Weigang. Wei, M. Ögren, E. Salomons. *Urban Background Noise Mapping: The Multiple-Reflection Correction Term.* ACTA ACUSTICA UNITED WITH ACUSTICA, 100(2):293-305, MAR-APR 2014.

- J. Forssén, M. Hornikx,D. Botteldooren, Weigang. Wei, T. Van Renterghem, M. Ögren. *A model of sound scattering by atmospheric turbulence for use in noise mapping calculations*. ACTA ACUSTICA UNITED WITH ACUSTICA, 100(5): 810-815(6), SEP-OCT 2014.

1.6.2 Publications in international conferences

- Weigang. Wei, A. Bockstael, B. De Coensel, D. Botteldooren. *Effects of Chinese high-speed train compartment noise and speech on task performance*. FORUM ACUSTICUM 2011, Aalbog, Denmark, July 2011.

- Weigang. Wei, T. Van Renterghem, D. Botteldooren,M. Hornikx, J. Forssén, E. Salomons, M. Ögren. *An efficient model for background noise mapping*. Euronoise 2012, Prague, Czech, June, 2012.

- Weigang. Wei, T. Van Renterghem, D. Botteldooren. *An efficient method to calculate the insertion loss of a rigid barrier*. AIA-DAGA 2013, Merano, Italy, March, 2013.

- Weigang. Wei, T. Van Renterghem, D. Botteldooren. *Monitoring sound exposure by real time measurement and dynamic noise map*. FORUM ACOUSTICUM 2014, Krakow, Poland, September, 2014

References

[1] Birgitta Berglund, Thomas Lindvall, and Dietrich H Schwela. *Community Noise*. Technical Report April, 1999.

[2] *Pedestrian Safety, Urban Space and Health*. Technical report, International Transport Forum, August 2012.

[3] WHO Regional Office for Europe. *World Health Organization*.

[4] *European Vehicle Market Statistics Pocketbook 2013*. 2013.

[5] WHO Regional Office for Europe. *Burden of disease from Burden of disease from*. Technical report, 2011.

[6] E. Öhrström. *SLEEP DISTURBANCE , TO PILOT PSYCHO-SOCIAL SURVEY AMONG OF ROAD AND MEDICAL EXPOSED TRAFFIC*. Journal of Sound and Vibration, 133:117–128, 1989.

[7] Rainer Hoeger, Dirk Schreckenberg, Ute Felscher-suhr, and Barbara Griefahn. *Night-time Noise Annoyance : State of the Art*. Noise Pollution & Health, pages 51–57.

[8] European Commission. *Position paper on dose response relationships*. Technical report, 2002.

[9] Tetsuya Kaneko and Kyoichi Goto. *Dose-response relationship between aircraft noise and annoyance around an airport in Japan*. In 9th International Congress on Noise as a Public Health Problem (ICBEN), pages 1–5, Foxwoods, 2008.

[10] Wolfgang Babisch. *Transportation noise and cardiovascular risk : Updated Review and synthesis of epidemiological studies indicate that the evidence has increased*. Noise & Health, 8(March), 2006.

[11] H Ising and B Kruppa. *Health Effects caused by Noise : Evidence in the Literature from the Past 25 Years*. Noise & Health, pages 5–13, 2004.

[12] Michael D Seidman and Robert T Standring. *Noise and quality of life*. International journal of environmental research and public health, 7(10):3730–8, October 2010.

[13] E Murphy and E.A. King. *Environmental Noise Pollution: Noise Mapping, Public Health, and Policy*. Elsevier, Burlington, MA, USA, 2014.

[14] Yvonne de Kluizenaar, Sabine a Janssen, Frank J van Lenthe, Henk M E Miedema, and Johan P Mackenbach. *Long-term road traffic noise exposure is associated with an increase in morning tiredness.* The Journal of the Acoustical Society of America, 126(2):626–33, August 2009.

[15] Jiro Kaku, Masaaki Hiroe, Sonoko Kuwano, and Seiichiro Namba. *Sleep disturbance by traffic noise: an experimental study in subjects' own houses using a portable CD player*. Journal of Sound and Vibration, 277(3):459–464, October 2004.

[16] M. Vallet, J.-M. Gagneux, V. Blanchet, B. Favre, and G. Labiale. *Long term sleep disturbance due to traffic noise*. Journal of Sound and Vibration, 90(2):173–191, September 1983.

[17] Jenny Selander, Mats E Nilsson, Gösta Bluhm, Mats Rosenlund, Magnus Lindqvist, Gun Nise, and Göran Pershagen. *Long-term exposure to road traffic noise and myocardial infarction.* Epidemiology (Cambridge, Mass.), 20(2):272–9, March 2009.

[18] Wolfgang Babisch. *Road traffic noise and cardiovascular risk.* Noise & Health, 10:27–33, 2008.

[19] Wen Qi Gan, Hugh W Davies, Mieke Koehoorn, and Michael Brauer. *Association of long-term exposure to community noise and traffic-related air pollution with coronary heart disease mortality.* American journal of epidemiology, 175(9):898–906, May 2012.

[20] Diarmid Campbell-lendrum, Annette Prüss-üstün, Diarmid Campbell-lendrum, Carlos Corvalán, and Alistair Woodward. *Occupational noise Assessing the burden of disease from work-related hearing impairment at national and local levels*. Technical Report 9, World Health Organization Protection of the Human Environment, Geneva, 2004.

[21] Gaetano Licitra. *Noise Mapping in the EU: Models and Procedures*. CRC Press, 2012.

[22] Dick Botteldooren. *Finite-difference time-domain simulation of low-frequency room acoustic problems*. J. Acoust. Soc. Am., 98:3302–3308, 1995.

[23] Dick Botteldooren. *Numerical model for moderately nonlinear sound propagation in three-dimensional structures*. J. Acoust. Soc. Am., 100:1357–1367, 1996.

[24] Timothy Van Renterghem, Erik Salomons, and Dick Botteldooren. *Parameter study of sound propagation between city canyons with coupled FDTD-PE model*. Appl. Acoust., 67(9):487–510, 2006.

[25] Julian R Wright. *An Exact Model of Acoustic Radiation in Enclosed Spaces*. Audio Engineering Society, 43(10):813–820, 1995.

[26] International Organization for Standardization. *ISO 9613-2:1996 Acoustics attenuation of sound during propagation outdoors - Part 2*. 1996.

[27] Jérôme Defrance, Erik Salomons, Ingrid Noordhoek, Dietrich Heimann, Birger Plovsing, Greg Watts, Hans Jonasson, Xuetao Zhang, Eric Premat, Isabelle Schmich, François Aballea, Marine Baulac, and Foort de Roo. *Outdoor Sound Propagation Reference Model Developed in the European Harmonoise Project*. Acta Acust. Acust., 93:213–227, 2007.

[28] Erik Salomons, Dirk van Maercke, Jérôme Defrance, and Foort de Roo. *The Harmonoise Sound Propagation Model*. Acta Acust. Acust., 97(1), 2011.

[29] Guillaume Dutilleux, Jérôme Defrance, David Ecotière, Benoit Gauvreau, Michel Bérengier, Francis Besnard, and Emmanuel Le Duc. *NMPB-Routes-2008: The Revision of the French Method for Road Traffic Noise Prediction*. Acta Acust. Acust., 96:452–462, 2010.

[30] *Environmental Noise and the CNOSSOS-EU initiative*, 2012.

[31] M. Arana, R. San Martin, M. L. San Martin, and E. Aramendia. *Strategic noise map of a major road carried out with two environmental prediction software packages*. Environmental monitoring and assessment, 163(1):503–513, 2010.

[32] Andrzej Czyewski, Józef Kotus, and Maciej Szczodrak. *Creating Acoustic Maps Employing Supercomputing Cluster*. Archives of Acoustics, 36(2):395–418, January 2011.

[33] E.A. King and H.J. Rice. *The development of a practical framework for strategic noise mapping*. Applied Acoustics, 70(8):1116–1127, August 2009.

[34] Joon Hee Ko, Seo Il Chang, and Byung Chan Lee. *Noise impact assessment by utilizing noise map and GIS: A case study in the city of Chungju, Republic of Korea*. Applied Acoustics, 72(8):544–550, July 2011.

[35] Bo Wang and Jian Kang. *Effects of urban morphology on the traffic noise distribution through noise mapping: A comparative study between UK and China*. Applied Acoustics, 72(8):556–568, July 2011.

[36] Paulo Henrique Trombetta Zannin and David Queiroz De Sant Ana. *Noise mapping at different stages of a freeway redevelopment project A case study in Brazil*. Applied Acoustics, 72(8):479–486, July 2011.

[37] A. Can, L. Dekoninck, and D. Botteldooren. *Measurement network for urban noise assessment: Comparison of mobile measurements and spatial interpolation approaches*. Applied Acoustics, 83:32–39, September 2014.

[38] Timothy Van Renterghem, Dick Botteldooren, and Luc Dekoninck. *Evolution of building façade road traffic noise levels in Flanders.* Journal of environmental monitoring : JEM, 14(2):677–86, February 2012.

[39] Fei Zuo, Ye Li, Steven Johnson, James Johnson, Sunil Varughese, Ray Copes, Fuan Liu, Hao Jiang Wu, Rebecca Hou, and Hong Chen. *Temporal and spatial variability of traffic-related noise in the City of Toronto, Canada.* The Science of the total environment, 472:1100–7, February 2014.

[40] Wolfgang Kropp, Jens Forssén, and Mikael Ogren. *The failure of traditional traffic noise control for quiet areas*. In Inter-Noise 2004, 2004.

[41] W. Wei, D. Botteldooren, T. Van Renterghem, M. Hornikx, J. Forssén, E. Salomons, and M. Ögren. *Urban Background Noise Mapping: The General Model.* Acta Acust. United Ac, 100(6):1098–1111, 2014.

[42] Jian Kang. *Urban sound envvironment.* Taylor and francis, London, 2007.

[43] E. Öhrström, A. Skånberg, H. Svensson, and A. Gidlöf-Gunnarsson. *Effects of road traffic noise and the benefit of access to quietness*. J. Sound Vib., 295:40–59, 2005.

[44] E. Öhrström. *Psycho-social effects of traffic noise exposure*. J. Sound Vib., 151(3):513–517, 1991.

[45] Yvonne de Kluizenaar, Erik M. Salomons, Sabine A. Janssen, Frank J. van Lenthe, Henk Vos, Han Zhou, Henk M. E. Miedema, and Johan P. Mackenbach. *Urban road traffic noise and annoyance: The effect of a quiet facade*. J. Acoust. Soc. Am., 130(4):1936–1942, 2011.

[46] Timothy Van Renterghem and Dick Botteldooren. *Focused Study on the Quiet Side Effect in Dwellings Highly Exposed to Road Traffic Noise*. International Journal of Environmental Research and Public Health, 9(12):4292–4310, November 2012.

[47] Gabor Gereb. *Real-time updating of noise maps by source-selective noise monitoring*. NOISE CONTROL ENGINEERING JOURNAL, 61(2):228–239, March 2013.

[48] Maciej Szczodrak, Józef Kotus, Boena Kostek, and Andrzej Czyewski. *Creating Dynamic Maps of Noise Threat Using PL-Grid Infrastructure*. Archives of Acoustics, 38(2):235–242, January 2013.

[49] Dae Seung Cho, Jin Hyeong Kim, and Douglas Manvell. *Noise mapping using measured noise and GPS data*. Applied Acoustics, 68(9):1054–1061, September 2007.

[50] Bert De Coensel, Dick Botteldooren, Filip Vanhove, and Steven Logghe. *Microsimulation Based Corrections on the Road Traffic Noise Emission Near Intersections*. 93(December 2006):241–252, 2007.

[51] Ma Xia-lin and Cai Ming. *Rendering of Dynamic Road Traffic Noise Map based on Paramics*. Procedia - Social and Behavioral Sciences, 96(Cictp):1460–1468, November 2013.

2

Urban background noise mapping: the general model

★★★

Published in Acta Acustica United with Acustica

Surveys show that inhabitants of dwellings exposed to high noise levels benefit from having access to a quiet side. However, current practice in noise prediction often underestimates the noise levels at a shielded façade. Multiple reflections between façades in street canyons and inner yards are commonly neglected and façades are approximated as perfectly flat surfaces yielding only specular reflection. In addition, sources at distances much larger than normally taken into account in noise maps might still contribute significantly. Since one of the main reasons for this is computational burden, an efficient engineering model for the diffraction of the sound over the roof tops is proposed, which considers multiple reflections, variation in building height, canyon width, façade roughness and different roof shapes. The model is fitted on an extensive set of full-wave numerical calculations of canyon-to-canyon sound propagation with configurations matching the distribution of streets and building geometries in a typical historically grown European city. This model allows calculating the background noise in the shielded areas of a city, which could then efficiently be used to improve existing noise mapping calculations. The model was validated by comparison to long-term measurements at 9 building façades whereof 3 were at inner yards in the city of Ghent, Belgium. At shielded façades, a strong improvement in prediction accuracy is obtained.

2.1 Introduction

Several researchers found that inhabitants of dwellings exposed to road traffic noise levels can benefit from having access to a quiet side [1, 2, 3, 4]. The European Environmental Noise Directive (END) specifies that a quiet side is present if the noise level at the shielded façade is at least 20 dBA lower than the noise level at the most exposed façade of the dwelling (Directive 2002/49/EC). However, there is still some debate about accurately defining a quiet side (e.g. [5]). In typical European cities, many enclosed shielded courtyards and parks exist that can provide such quiet areas. Notwithstanding the lack of a good definition, research on quiet sides and its implementation in urban planning also suffers from a lack of accuracy in commonly used noise mapping when it comes to predicting noise levels in urban shielded areas. The EU is currently renewing its guidelines for methods to be used in noise mapping, yet the lack of accuracy of noise mapping in shielded areas is mainly due to the choices made during implementation and application of the methods. Typically, the underestimation of the noise level at such shielded places, is caused by limiting the number of reflections in streets and yards and by neglecting contributions of distant sources that could become dominant. To solve these problems, simplified theoretical models, such as the "flat city model" and the "equivalent source model(ESM)", were developed to predict the noise level in shielded courtyards [6, 7]. However, these models need further improvement. For example, the coupling between the sound field inside a street canyon and the propagation above the roofs can depend on the difference in height of the buildings forming the street canyon. Moreover, the ESM is computationally too costly to cover a whole city. In this chapter, an efficient engineering model for background noise mapping is proposed that is inspired by the concept of the "flat city model" and a new approximation to more advanced diffraction formulas. The coefficients of the proposed engineering model are fitted on an extensive set of 2D simulations of canyon-to-canyon sound propagation, which are based on finite-difference-time-domain (FDTD) method [8, 9]. The effect of multiple reflections, variation in building height, canyon width, building façade roughness, finite impedance and roof shape is taken into account. The proposed engineering model is designed to complement the noise map calculated by 2.5D methodologies in which the diffraction over buildings due to reflections between canyons may not be sufficiently considered. The direct field, reflection in the horizontal plane as well as diffraction around vertical edges is assumed to be accounted for by the "parent" model (e.g. following the CNOSSOS-EU methodology. The proposed extension calculates the contribution to the noise level caused by all sources that are shielded by at least one building in the vertical plane. In this work, a building is a construction of at least 4 m high and at least 5 m wide; conventional noise barriers are expected to be correctly included in the "parent" model. The resulting "background" noise level should be added to the level obtained using the "parent" model. With this approach the national and international standard methods currently in use can still be applied. For every contributing source the suggested procedure for calculating the "background" noise level at the shielded location reads:

$$L_{pb} = 10\log_{10}\left(10^{0.1L_{pdb}} + 10^{0.1L_{p,scatter}}\right) \tag{2.1}$$

$$L_{pdb} = L_W - A_{free} - A_{diffr} - A_{inter} \tag{2.2}$$

$$A_{diffr} = -10\log_{10}\left(10^{-0.1A_{bar}} + 10^{-0.1A_{can}}\right) \tag{2.3}$$

where,

- L_{pb} = the "background" sound pressure level excluding the diffraction around the vertical edges and excluding the diffraction over conventional noise barriers [dB].

- L_{pdb} = the contribution to the "background" level in still, homogeneous atmosphere [dB].

- L_W = sound power level per octave band of a point source representing part of the traffic, no directivity is taken into account since multiple sources will contribute to the shielded level as well as multiple reflections from various directions [dB].

- A_{diffr} = the attenuation caused by the building, which is limited by diffraction and multiple reflections over the building [dB]. The diffraction and reflections in the horizontal plane are not the concern of this chapter and they are supposed to be calculated in the END map.

- A_{free} = 3D free field divergence [dB].

- A_{bar} = the attenuation by the building(s) cutting the direct path between source and receiver limited by diffraction over the building roof, including the effect of the ground. Only the direct diffraction path without reflections in the canyon is considered in this term [dB].

- A_{can} = the attenuation of the sound following a path between source and receiver including at least one reflection in the source and/or receiver canyon. If canyons are present, this term quickly dominates A_{bar} and thus determines A_{diffr} [dB].

- A_{inter} = additional attenuation caused by diffraction at intermediate canyons [dB].

- $L_{p,scatter}$ = the contribution to the background sound level caused by scattering from atmospheric turbulence [dB] [10].

Atmospheric absorption is not included as a separate term in this model as it is implicitly included in the A_{can} term, where the absorption was added by post-processing the FDTD simulation results. One of the major assumptions for the model is that the sound propagation in 3D can be calculated by the summation of many 2D sections. This so called 2.5D approach is quite common and forms e.g. the basis of the Harmonoise reference model [11] and the CNOSSOS-EU methodology [12]. Also, the full wave numerical model used to extract the coefficients in the proposed equations cannot be used for 3D simulations due to computational cost. Therefore, also for the reference calculation, line sources are split into many emission points and all contributions are summed. In this approach, façades are "twisted" so their faces become normal to the line connecting source-receiver [13]. It can be shown from numerical simulations that the error caused by using the twisted angle approach is reasonably small [14]. A correction for 3D free field spreading of the contributions of reflections is taken into account. A second important assumption is that wind and temperature gradients are not included in the A_{bar} and A_{can} terms. For the A_{inter} term meteorological effects (except scattering) are considered implicitly(see further) since downwind refraction over larger distances may have a noticeable effect.

This chapter is organized as follows. In section 2, the configurations and setups of the simulations that are used for fitting coefficients in the engineering model are introduced. In section 3, the attenuation terms (A-terms) are studied in detail. In section 4, the calculated background noise levels are compared to long-term measurements at 9 locations in the city of Ghent, Belgium. The latter comparison includes the contribution from turbulence scattering. The engineering model developed for calculating turbulence scattering can be found in [10].

2.2 Simulation configurations and setups

The simulations cover different widths of source canyons, receiver canyons and intermediate buildings, as well as different building heights. Distributions of these parameters for a typical historically grown European city, are extracted from a GIS-building layer for the city of Ghent. The distribution of the projected canyon and building widths along each source-receiver line is shown in figure 2.1. Note that the width is defined along a line that is not necessarily orthogonal to the building façade, which is compatible with the point-to-point model that is proposed. 72% of the projected buildings widths and 78% of the canyons are less than 50 m wide. Besides, the most frequently projected widths of the buildings and canyons are 24 m and 12 m, respectively. The full-wave numerical simulations on which the engineering model is based have been limited to canyon and building widths between 4.8 m and 42 m. The heights of the buildings are varied from 4 to 16 m. The building façades are modeled in a realistic way by assigning different materials and making the façade surface irregular to allow for the build-up of a diffuse sound field in the city canyons, which was shown to be an essential aspect of urban sound propagation [15]. The road surface is modelled as perfectly reflecting both in source and receiver canyon. In these simulations, the normalized impedance of windows and brick walls are taken as Z_n = 77 and Z_n = 10 respectively. Receivers are located along the façade and across the canyons. A typical simulation configuration is shown in figure 2.2, where, W_s, W, W_r are the width of the source canyon, intermediate building and receiver canyon respectively. H_i is the height of the building in the direct sound path, and H_s, H_r are the heights of the buildings flanking the source and receiver canyon respectively. Since the sound waves travel a longer distance because of multiple reflections, the air will absorb more sound energy than during direct propagation between source and receiver. The effect of the air absorption, with T = 10 °C and Humidity= 70%, is added to the simulated impulse response using the approach proposed in references [16, 17].

When sound waves oscillate in the canyon, the multiple reflection effect will change with the relative location of the source and receiver, the height of the buildings and the width of the canyon and buildings. In total, 565 configurations with combinations of these parameters were simulated.

The excess attenuation caused by screening and ground effects was proven not to be affected too much by source type in the far field [18]. However, in the case of multiple reflections in a street canyon, small differences might still occur. Therefore, the time-domain response is multiplied by $1/\sqrt{ct}$ to approximately translate the line source propagation to point source propagation [19]. In our data post-processing, this technique is used to approximate point source propagation from canyon to canyon.

2.3 Analysis of attenuation terms: A_{bar}, A_{can}, and A_{inter}

The attenuation is resolved as separate parts A_{diffr} and A_{inter}, where A_{diffr} is calculated by the sum A_{bar} and A_{can}, as $-10\log_{10}\left(10^{-0.1A_{bar}} + 10^{-0.1A_{can}}\right)$. A_{bar} and A_{can} will be formulated in section 2.3.1 and section 2.3.2 respectively. A_{inter} will be introduced in section 2.3.3.

2.3.1 A_{bar}

A_{bar} is the attenuation of a thick barrier including the presence of the ground. In absence of canyons and in case of a flat roof, it is the only remaining term. In this study A_{bar} = $A_{bar,flat,}$ + $A_{bar,roof}$, where, $A_{bar,flat}$ is the attenuation of a rigid barrier with flat roof; $A_{bar,roof}$ is the correction of the roof shape in dB.

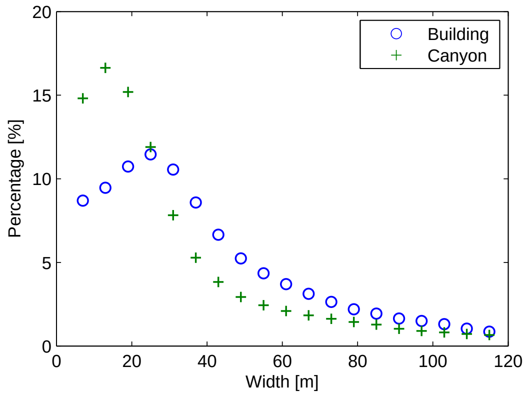

(a) Distribution

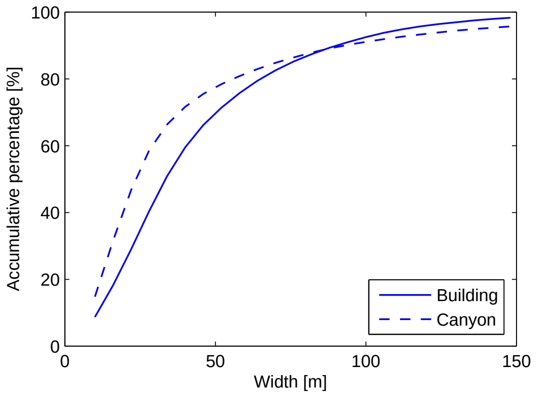

(b) Cumulative probability

Figure 2.1: Distribution(a) and cumulative probability(b) of the projected building and canyon width in the city of Ghent, Belgium. In the simulations, the widths of buildings and canyons are limited to 42 m.

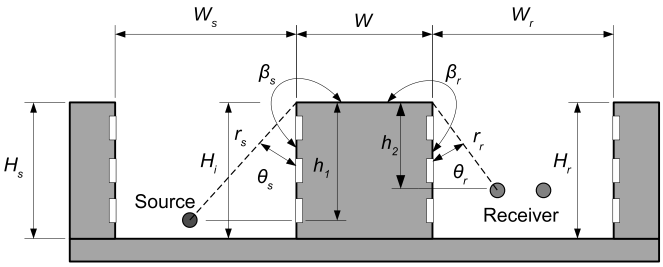

Figure 2.2: A typical simulation configuration, where W_s, W and W_r are the width of source canyon, intermediate building and receiver canyon; H_s, H_i and H_r are the height of the left, intermediate and right building; h_1 and h_2 are the distance from the source or receiver to the top of the building; θ_s and θ_r are the angle between the building façade and the connecting line from the source or receiver to the diffraction edge; β_s and β_r are the outside angle of the building which equals $3\pi/2$ in this study.

2.3.1.1 $A_{bar,flat}$: rigid barrier with flat roof

In most noise mapping methods (including CNOSSOS-EU), the ISO9613-2 diffraction formula or similar is used to calculate $A_{bar,flat}$. By comparing with an in-situ long-term measurements [20] and FDTD simulations, it was found that using the ISO standard to calculate A_{bar} leads to large predicting errors. Therefore, a more accurate but still computational efficient approximation is needed. In a first step, ground reflection is ignored. According to the literature [21, 22, 23, 24], $A_{bar,flat,0}$ can be expressed with high accuracy by equation (2.4):

$$A_{bar,flat,0} = -10\log_{10}\left\{\left(\frac{R}{L}\right)^2\left[f^2(X_1)+g^2(X_1)\right]\left[f^2(X_2)+g^2(X_2)\right]\right\} \quad (2.4)$$

where, $X_1 = X_s$ and $X_2 = B\ X_r$ when $X_s > X_r$; $X_1 = B\ X_s$ and $X_2 = X_r$ when $X_s < X_r$. X_s and X_r are functions of geometrical positions and diffraction angles. $X_s = \gamma_s M_{\nu s}(\beta_s - \theta_s)$, $X_r = \gamma_r M_{\nu r}(\beta_r - \theta_r)$, $\gamma_s = \sqrt{2r_s(W+r_r)/(\lambda L)}$, $L = \sqrt{(r_s+r_r+W)^2+(z_s-z_r)^2}$, ($z_s = z_r$ in the two dimensional case considered here), R is the distance between source and receiver, $B = \sqrt{W(W+r_s+r_r)/[(W+r_s)(W+r_r)]}$ and $M_{\nu s}(\theta) = \frac{\cos(\nu\pi)-\cos(\nu\theta)}{\nu\sin(\nu\pi)}$, $\nu_s = \pi/\beta_s$ and $\nu_r = \pi/\beta_r$. Definitions of parameters are shown in figure 2.2. $f(X)$ and $g(X)$ are functions of Fresnel integrals C and S [21]:

$$f(X) = [\frac{1}{2} - S(X)]\cos(\frac{1}{2}\pi X^2) - [\frac{1}{2} - C(X)]\sin(\frac{1}{2}\pi X^2) \quad (2.5)$$

$$g(X) = [\frac{1}{2} - C(X)]\cos(\frac{1}{2}\pi X^2) + [\frac{1}{2} - S(X)]\sin(\frac{1}{2}\pi X^2) \quad (2.6)$$

The combination $f^2 + g^2$ needed in equation (2.4) simplifies since the cosine and sine functions cancel out, reducing the expression to:

$$f^2(X) + g^2(X) = \Big[0.5 - C(X)\Big]^2 + \Big[0.5 - S(X)\Big]^2 \tag{2.7}$$

where X is the input argument. For a noise mapping model, calculating the Fresnel integrals is computationally too costly, so an approximation is needed.
For this, it is first observed that the distances involved in the formula for diffraction over building, and in particular W, are generally large compared to the wavelength. Thus, γ will be large. If source and receiver heights are much lower than the building height, $\beta - \theta$ will remain larger than π and it can be verified that M_ν is not smaller than one. For these cases, the input argument X satisfies $X \gg 0$. For large arguments, the Fresnel integrals can be approximated by [25]:

$$C(X) \approx 0.5 + \frac{1}{\pi X} \sin\left(\frac{\pi}{2} X^2\right) \tag{2.8}$$

$$S(X) \approx 0.5 - \frac{1}{\pi X} \cos\left(\frac{\pi}{2} X^2\right) \tag{2.9}$$

Inserting equation (2.8) and (2.9) into equation (2.7) results in a very simple form for $f^2 + g^2$:

$$f^2(X) + g^2(X) = \frac{1}{(\pi X)^2} \tag{2.10}$$

However, when the source or observer are in the extension of the plane of the roof, the angle difference $\beta - \theta$ approaches π and M_ν approaches zero which makes $S(X)$, $C(X)$ and $f^2(X) + g^2(X)$ become singular. To avoid this strong singularity while keeping the error at larger X limited, a small constant is added to the numerator and denominator. The value of this constant is obtained by requiring that the error it introduces is small for typical values of X_1 and X_2 found in a typical city (see Figure (2.4)). In addition the approximation minimizes the error over the whole range of angles (Figure (2.3)). The following approximation of equation (2.10) is proposed:

$$f^2(X) + g^2(X) = \left(\frac{0.37}{X + 0.37}\right)^2 \tag{2.11}$$

Thus, equation (2.4) is simplified to:

$$A_{bar,flat,0} \approx -10\log_{10}\left[\left(\frac{R}{L}\right)^2 \left(\frac{0.37}{X_1 + 0.37}\right)^2 \left(\frac{0.37}{X_2 + 0.37}\right)^2\right] \tag{2.12}$$

When $X_s > X_r$, $X_1 = \sqrt{\frac{6r_s(W+r_r)}{\lambda(r_s+W+r_r)}}\left|-0.5 + \cos(\frac{2}{3}\theta_s)\right|$,
$X_2 = \sqrt{\frac{6r_rW}{\lambda(W+r_r)}}\left|-0.5 + \cos(\frac{2}{3}\theta_r)\right|$;
when $X_s < X_r$, $X_1 = \sqrt{\frac{6r_sW}{\lambda(r_s+W)}}\left|-0.5 + \cos(\frac{2}{3}\theta_s)\right|$,

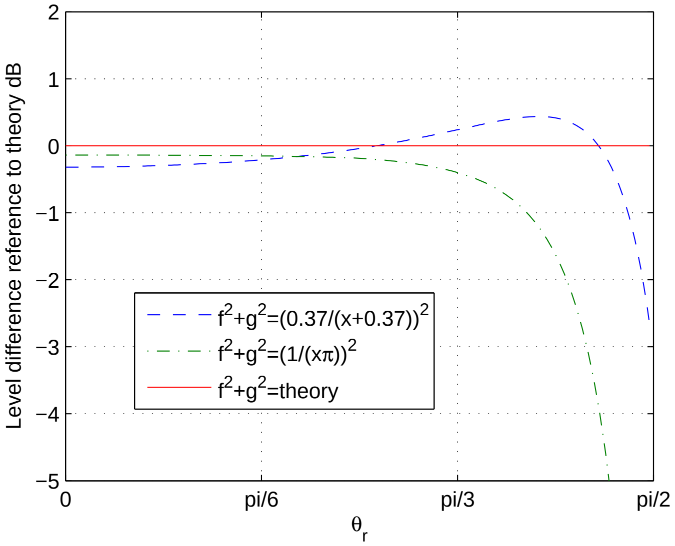

Figure 2.3: Error estimation of $f^2 + g^2$ compared with the theoretical values. In this case, $W = 10\lambda, r_s = r_r = 10\lambda, \beta_s = \beta_r = \frac{3\pi}{2}, \theta_s = \frac{\pi}{4}$, θ_r increases from 0 to $\pi/2$

$X_2 = \sqrt{\frac{6r_r(W+r_s)}{\lambda(r_s+W+r_r)}}\left|-0.5 + \cos(\frac{2}{3}\theta_r)\right|$.

Figure 2.3 illustrates how, for a typical urban sound propagation case, the large argument approximation and the proposed approximation for the Fresnel integrals differ from the accurate calculation. Although there is a small increase in inaccuracy for the proposed approximation when θ_r is very small, a strong benefit can be observed for $\theta_r > \pi/3$. Even when $\theta_r = \pi/2$, there is still less than 3 dB deviation. Specifically, at $X = 0$ the approximate formula gives 1, however, knowing that C and S become zero at $X = 0$, the actual value should be 0.5, which implies a 3 dB error. It should however be kept in mind that this situation will only occur for very few of the source receiver paths contributing to the overall noise level. To further illustrate the fit of the proposed approximation for diffraction over buildings, the distribution of the input X is extracted for the city of Ghent and plotted together with error contours in figure 2.4. At the X_1 and X_2 combinations where the distribution peaks, the error introduced by using equation (2.12) is particularly small and it stays below 1.5 dB for all combinations that have a significant probability of occurrence.

With this simplification, the Fresnel integrals in equation 2.7 are canceled out and only the geometrical parameters remains, which reduces computing time considerably and makes it easier to implement. It is suggested to include contributions

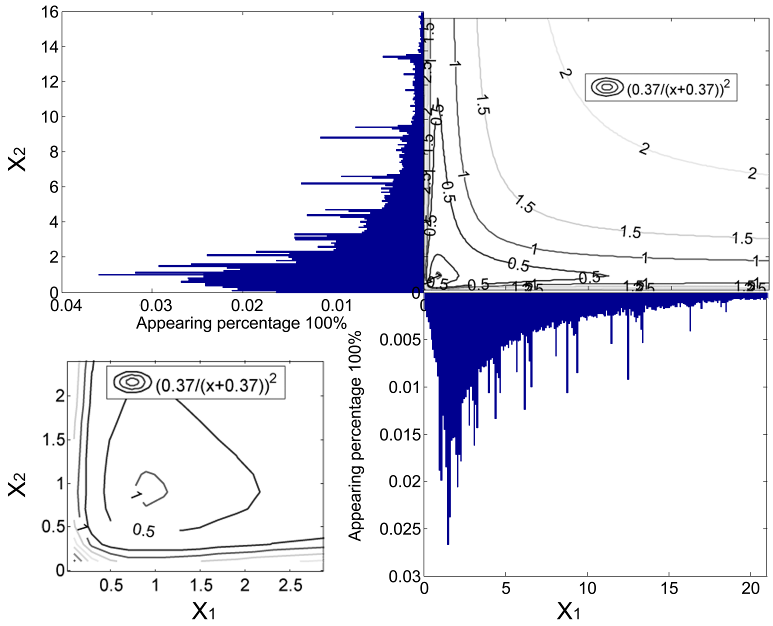

Figure 2.4: Error estimation reference to the theoretical solution, where "$\left(\frac{0.37}{X+0.37}\right)^2$" *indicates the equation (2.11). Every line indicates 0.5 dB difference.*

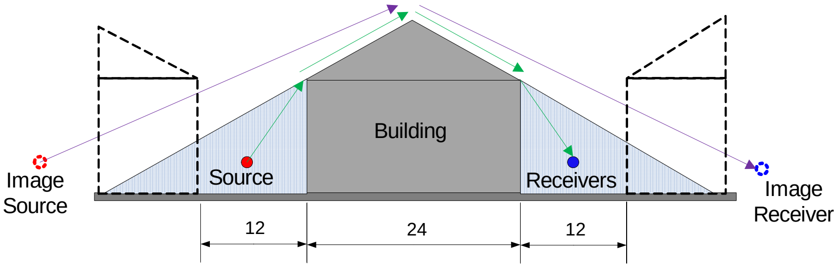

Figure 2.5: Effect of roof shape.

from the image sources due to ground reflections explicitly as a rule. Since the source height for road traffic noise applications is usually very low, the diffraction term does not differ significantly between the path from the original source and from the image source and the calculation can be simplified by assuming that $A_{bar,flat}$ is the same as $A_{bar,flat,0}$. The total $A_{bar,flat}$ can be obtained by summing up the contribution of paths "source→ receiver" $A_{bar,flat,0}$, "image source → receiver" $A_{bar,flat,1}$, "source → image receiver" $A_{bar,flat,2}$ and "image source → image receiver"

2.3.1.2 $A_{bar,roof}$: correction of roof shape

In some European city centers, gabled roofs are very common. The sound waves propagating over an idealized gabled roof may be diffracted once, twice or three times before reaching the observer. It should be noted that roofs may be more complicated and diffraction may result in a wide range of significantly different sound attenuation [26]. The effect of roof shape depends on the source and receiver position, the angle of the roof and the building height. According to the statistics for Ghent (as a typical old European city), the most common width of canyons and buildings is 12 m and 24 m respectively, and the mean height of the buildings is 10.9 m. If the height of the roof is assumed to be 4.5 m, then most of the sources and receivers below 4.5 m high would be located inside the shadow region where the sound wave has to diffract three times to reach the receiver at the other side of the building, as shown in figure 2.5. Under this condition, $A_{bar,roof}$ is linearly correlated to $A_{bar,flat}$. To simplify the calculation of the roof, $A_{bar,roof}$ is rewritten as a linear function of $A_{bar,flat}$:

$$A_{bar,roof} = q_0 A_{bar,flat} - q_1 \tag{2.13}$$

Fitting on 1788 numerical calculations by least squares method yields values of, $q_0 = 0.27$ and $q_1 = 3.4$, with a mean squared error of the fit equal to 3.0 dB for equation (2.13). The fitting database covers building heights from 6 m to 16 m,

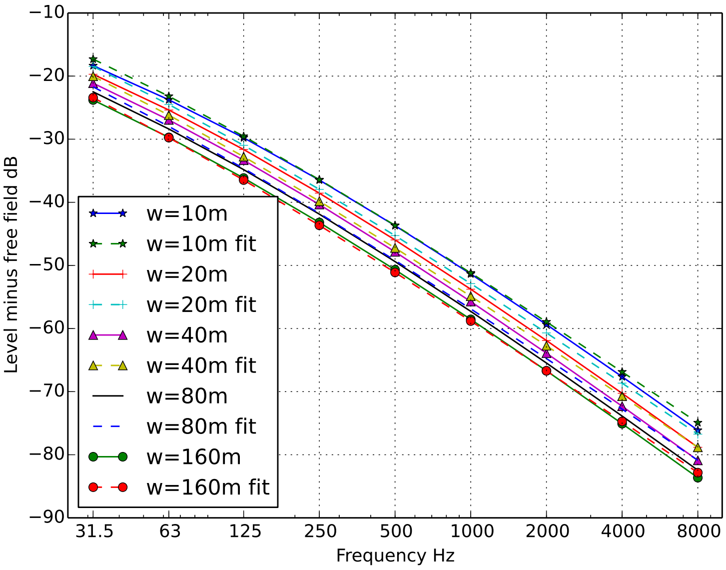

Figure 2.6: Accuracy of the fitted and analytical curve. The curve labeled "$W = 10m$" indicates the exact values, while curve labeled "$W = 10m$ fit" indicates the approximated values obtained using equation (2.13). The height of the building is 12 m. The source is 5 m to the façade and the distances from receivers to façade are 0.1, 0.5, 1, 2, 3, 5 m respectively.

building widths from 10 m to 160 m and all roof heights are 4.5m. Figure (2.6) shows the accuracy of the fit for a particular situation.

If a source canyon or a receiver canyon is present, the image source or the image receiver would most probably lie outside the three-diffraction region, which means that the effect of roof shape on the multiple-reflection path would probably be much more important. The roof effect in such cases is discussed in detail in section(2.3.2) as $A_{can,roof}$.

2.3.2 A_{can}

A_{can} is the attenuation of the sound following a path between source and receiver including at least one reflection in the source and/or receiver canyon. $A_{can} = A_{can,flat} + A_{can,roof}$, where $A_{can,flat}$ is the extra attenuation in case of a flat roof on the intermediate building; $A_{can,roof}$ is a correction accounting for a gabled roof shape.

An analytic formulation for the additional effect of the canyons has to fulfill some requirements: 1) if the height of the outer buildings goes to zero, the term should vanish; 2) if the outer buildings become much higher than the screening building, A_{can} should saturate when further increasing the outer building height.

2.3.2.1 Contribution of multiple reflections

Multiple reflections, occurring at the façades of the outer buildings and intermediate building, influence the canyon-to-canyon propagation in a different way. When H_s or H_r increases, the effect of multiple reflections increases monotonically at all frequencies. When H_i increases, the effect of multiple reflections increases at one hand. At the other hand, the shielding of the middle building also increases. Similar to A_{bar}, $A_{can,flat}$ is also frequency dependent.

2.3.2.2 Formulation of $A_{can,flat}$

Suppose the buildings are higher than 4 m and the sources are in the middle of the canyon, then an analytical form of $A_{can,flat}$ can be obtained based on image source theory. Details are described in Appendix A2. By adding fitting coefficients $F(0)$, $F(1)$, $F(2)$ and $F(3)$ to different contributing parts, small approximation errors as well as effects of non flat façades can be reduced. The proposed analytical form thus reads:

$$\begin{aligned} & A_{can,flat} \approx \\ & -F(0) 10 \log_{10} \Bigg[F(1) \frac{C_{1s} \rho_s^6 R^2}{(C_{3s} + W_s)^2} 10^{0.1 L_{hs}} + F(2) \frac{C_{1r} \rho_r^6 R^2}{(C_{3r} + W_r)^2} 10^{0.1 L_{hr}} \\ + \quad & F(3) \frac{\rho_s^6 \rho_r^6 R^2}{(3.31 h_1 / \sqrt{\lambda} + C)(3.31 h_2 / \sqrt{\lambda} + C)} 10^{0.1 L_{hs}} 10^{0.1 L_{hr}} \Bigg] \end{aligned} \tag{2.14}$$

where $C = 1.5W_s + W + 1.5W_r$, other parameters can be found in the Appendix A2.

The three terms in equation (2.14) describe the contribution from all image sources to all image receivers. The $F(1)$ term can be interpreted as a reverberant source canyon field diffracted into the receiver canyon. As such $(C_{3s} + W_s)^2 = 1/\left(3.31 h_1 \sqrt{W/\lambda} + 1.5 W_s + W + r_r\right)^2$ expresses mainly the amplification due to the source canyon reverberation. A similar interpretation can be given to the F(2) and F(3) terms. If W becomes very large, the whole $F(1)$, $F(2)$ and $F(3)$ term will approach $F(1) C_{1s} \rho_s^6 10^{0.1 L_{hs}}$, $F(2) C_{1r} \rho_r^6 10^{0.1 L_{hr}}$ and $F(2) \rho_s^6 \rho_r^6 10^{0.1 L_{hs}} 10^{0.1 L_{hr}}$, which implies that the effect of the source and receiver canyon become independent and are then only related to the receiver or source canyon dimension. This is also verified by numerical simulation as shown in [14]. If W_s becomes very big, the source canyon effect will vanish and similar situations can be found for the receiver canyon if W_r becomes large. If $h_2 \to 0$, L_{hr} becomes meaningless because of $(H_r - h_r)/(H_i - h_r)$ tending to ∞. This condition implies that the receiver is at the same height as the top of the shielding building and the canyon effect can then be neglected. As a result, the $F(2)$ term becomes zero. Since the source position is almost close to the ground in most cases, h_1 is expected not to tend to zero.

Based on fitting equation (2.14) to the database containing (20740 numerical results) with $\rho_s = \rho_r = 0.97$, minimizing the quadratic error, the following coefficients were found: $F(0) = 1.04$, $F(1) = 12.53$, $F(2) = 21.75$ and $F(3) = 0.05$. The mean squared error between $A_{can,flat}$ and the simulated results is 7.1 dB. If both H_s and H_r are very large, $A_{can,flat}$ tends to a constant.

A comparison between the fitted equation and several common cases calculated by the FDTD method are shown in figure 2.7. Several typical configurations are depicted, showing good agreement between the fitted equation and the detailed simulations. The analytical approximation follows the increasing or decreasing trends very well, but it cannot capture the increase if $H_s > H_i$. Additionally, if H_s is much lower than H_i, an overestimation of the reflections could be observed. The reason could be because that the diameter of ellipsoid between image source and receiver is much bigger than H_s. In this condition, the sound waves “leak” from the canyon meanwhile the model still include this part.

2.3.2.3 $A_{can,roof}$

When canyons are present, the sound reflects in these canyons and the $A_{can,roof}$ can be considered as the extra attenuation of the sum of different $A_{bar,flat}$ terms with different powers and positions of image sources and receivers. However, the image sources could reach the receivers or image receivers by only one diffraction from the roof top which will significantly increase the sound power at the receiver positions, as show in figure 2.5. Additionally, this effect depends strongly on the geometrical configuration of the buildings and canyons which also differs significantly from one to another. In this study, $A_{can,roof}$ is quantified from the literature [26], where an extensive set of roof shapes was numerically studied. The general contribution of a gabled roof was around -5 dB. In this study, $A_{can,roof} = -5$ dB if both a source and a receiver canyons are present and $A_{can,roof}$ increases to -2.5 dB if only one canyon is present. $A_{can,roof}$ is zero on condition that the roof shape is flat.

2.3.3 A_{inter}

The presence of intermediate canyons could lead to additional attenuation of sound. Since A_{can} is fitted based on thick barrier simulations only, an additional correction term, A_{inter}, is necessary. According to the FDTD simulations, A_{inter} in-

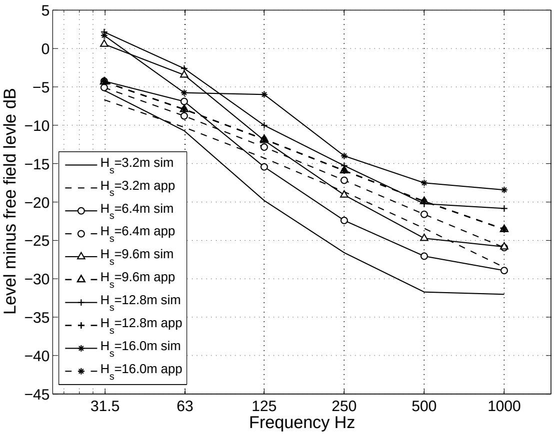

(a) Case study 1 with H_i = H_r = W_s = W_r = 9.6 m, W = 10 m, and H_s changes

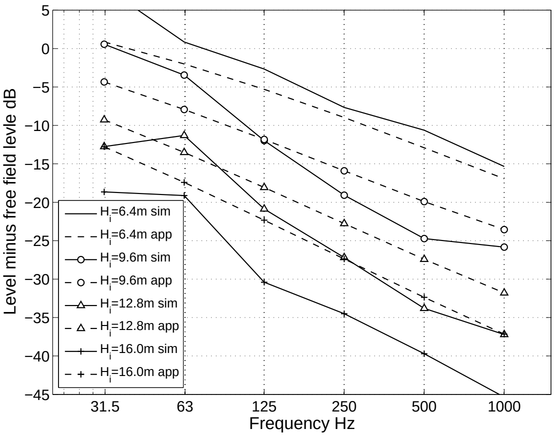

(b) Case study 2 with H_s = H_r = W_s = W_r = 9.6 m, W = 10 m, and H_i changes

Figure 2.7: Comparison between FDTD simulations and the analytical approximation. In these comparisons, the source is in the center of the canyon with height of 0.5 m. The receiver is 6.4 m away from the intermediate building which has a height of 4 m.

creases approximately by 1.8 dB/canyon for buildings of equal height as shown in(figure 2.8). A previous study also shows 1.8 dB/canyon [27] and similar findings were reported based on the measurement data from Södermalm in Stockholm [28]. As mentioned in the introduction, moderately downward refraction is assumed. At longer propagation distances, the effect of an atmospheric gradient resulting in downward refraction can be approximated by bending the ground surface upward which is comparable to lowering intermediate buildings [29]. Figure (2.9) shows the effect of different heights of intermediate buildings. In this figure, "H" indicates the height of the high intermediate building-block and equals 9.6 m; "L" is equal to 6.4 m; the combination of "H" and "L" indicates the succession of the building-blocks. For example "HLLHLH" means that the sound waves propagate over → a higher building → two lower buildings → a higher building → a lower building → a higher building, and finally to the receiver. According to the simulations, the effect caused by the low buildings in between can be reasonably neglected. Based on the calculations shown in figure 2.8 and comparable studies found in literature [13], an attenuation of 1dB/canyon is proposed as an efficient but still reasonably accurate approach for A_{inter} in more realistic situations. The geometrical data of Ghent (Belgium) and Södermalm (Sweden) [30] further show that one canyon per 100 meters is the most common canyon density. Because of the aforementioned reasons and given the complexity of the canyon structure in cities, the suggested broadband (and frequency independent) attenuation is 1 dB per 100 m. A maximum 5 dB is recommended in this model. This limit implicitly assumes that statistically speaking in downward refracting conditions no additional intermediate building will cut the curved propagation path once the distance reached 500 m.

2.4 Comparison with measurement

2.4.1 Introduction of the measurement network

An inner city noise measurement network in Ghent (Belgium) with microphone nodes [32] placed at both shielded and directly exposed locations is used as a first validation of the current engineering model. The measurement system is based on the "cheap" microphones. But its accuracy for long-term outdoor measurement is acceptable with 1 dB average error. The microphones are 1) tested and calibrated in the lab; 2) the qualified microphones together with pre-process chips are mounted to different places; 3)the measurement data send back to the net-work database to be analysed. By the measurement network, the noise levels of different places can be monitored simultaneously. It is a very convenient tool to validating predicting models and run mega analysis.

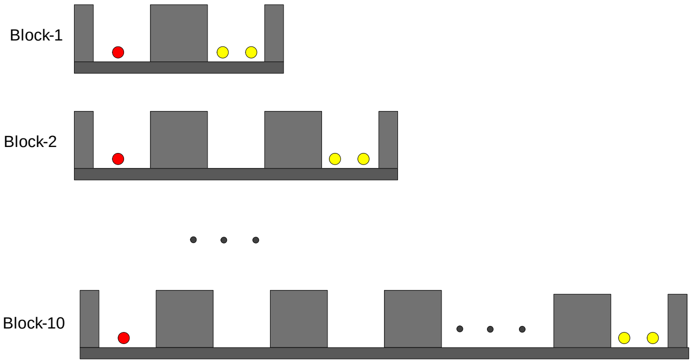

(a) Configuration

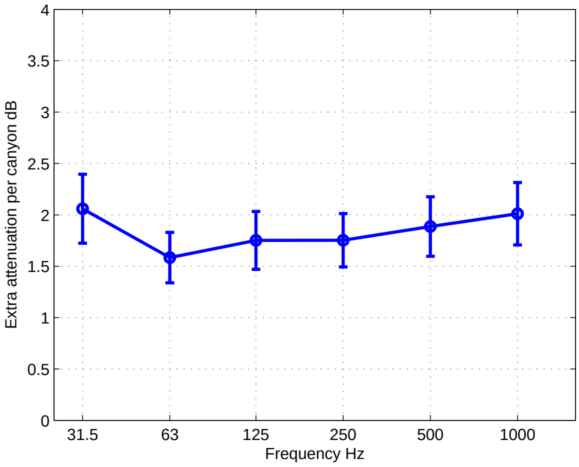

(b) Attenuation per canyon

Figure 2.8: Attenuation caused by multiple intermediate buildings of equal height, with $W_s = W_r = W = 10\ m, H_s = H_i = H_r = 9.6\ m$. *(a) Configuration; (b) Attenuation per canyon relative to no-canyon case. The error bar is the standard error extracted from all receivers in all configurations.*

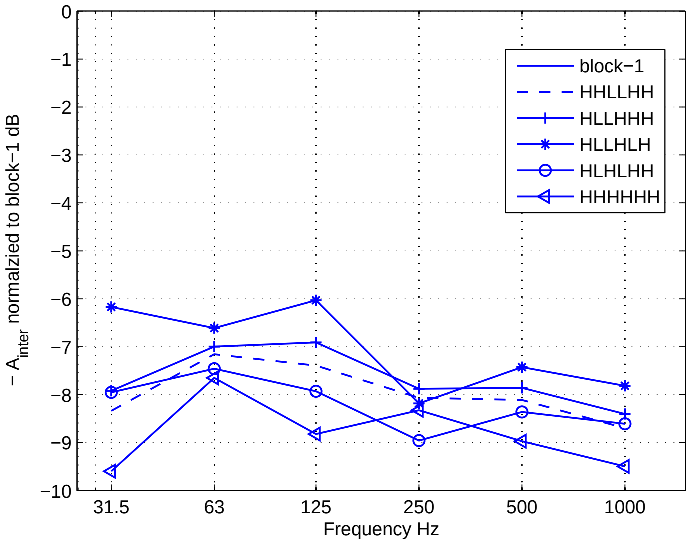

Figure 2.9: Intermediate canyon effect for different variations in the sequence of heights of intermediate buildings between source and receiver. See Fig. 2.8 for a description of Block-1. The curves are relative to the attenuation of a single large building of equal total length.

2.4.2 Comparison with the measurement

At these measurement locations of this study, road traffic noise was the main source of environmental noise exposure. The officially approved noise maps made for the agglomeration of Ghent in the framework of the END were used as the parent noise map. In this noise mapping, one reflection and one diffraction from vertical obstacle were considered. The traffic intensity and speed come from the official statistical department and the traffic on minor roads inside the city comes from the traffic simulation. The same traffic intensity and traffic composition database (i.e. a combination of traffic counts and traffic flow modeling) as used for the END map was used for the background noise mapping calculations. The building coordinates and the heights are extracted from a GIS system. The mean height of the buildings in the calculation zone is 10.9 m with std= 4.50 m. The quiet façade nodes are all located in residential zones inside the city and could be affected by human activities other than traffic noise. Therefore the time window was limited to 9:00 to 17:00 when the inhabitants of the house where the measurement equipment is installed are at work and traffic noise levels are considerable. For simplicity this value is still referred to as L_{day}. The measurement locations are chosen in such a way that continuous noise sources such as ventilation or cooling units are not present. Finally, a long observation period is considered to average out occasional gardening, cleaning, or rebuilding activities. Measured data during 90 days lead to convergence of the energetically averaged L_{day} noise exposure indicator at all locations considered. All traffic noise sources up to 1500 m from each receiver were considered in the calculations. Figure 2.10 shows 9 measurement positions used for the validation and their locations on the map. The measurements, the END-reported noise levels and the predicted levels based on the background noise mapping concept are shown in figure 2.11. The distance from the measurement microphones to the wall is in most cases less than 20 cm, so a correction for the façade reflection is necessary. For the most exposed façade, the correction should be between 0 to 6 dB according to some in-situ measurement [33]. However, in historically grown cities, such as Gent, the most exposed road can be small and a nearby major road may affect the sound pressure level considerably. Besides, the roughness and the architectural style make the correction for this reflection difficult to quantify. The roughness may scatter and diffract the sound propagating over the roof and cause the correction to be smaller than the literature study, such as [33]. Some measurement nodes are mounted on the back façade, the situation becomes then even more complicated. If the traffic uniformly distributes around the shielded yard, the sound field there is close to being diffuse. Therefore, the correction for the back façade microphone is also smaller than usual. Considering all above reasons, 3 dB is subtracted from the measurement to account for the direct and reflected waves near the façades for very low frequencies(< 250 Hz) [33, 34]. Position 6, 8, and 9 are inside an enclosed yard and other positions

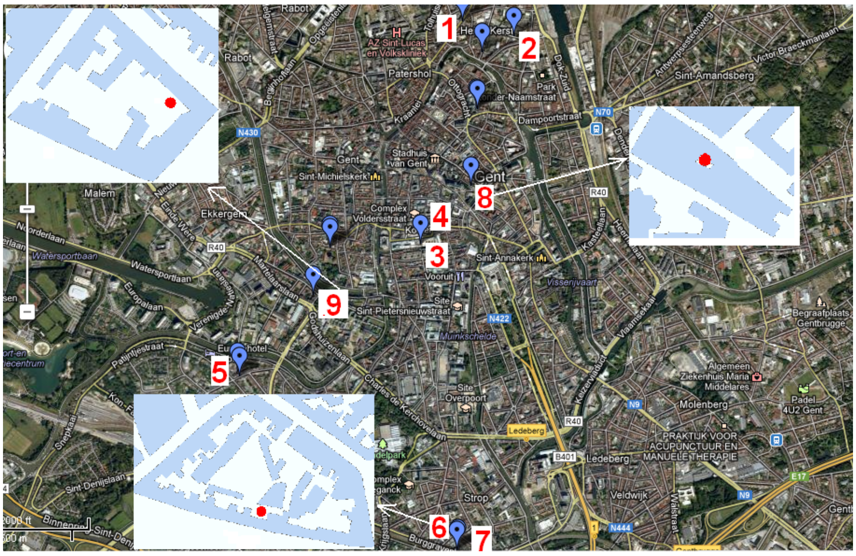

Figure 2.10: Measurement positions of Ghent city, Belgium.

are at a directly exposed façades. The sound spectrum at the totally shielded positions are shown in figure (2.12, 2.13, 2.14). The results show that the noise levels of L_{day} calculated by the END noise map are close to the measured levels in the directly exposed façades(except for position 4), but clearly underestimate levels at the shielded façades. In position 9, this difference exceeds 14 dBA. At shielded locations, the A_{can} term significantly improves the noise level spectrum predictions at low frequencies but not at high frequencies. Adding a turbulent scattering contribution becomes therefore essential and the engineering model as described in detail in [10] was used. Applying the background noise mapping concept still leads to an underestimation at position 8, although an important improvement is made compared to the END map. At this specific small enclosed courtyard in the traffic free inner city, traffic noise hardly contributes to the observed noise level during the day.

At the most exposed façades, some difference between the measurements and the calculated levels for the END map could be attributed to e.g. inaccuracies in traffic data. Also the measurement error should be mentioned, which is expected to be below 2 dBA for road traffic dominated environmental noise exposure [32].

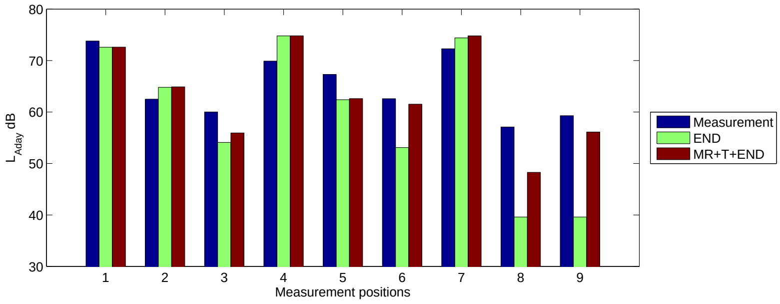

Figure 2.11: Comparison of predicted level and measurement. The legends "Measurement" indicates the measured L_{day}; "END" is the L_{day} calculated for the END map; "MR+T+END" uses the background noise mapping concept, including multiple reflections and the turbulence scattering model [10] applied to the END map predictions.

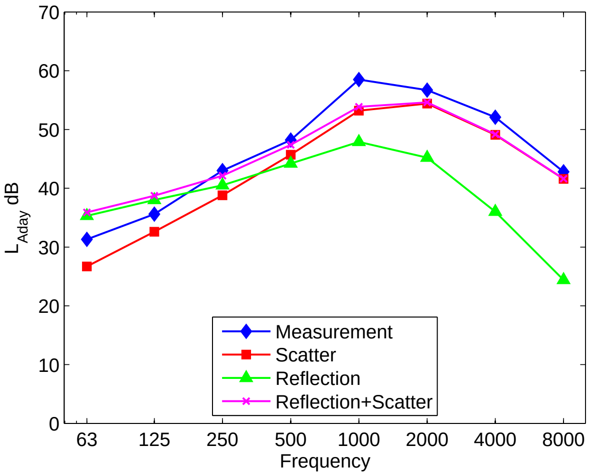

Figure 2.12: Spectrum of position 6. Legend "Scatter" is calculated by the model in [10]; "Reflection" is calculated by equation (2.2); "Reflection+Scatter" is calculated by equation (2.1) with $C_t^2 = 0.4K^2/m^{2/3}$ *and* $C_v^2 = 1.2m^{4/3}/s^2$. C_v *and* C_t *are the structure parameters of velocity and temperature fluctuations, respectively, describing their partial turbulence strengths.*

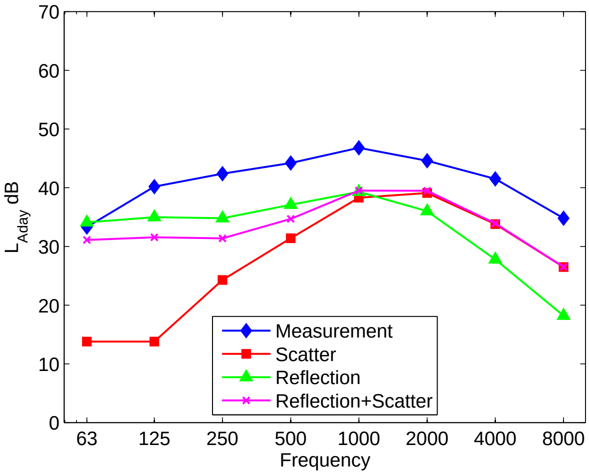

Figure 2.13: Spectrum of position 8.

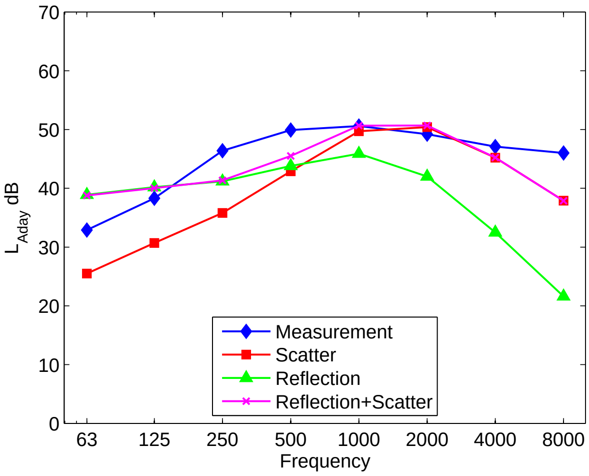

Figure 2.14: Spectrum of position 9.

2.5 Discussion of the turbulent strength

The turbulence strength varies considerably in different places at different time. The noise levels caused by the turbulence scattering are changed significantly. For the exposed façade, the direct sound usually dominates the noise levels, however, for the shielded places, different turbulence strength would lead to big predicting errors. Measurements show that the fluctuation of the turbulence strength has limited effect on low frequencies, meanwhile, the influence to high frequencies are obvious [35]. The general model presented in this study has very well prediction accuracy in low frequencies (≤1000 Hz) and its predicting only depends on the geometrical information and absorbing properties of buildings and streets. This is an obvious advantage to have stable and accurate prediction for low frequencies. For the correction of high frequencies (>1000 Hz) at shielded positions, the turbulent scattering would dominate. Since the fluctuation of the turbulence strength, a dynamically predicting strategy is needed which will be discussed in the following chapters.

2.6 Conclusions

An engineering model for improving noise level predictions at shielded locations in an urban noise map is presented, based on a large set of 2D full-wave numerical calculations of canyon-to-canyon propagation. The engineering model for background noise mapping proposed here can be used to improve existing noise maps with a poor prediction at shielded zones. In this model, different attenuation terms, A_{bar}, A_{can}, and A_{inter} are quantified separately, which opens possibilities to add more correction terms, such as terms to explicitly account for refraction by wind and temperature gradients. Another advantage is that the inputs of the model are only geometrical parameters of the canyons, buildings, sources and receivers. Such parameters are easily derived from common GIS systems. A comparison between predicted levels and long-term measurements, shows that the model performs well in predicting total L_{day} and the compatibility of the background noise mapping concept with existing noise maps is illustrated. Especially at shielded building façades, predictions are strongly improved.

Acknowledgment

We gratefully appreciate the financial support of the Life+ program of the European Community (project QSIDE, LIFE09 ENV/NL/000423).

Appendix A2: Analytic form for $A_{can,flat}$

To derive the general form of the analytic expression that will be fitted to the numerical results, diffraction over the central building from multiple image sources in the source canyon to multiple image receivers in the receiver canyon is studied. The total squared sound pressure at the receiver caused by all of these propagation paths is summed. The total contribution is:

$$\sum_{a=0}^{\infty}\sum_{b=0}^{\infty}\left|p_{a,b}\right|^2 = \left|p_{0,\,0}\right|^2 + \sum_{a=1}^{\infty}\left|p_{a,0}\right|^2 + \sum_{b=1}^{\infty}\left|p_{0,b}\right|^2 + \sum_{a=1}^{\infty}\sum_{b=1}^{\infty}\left|p_{a,b}\right|^2 \tag{2.15}$$

where the subscript indicates the position of the source, the receiver and the image sources and image receivers, i.e. $a = 0$ indicates the source position and $b = 0$ indicates the receiver position; the $a = 1, 2, 3...$ indicates different image sources; similarly, $b = 1, 2, 3...$ indicates different image receivers. $\left|p_{0,\,0}\right|^2$ contains the part of the squared sound pressure at the receiver, emitted by the source and diffracted directly over the building. This term is included in $A_{bar,flat}$. $\sum_{a=1}^{\infty}\left|p_{a,\,0}\right|^2$ indicates the total squared sound pressure at the receiver position, emitted by all the image sources. $\sum_{b=1}^{\infty}\left|p_{0,\,b}\right|^2$ indicates the squared sound pressure emitted by the source and received by all the image receivers (i.e. located at the image receiver positions). $\sum_{a=1}^{\infty}\sum_{b=1}^{\infty}\left|p_{a,b}\right|^2$ indicates the total sound pressure square at all the image receiver positions, emitting by all the image sources. For each of these three terms, an analytic expression is derived below.

A2.1 Analytic solutions of $\sum_{a=1}^{\infty}\left|p_{a,\,0}\right|^2$ and $\sum_{b=1}^{\infty}\left|p_{0,\,b}\right|^2$

Image sources will occur in the direction away from the intermediate building and in the direction of this building. Because the diffraction angle is much larger and the distance is comparable for the latter set, it can easily be shown that these can be neglected. Thus the derivation can focus on the image sources positioned away from the intermediate building. A few assumptions are listed before hand. The first assumption is that the buildings are not very low (>4 m). Accordingly, the decay caused by the finite size of the reflecting surface that could be expressed as a decaying overlap between the surface and the Fresnel zone can be ignored even after many reflections. This decay will be considered in a fitting coefficient later. A second assumption is that the building height of the source canyon and receiver canyon are the same. As a result, the image sources can reach the receiver or image receivers by double diffraction. Afterwards, other conditions such as, $H_s < H_i$, $H_r < H_i$, $H_s > H_i$ and $H_r > H_i$ will be studied. With the above assumptions and equation (2.4), the square of the sound pressure generated by the *a*th image source is: $\left|p_{a,0}\right|^2 = \left(\frac{0.37}{X_{a,1}+0.37}\right)^2\left(\frac{0.37}{X_{a,2}+0.37}\right)^2\left|p_{at,L_a}\right|^2$. For a point source, the sound pressure at distance L_a is $p_{at,L_a} = \frac{\rho_s^a A}{4\pi L_a}e^{-jkL_a}$, where A is the amplitude and ρ_s

is the reflection coefficient in the source canyon. Note that in accordance with the diffraction theory L_a is the shortest path between source and receiver around the diffracting elements. Then the sum of $p_{a,0}$ is:

$$\sum_{a=1}^{\infty}|p_{a,0}|^2 = \sum_{a=1}^{\infty}\left|\frac{\rho_s^a A}{4\pi}\right|^2\left|\frac{1}{L_a}\right|^2\left(\frac{0.37}{X_{a,1}+0.37}\right)^2\left(\frac{0.37}{X_{a,2}+0.37}\right)^2 \tag{2.16}$$

In a general case, $X_s = M_{\nu s}\gamma_s = \sqrt{\frac{2r_{a,s}(r_r+W)}{r_{a,s}+r_r+W}}\sqrt{3}\left(\cos\frac{2}{3}\theta_{a,s}-0.5\right)$. For $\theta_{a,s}$ in the range between 0 and $\pi/2$, which is the shielded area, $\cos\frac{2}{3}\theta_{a,s} - 0.5$ can be approximated by $0.5\cos\theta_{a,s}$ which is calculated as $0.5h_1/r_{a,s}$. It can easily be verified that this approximation introduces a very small error, $std = 0.0056$ in more than 1500 checking samples. As a result, X_s and X_r can be simplified as:

$$X_{a,s} \approx \sqrt{\frac{2r_{a,s}\left(r_r+W\right)}{r_{a,s}+r_r+W}}\frac{\sqrt{3}}{2}\cos\theta_{a,s} = \sqrt{\frac{2r_{a,s}\left(r_r+W\right)}{r_{a,s}+r_r+W}}\frac{\sqrt{3}}{2}\frac{h_1}{r_{a,s}}; \tag{2.17}$$

$$X_{a,r} \approx \sqrt{\frac{2r_r\left(r_{a,s}+W\right)}{r_{a,s}+r_r+W}}\frac{\sqrt{3}}{2}\cos\theta_{a,r} = \sqrt{\frac{2r_r\left(r_{a,s}+W\right)}{r_{a,s}+r_r+W}}\frac{\sqrt{3}}{2}\frac{h_2}{r_r}; \tag{2.18}$$

According to the diffraction theory, the factor B has to be multiplied with the smallest of the two X terms. Therefore we have a closer look at the ratio $X_{a,s}/X_{a,r}$ which is $\frac{h_1}{h_2}\sqrt{\frac{r_r(r_r+W)}{r_{a,s}(r_{a,s}+W)}}$. Considering that the receiver is generally higher than the source and that all façades of buildings have the same height, $h_1 > h_2$. In most cases it can be shown that this ratio is less than 1 after a few reflections, since $r_{a,s} \gg r_r$ is expected. For deducing an analytic form for $A_{can,flat}$, all $X_{a,s}$ are supposed to be less than X_r. As a result, $X_{a,1} = X_{a,s}B$ and $X_{a,2} = X_r$.

Let us now consider the second term in equation (2.16) which we call C_{1s} for convenience:

$$\begin{aligned} C_{1s} = \left(\frac{0.37}{X_{a,2}+0.37}\right)^2 &\approx \left[\frac{0.37}{\sqrt{\frac{2r_r(W+r_{a,s})}{\lambda(r_{a,s}+W+r_r)}}\frac{\sqrt{3}}{2}\cos\theta_r+0.37}\right]^2 \\ &\approx \left[\frac{0.37}{\sqrt{\frac{2r_r}{\lambda}}\frac{\sqrt{3}}{2}\cos\theta_r+0.37}\right]^2 \end{aligned} \tag{2.19}$$

which becomes independent of a when it can be assumed that $W + r_{a,s} \gg r_r$, which is the case for higher order reflections at least. The remaining part of equation (2.16) can be rewritten as:

$$\left|\frac{1}{L_a}\right|^2 \left(\frac{0.37}{X_{a,1}+0.37}\right)^2 \approx \left[\frac{0.37}{\sqrt{\frac{2r_{a,s}W}{\lambda(W+r_{a,s})}}\frac{\sqrt{3}}{2}\cos(\theta_{a,s})L_a + 0.37L_a}\right]^2$$

$$= \left[\frac{1}{\sqrt{\frac{2W(r_{a,s}+W+r_r)}{\lambda(r_{a,s}+W)}}\frac{\sqrt{3}}{0.74}h_1\sqrt{\frac{(r_{a,s}+W+r_r)}{r_{a,s}}} + (r_{a,s}+W+r_r)}\right]^2 \qquad (2.20)$$

Again assuming that $r_{a,s} + W \gg r_r$, the first square root term simplifies and becomes independent of the reflection order a. $\sqrt{\frac{(r_{a,s}+W+r_r)}{r_{a,s}}}$ is difficult to handle but fortunately assuming that it is close to 1 introduces at most 3 dB of error for the $r_{a,s}$ and W that can be expected in an urban setting. The reader should keep in mind that the purpose of this derivation is to extract an analytic form with coefficients that will be fitted on numerical simulation results. As a result of these approximations, the total sum of equation (2.16) is reduced to:

$$\sum_{a=1}^{\infty} |p_{a,0}|^2 = C_{1s}\sum_{a=1}^{\infty}\left|\frac{\rho_s^a A}{4\pi}\right|^2 \left(\frac{1}{\sqrt{\frac{2W}{\lambda}}\frac{\sqrt{3}}{0.74}h_1 + r_{a,s} + W + r_r}\right)^2 \qquad (2.21)$$

The first term in the denominator is independent of the image source index a. This implies that the approximations made above boil down to assuming that the effect of increasing distance from the image source to the diffraction edge is neatly compensated by the effect of changing diffraction angle. To simplify the sum further it is now assumed that the source is positioned in the middle of the canyon and that when $r_{a,s}$ becomes large compared to the height of the canyon above the source h_1, its value can approximated by $r_{a,s} \approx d_a$, where $d_a = a * W_s + 0.5W_s$ is the horizontal distance from the ath image source to the edge of the building façade. In this case, the sum is a special function:

$$\sum_{a=1}^{\infty} |p_{a,0}|^2 = C_{1s}\left|\frac{A}{4\pi}\right|^2 \frac{\rho_s^2}{W_s^2}\Phi\left(\rho_s^2, 2, \frac{C_{3s}+W_s}{W_s}\right) \qquad (2.22)$$

where $C_{3s} = \sqrt{\frac{2W}{\lambda}}\frac{\sqrt{3}}{0.74}h_1 + 0.5W_s + r_r + W$. Φ is the Hurwitz-Lerchi transcendent. Until now it was assumed that the flanking building creating the source street canyon was very high so that all reflections were possible. However, when $H_s < H_i$, the sound emitting from some of the left image sources cannot contribute to the receiver and the contribution of the image sources from the right side start becoming stronger. The sound will need to diffract three times to reach the receiver

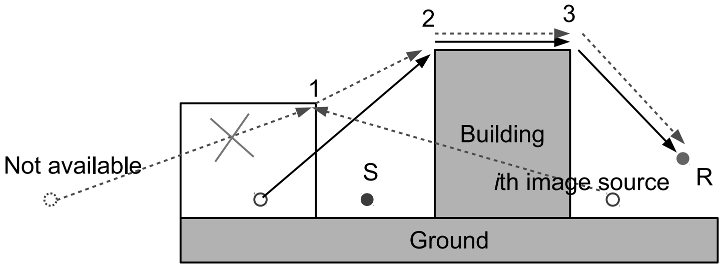

Figure 2.15: Demonstration of contributed image sources.

and follows the route "image source → 1 → 2 → 3 →receiver" to reach the receiver position, as shown in figure 2.15.

After one more diffraction, the sound power decreases significantly, which can be accordingly ignored. When H_s is not much smaller than H_i, the sound from the first few important images sources can still reach the receiver position by double diffraction following the routine "image source → 2 → 3 →receiver", as shown in figure 2.15. Under this condition and neglecting high order diffraction, the total contribution of the image sources is approximated by:

$$\begin{aligned}\sum_{a=1}^{N} |p_{a,0}|^2 = \sum_{a=1}^{\infty} |p_{a,0}|^2 - \sum_{a=N+1}^{\infty} |p_{a,0}|^2 = C_{1s}\left|\frac{A}{4\pi}\right|^2 \frac{\rho_s^2}{W_s^2}\Phi\left(\rho_s^2, 2, \frac{C_{3s}+W_s}{W_s}\right) \\ - \quad C_{1s}\left|\frac{A}{4\pi}\right|^2 \frac{\rho_s^{2(N+1)}}{W_s^2}\Phi\left(\rho_s^2, 2, N+1+\frac{C_{3s}}{W_s}\right)\end{aligned} \tag{2.23}$$

where N is the number of images sources which can reach the receiver by only two diffraction corners. As expected, the higher H_s is the larger N is. When $H_s = H_i$, N becomes infinite. The number of visible image sources, N, is the most important parameter to determine the difference between the level calculated using equation (2.23) and equation (2.22). Other parameters, such as W_s, W and λ can still affect this level difference slightly. To avoid calculating N for every source position in the canyon, N is proposed using the assumption that the source is in the middle of the canyon and categorize situations according to the ratio of $(H_s - h_s)/(H_i - h_s)$, where h_s is the height of the source. The relation can be written as: $H_s - h_s = \frac{2N-1}{2N+1}(H_i - h_s)$ for a source in the middle of the source canyon. Specifically, when $N = [1, 2, 3, \cdots]$ corresponds to the ratio $(H_s - h_s)/(H_i - h_s) \le [1/3, 3/5, 5/7 \cdots]$. When $(H_s - h_s)/(H_i - h_s) \le 1/3$, no image sources are available from the left side and the canyon effect can be neglected. L_{hs} is set to $-\infty$. When $1/3 < (H_s - h_s)/(H_i - h_s) \le 3/5$, only the first image source from the left side can contribute and $\sum |p_{a,0}|^2 = 10^{(-0.1 A_{bar,flat})}$ with the "source position" being at the first image source; when $3/5 < (H_s - h_s)/(H_i - h_s)$, more than one image source from the left side are available, an approximation of the level difference between equation (2.23) and equation (2.22) is: $L_{hs} = -6.17\left(1 - \frac{H_s - h_s}{H_i - h_s}\right)\left[1 - 1.37\log_{10}\left(\frac{\sqrt{\lambda W_s}}{W}\right)\right]$ dB which is fitted on the condition of $W_s \in [15, 100], W \in [20, 500], H_i = 18$ m and Frequency $\in [60, 8000]$Hz. When $\frac{H_s - h_s}{H_i - h_s} > 1$, $L_{hs} = 0$.

When $H_s > H_i$, in most cases the important contribution comes from the sound from the image sources diffracting twice over the middle building. In some extreme cases, when H_s is high, H_i is low and W is narrow, sound could reach the receiver after only one reflection on the edge of the building of height H_s. Since this condition is not common, its effect is ignored when extracting the analytic form of the functions used for fitting. Without the numerical constant, the fitting formula for $\sum_{a=1}^{\infty} |p_{a,0}|^2$ is:

$$\begin{aligned} \sum_{a=1}^{\infty} |p_{a,0}|^2 &\approx F(1)\left[C_{1s}\frac{\rho_s^2}{W_s^2}\Phi\left(\rho_s^2, 2, \frac{C_{3s} + W_s}{W_s}\right)10^{0.1L_{hs}}\right] \\ &\quad if\frac{3}{5} < \frac{H_s - h_s}{H_i - h_s} \le 1 \end{aligned} \tag{2.24}$$

where $F(1)$ is a fitting coefficient. Similarly, the $\sum_{b=1}^{\infty} |p_{0,b}|^2$ could also be obtained.

$$\begin{aligned} \sum_{b=1}^{\infty} |p_{0,b}|^2 &\approx F(2)\left[C_{1r}\frac{\rho_r^2}{W_r^2}\Phi\left(\rho_r^2, 2, \frac{C_{3r} + W_r}{W_r}\right)10^{0.1L_{hr}}\right] \\ &\quad if\frac{3}{5} < \frac{H_r - h_r}{H_i - h_r} \le 1 \end{aligned} \tag{2.25}$$

where $F(2)$ is the fitting coefficient, h_r is the height of the receiver, ρ_r is the average reflection coefficient of the façade in the receiver canyon and other parameters are as follows:

$$\begin{aligned} L_{hr} &= -6.17\left(1 - \frac{H_r - h_r}{H_i - h_r}\right)\left[1 - 1.37\log_{10}\left(\frac{\sqrt{\lambda W_r}}{W}\right)\right] \\ C_{1r} &\approx \left(\frac{0.37}{\sqrt{\frac{2r_s}{\lambda}}\frac{\sqrt{3}}{2}\cos\theta_s + 0.37}\right)^2 \\ C_{3r} &= \sqrt{\frac{2W}{\lambda}}\frac{\sqrt{3}}{0.74}h_2 + 0.5W_r + r_s + W \end{aligned}$$

Similarly, when $\frac{H_r - h_r}{H_i - h_r} < 1/3$, the canyon effect is neglected and L_{hr} is set to $-\infty$; when $1/3 < \frac{H_r - h_r}{H_i - h_r} < 3/5$, $\sum_{b=1}^{\infty} |p_{0,b}|^2 = 10^{-0.1A_{bar,flat}}$. In a special case when $H_i = h_r$, the canyon effect is neglected as well.

To quantify the effect of the finite size of an object on the amount of the reflected acoustic energy, the envelope of the object and the Fresnel ellipsoid should be calculated. The source height of a vehicle is often close to the ground which implies that half of the section of the ellipsoids is below the building façade. If the reflections on the ground are considered, its contribution can be treated as an image source. As a result, the Fresnel zone can only cause decay when the radius of the Fresnel ellipsoids is greater than H_s or H_i. If the radius $\sqrt{\lambda D}/2 \leq H_s$, the sound energy will be totally reflected, where D equals twice the distance of the image source which is $D = 2(aW_s + 0.5W_s)$. If $H_s = 12$ m (corresponding to a 3-floors building), $W_s = 15$ m (appears frequently in Gent), the Fresnel zone starts to cause decay after 10 and 112 reflection for $\lambda = 3.4$ m(corresponding to 100Hz) and $\lambda = 0.34$ m(corresponding to 1000Hz) respectively. It can be concluded that the decay speed is much less than the decay caused by the absorption of the façade. which decays by power function and the absorption starts to decay from the first reflection.

For the receiver canyon, it is difficult to make accurate estimation considering the receiver height is often at 4 m. Suppose $H_s = 10$ m, $H_i = 10$ m, $W_s = 12$ m, The decay starts from 2 for 100Hz and 20 for 1000Hz. Although the decay due to the Fresnel ellipsoid depends differently on the reflection area, it is decided to include its effect by increasing the average contribute of the façade.

A2.2 Approximation of $\sum_{a=1}^{\infty}\sum_{b=1}^{\infty}|p_{a,b}|^2$

The double sum can be written as a sum of single sums for the source canyons for example. It is already known that the sum over all image sources results in the Hurwitz-Lerchi transcendent, but it is not possible to convert the sum over these special functions to a closed form. In the next step, the Hurwitz-Lerchi transcendent Φ is approximated by $G(\rho_s, x) = K\rho_s^2/x^2$. In the region $x \in (5, 20]$, $\rho_s \in [0.8, 1]$, this approximation with $K = 1.59$ results in a mean squared error of 0.0034, which is acceptable. Because the solution of every sum $\sum_{a=b}^{\infty}|p_{a,b}|^2$ is similar as equation (2.22), the double sum can be generally written as:

$$\sum_{a=1}^{\infty}\sum_{b=1}^{\infty}|p_{a,b}|^2 = 10^{0.1L_{hs}}10^{0.1L_{hr}}\left|\frac{A}{4\pi}\right|^2\sum_{b=1}^{\infty}C_{1s,b}\frac{\rho_s^2\rho_r^{2j}}{W_s^2}\Phi\left(\rho_s^2, 2, \frac{C_{3s,b}+W_s}{W_s}\right) \tag{2.26}$$

where $C_{3s,b} = \sqrt{\frac{2W}{\lambda}}\frac{\sqrt{3}}{0.74}h_1 + 0.5W_s + r_{b,r} + W$. It should be mentioned that while deriving this equation, it was assumed that $r_{a,s} \gg r_{b,r}$ which may not hold for high order receiver reflections. According to the approximation mentioned in this section, equation (2.26) changes to:

$$\sum_{a=b}^{\infty}\sum_{a=1}^{\infty}|p_{a,b}|^2 = 1.59\rho_s^6 10^{0.1L_{hs}}10^{0.1L_{hr}}\left|\frac{A}{4\pi}\right|^2 \sum_{b=1}^{\infty}\left(\frac{0.37}{\sqrt{\frac{2r_{b,r}}{\lambda}}\frac{\sqrt{3}}{2}\cos\theta_{b,r}+0.37}\right)^2\left(\frac{1}{C_{3s,b}+W_s}\right)^2 \tag{2.27}$$

For high order image receivers, $\left(\frac{0.37}{\sqrt{\frac{2r_{b,r}}{\lambda}}\frac{\sqrt{3}}{2}\cos\theta_{b,r}+0.37}\right)^2 = \left(\frac{0.37}{3.31h_1/\sqrt{\lambda r_{b,r}}+0.37}\right)^2 \rightarrow 1$. As a result, the above equation approximates to:

$$\begin{aligned}\sum_{a=1}^{\infty}\sum_{b=1}^{\infty}|p_{a,b}|^2 &< 1.59\rho_s^6\left|\frac{A}{4\pi}\right|^2 10^{0.1L_{hs}}10^{0.1L_{hr}}\sum_{b=1}^{\infty}\left(\frac{1}{C_{3s,b}+W_s}\right)^2 \\ &= \left|\frac{A}{4\pi}\right|^2 10^{0.1L_{hs}}10^{0.1L_{hr}}1.59\rho_s^6\frac{\rho_r^2}{W_r^2}\Phi\left(\rho_r^2, 2, \frac{3.31h_1/\sqrt{\lambda}+1.5W_s+W+1.5W_r}{W_r}\right) \\ &\approx \left|\frac{A}{4\pi}\right|^2 10^{0.1L_{hs}}10^{0.1L_{hr}}\rho_s^6\rho_r^6\left(\frac{1.59}{3.31h_1/\sqrt{\lambda}+1.5W_s+W+1.5W_r}\right)^2 \end{aligned}\tag{2.28}$$

The asymmetry is caused by the above assumption. If we calculate the double sum from the receiver canyon, a similar form could be achieved only replacing "h_1" by "h_2". To moderate this error, the average of the two calculations is used to approximate the double sum by:

$$\sum_{a=b}^{\infty}\sum_{a=1}^{\infty}|p_{a,b}|^2 \approx \frac{\left|\frac{A}{4\pi}\right|^2(1.59)^2 10^{0.1L_{hs}}10^{0.1L_{hr}}\rho_s^6\rho_r^6}{(\frac{3.31h_1}{\sqrt{\lambda}}+1.5W_s+W+1.5W_r)(\frac{3.31h_2}{\sqrt{\lambda}}+1.5W_s+W+1.5W_r)} \tag{2.29}$$

References

[1] E. Öhrström, A. Skånberg, H. Svensson, and A. Gidlöf-Gunnarsson. *Effects of road traffic noise and the benefit of access to quietness*. J. Sound Vib., 295:40–59, 2005.

[2] E. Öhrström. *Psycho-social effects of traffic noise exposure*. J. Sound Vib., 151(3):513–517, 1991.

[3] Yvonne de Kluizenaar, Erik M. Salomons, Sabine A. Janssen, Frank J. van Lenthe, Henk Vos, Han Zhou, Henk M. E. Miedema, and Johan P. Mackenbach. *Urban road traffic noise and annoyance: The effect of a quiet facade*. J. Acoust. Soc. Am., 130(4):1936–1942, 2011.

[4] Timothy Van Renterghem and Dick Botteldooren. *Focused Study on the Quiet Side Effect in Dwellings Highly Exposed to Road Traffic Noise*. International Journal of Environmental Research and Public Health, 9(12):4292–4310, November 2012.

[5] Frits Van den Berg, Carlo Schoonebeek, and Menno Hillebregt. *On the definitions of quiet faades and quiet urban areas*. In Proc. of Euronoise 2012, Prague, Prague, Czech, August 2012.

[6] Mikael Ögren and Jens Forssén. *Modelling of a city canyon problem in a turbulent atmosphere using an equivalent sources approach*. Appl. Acoust., 65:629–642, 2004.

[7] Maarten Hornikx and Jens Forssén. *The 2.5-dimensional equivalent sources method for directly exposed and shielded urban canyons*. J. Acoust. Soc. Am., 122:2532–2541, 2007.

[8] Timothy Van Renterghem and Dick Botteldooren. *Prediction-step staggered-in-time FDTD: An efficient numerical scheme to solve the linearised equations of fluid dynamics in outdoor sound propagation*. Appl. Acoust., 68:201–216, 2007.

[9] Dick Botteldooren. *Finite-difference time-domain simulation of low-frequency room acoustic problems*. J. Acoust. Soc. Am., 98:3302–3308, 1995.

[10] Jens Forssén, Maarten Hornikx, T. Van Renterghem, W. Wei, D. Botteldooren, and M. Ögren. *Urban background noise mapping: the turbulence scattering model*. Submitted to Acta Acust. United Ac, 2013.

[11] Jérôme Defrance, Erik Salomons, Ingrid Noordhoek, Dietrich Heimann, Birger Plovsing, Greg Watts, Hans Jonasson, Xuetao Zhang, Eric Premat, Isabelle Schmich, François Aballea, Marine Baulac, and Foort de Roo. *Outdoor Sound Propagation Reference Model Developed in the European Harmonoise Project*. Acta Acust. Acust., 93:213–227, 2007.

[12] *Environmental Noise and the CNOSSOS-EU initiative*, 2012.

[13] Timothy Van Renterghem, Erik Salomons, and Dick Botteldooren. *Parameter study of sound propagation between city canyons with coupled FDTD-PE model*. Appl. Acoust., 67(9):487–510, 2006.

[14] Maarten Hornikx, Jens Forssén, T. Van Renterghem, D. Botteldooren, W. Wei, M. Ögren, and Erik Salomons. *Urban background noise mapping: the multiple-reflection correction term*. Submitted to Acta Acust. United Ac, 2013.

[15] J. Kang. *Urban Sound Environment*. Taylor & Francis incorporating, Spon, London, 2007.

[16] Christopher Torrence and Gilbert P. Compo. *A Practical Guide to Wavelet Analysis*. B. Am. Meteorol. Soc., 79:61–78, 1998.

[17] Maarten Hornikx and Jens Forssén. *A scalemodel study of parallel urban canyons*. Acta Acust. Acust., 94:265–281, 2008.

[18] Timothy Van Renterghem, Erik Salomons, and Dick Botteldooren. *Efficient FDTD-PE Model for Sound Propagation in Situations with Complex Obstacles and Wind Profiles*. Acta Acust. Acust., 91:671–679, 2005.

[19] Kurt Heutschi. *Calculation of Refelctions in an Urban Environment*. Acta Acust. Acust., 95:644–652, 2009.

[20] Timothy Van Renterghem and Dick Botteldooren. *Meteorological influence on sound propagation between adjacent city canyons: A real-life experiment*. J. Acoust. Soc. Am., 127(6):3335–3346, 2010.

[21] Allan D. Pierce. *Diffraction of sound around corners and over wide barriers*. J. Acoust. Soc. Am., 55(5):941–955, 1974.

[22] Allan D. Pierce. *Acoustics: An Introduction to Its Pysical Principles and Applications*. Acoustical Society of America, New York, USA, 1989.

[23] T. Kawai. *Sound Diffraction by a Many-Sided Barrier or Pillar*. J. Sound Vib., 79(2):229–242, 1981.

[24] Hyun-Sil Kim, Jae-Sueng Kim, Hyun-Ju Kang, Bong-Ki Kim, and Sang-Ryul Kim. *Sound diffraction by multiple wedges and thin screens*. Applied Acoustics, 66(9):1102–1119, September 2005.

[25] N.N. Lebedev. *Special Functions and their Applications*. Dover Publications, Inc., 1972.

[26] Timothy Van Renterghem and Dick Botteldooren. *The importance of roof shape for road traffic noise shielding in the urban environment*. J. Sound Vib., 329(9):1422–1434, 2010.

[27] Martin Schiff, Maarten Hornikx, and Jens Forssén. *Excess attenuation for sound propagation over an urban canyon*. Applied Acoustics, 71(6):510–517, 2010.

[28] Mikael Ögren and Jens Forssén. *Road traffic noise propagation between two dimensional city canyons using an equivalent source approach*. Acta Acust. Acust., 90:293–300, 2004.

[29] M Almgren. *Simulation by using a curved ground scale model of outdoor sound propagation under the influence of a constant sound speed gradient*. Journal of sound and Vibration, 118(2):353–370, 1987.

[30] Pontus J. Thorsson, Mikael Ögren, and Wolfgang Kropp. *Noise levels on the shielded side in cities using a flat city model*. Appl. Acoust., 65:313–323, 2004.

[31] Timothy Van Renterghem and Dick Botteldooren. *In-situ measurements of sound propagating over extensive green roofs*. Building and Environment, 46(3):729–738, 2011.

[32] Timothy Van Renterghem, Pieter Thomas, Frederico Dominguez, Samuel Dauwe, Abdellah Touhafi, Bart Dhoedt, and Dick Botteldooren. *On the ability of consumer electronics microphones for environmental noise monitoring*. Journal of environmental monitoring: JEM, 13(3):544–552, March 2011. PMID: 21157618.

[33] G Memoli, M Paviotti, S Kephalopoulos, and G Licitra. *Testing the acoustical corrections for reflections on a façade*. Applied Acoustics, 69(6):479–495, 2008.

[34] Siu Hong Tang and Kai Ming Li. *The prediction of façade effects from a point source above an impedance ground*. The Journal of the Acoustical Society of America, 110(1):278–288, 2001.

[35] Timothy Van Renterghem, Weigang Wei, Jens Forssén, Maarten Hornikx, Mikael Ögren, and Erik Salomons. *Improving the accuracy of engineering models at shielded building facades : experimental analysis of turbulence scattering*. pages 5–9.

3

Simplified analytical model for sound level prediction at shielded urban locations involving multiple diffractions and reflections

★★★

Submitted to The Journal of the Acoustical Society of America

A simplified method is presented to predict sound levels at shielded urban locations, including multi-edge diffraction over successive buildings and multiple reflections between parallel façades. The model is essentially based on Pierce's diffraction theory, where the Fresnel Integral is approximated by trigonometric functions for efficient evaluation, and parametrized for urban environments. The model has been evaluated for idealized urban configurations by comparing to the results of Pierce's theory and the full-wave numerical method. In case of multi-edge diffraction over buildings in absence of a source or receiver canyon, deviations from the full-wave simulations are smaller than 2 dB for the octave bands with central frequencies ranging from 125 to 1000 Hz. However, larger errors are made when receivers are close to the extension line from the diffraction edge closest to the receiver. In case of combining the simplified multi-edge diffraction model with an efficient approach for including the series of mirror sources and mirror receivers, based on the Hurwitz-Lerch transcendent, a very similar accuracy is obtained.

3.1 Introduction

Predicting sound pressure levels at highly shielded areas, e.g. in the deep shadow zone of a conventional noise wall or at non-directly exposed façades and in courtyards in an urban setting, is a challenging sound propagation problem. Many researchers developed analytical, semi-analytical and empirical calculation strategies for sound diffracting over thin screens, thick screens and multi-edge objects [1, 2, 3, 4, 5, 6, 7, 8]. An explicit solution, aiming to solve the diffraction of line sources, can also be found in literature [9, 10]. In general, such models are able to well predict the diffracted sound fields. The reader is referred to some review articles [11, 12] for a detailed analysis of previously proposed models or some scale model studies [13, 14]. For application to urban noise maps, however, not only accuracy but also calculation speed is a major issue, making many of these previously cited approaches not well suited for this specific task. At the other hand, models allowing a fast evaluation are unable to predict sound pressure levels with a sufficient accuracy at highly shielded urban locations like e.g. the screening formula used in the ISO9613-2 model.

The diffraction formula used in this chapter is essentially based on Pierce's diffraction theory [3], where the Fresnel Integral is approached by trigonometric functions for efficient evaluation, and parametrized for typical urban environments as discussed by Wei et al. [15]. The model has been further evaluated in this chapter for general multi-edge diffraction problems.

In an urban environment, not only diffraction but also accounting for the multiple reflections in between opposing building façades could strongly increase the computational burden. As consequences, the number of reflections (and associated number of mirror sources and mirror receivers) is limited in most noise mapping efforts. However, that results in significant loss of accuracy. Previously, Heutschi[16] proposed look-up tables to predict urban street sound pressure levels based on source-receiver positioning and street geometry, while Thomas et al.[17] proposed to add the energy present in the reverberant part of the sound field based on regression analysis of a large dataset of measurements in urban streets. In this chapter, the reverberant field approach that underlies these developments, is extended to propagation towards a shielded area. Theoretical analysis of the mirror source series contributing to a shielded receiver is efficiently approached by parametrization.

The chapter is organized as follows. In the first part, the simplified diffraction formula as previously presented in Wei et al. [15] is repeated and additional validation is provided, including analysis of CPU evaluation time. In the second part, this diffraction approach is generalized to multiple edge diffraction. In the third part of this chapter, a method is proposed to include the effect of multiple reflections for sound propagation towards shielded urban locations.

3.2 A simplified method to calculate diffraction

3.2.1 Single diffraction at a rigid-wedge

According to previous studies [3, 5, 6, 18], the diffracted sound pressure is a product of a source term, a term related to propagation distance and a diffraction term. For a point source diffracted by a rigid wedge, the diffracted sound pressure then reads:

$$p_{diffr} = S_0 \frac{e^{ikL}}{L} D_1, \tag{3.1}$$

where, D_1 is the diffraction function which is a function of $\theta_{s,l}$, $\theta_{r,l}$, $r_{s,l}$, $r_{r,l}$ and β_l. The subscript 1 of D indicates diffraction happens at the 1^{st} edge. Clearly, in rigid-wedge diffraction $l = 1$, implying there is only one diffraction edge. L is the total length of the propagation path and S_0 is the strength of the source. In contrast for the diffraction function, the asymptotic solution of D in Pierce's [3] work seems most interesting to allow further simplification:

$$D_1(r_{s,1}, \theta_{s,1}, r_{r,1}, \theta_{r,1}, \beta) = \frac{e^{i\pi/4}}{\sqrt{2}} \left[A_D(X_+) + A_D(X_-)\right], \tag{3.2}$$

where $X_+ = \Gamma M_\nu(\theta + \theta_0)$, $X_- = \Gamma M_\nu(\theta - \theta_0)$, $\Gamma = \sqrt{2r_s r_r/[\lambda(r_r + r_s)]}$, $M_\nu(\theta) = \dfrac{\cos\nu\pi - \cos\nu\theta}{\nu\sin\nu\pi}$, $\nu = \pi/\beta$. Clearly, in this case $\theta_{s,1} = \theta_0$ and $\theta_{r,1} = \theta$. The definition of the angles is shown in figure (3.1). Other parameters are:

$$A_D(X) = \frac{\sqrt{2}}{2\pi} \int_{-\infty}^{\infty} \frac{e^{-u}}{X\sqrt{\frac{\pi}{2}} - e^{-i\pi/4}u} du = sign(X) \left[f(|X|) - ig(|X|)\right],$$

$$f(X) = [\frac{1}{2} - S(X)] \cos(\frac{1}{2}\pi X^2) - [\frac{1}{2} - C(X)] \sin(\frac{1}{2}\pi X^2), \tag{3.3}$$

$$g(X) = [\frac{1}{2} - C(X)] \cos(\frac{1}{2}\pi X^2) + [\frac{1}{2} - S(X)] \sin(\frac{1}{2}\pi X^2), \tag{3.4}$$

$$C(X) = \int_0^X \cos\left(\frac{1}{2}\pi t^2\right) dt,$$

$$S(X) = \int_0^X \sin\left(\frac{1}{2}\pi t^2\right) dt,$$

Although the Fresnel integrals can be solved rather easily nowadays, further simplification is still useful. If $X \gg 0$, the Fresnel Integral can be simplified as $C(X) \approx 0.5 + \frac{1}{\pi X} \sin\left(\frac{\pi}{2} X^2\right)$ and $S(X) \approx 0.5 - \frac{1}{\pi X} \cos\left(\frac{\pi}{2} X^2\right)$. However, in real urban cases, $x \to 0$ appears frequently, implying that $S(X) \approx 0.5 - \frac{1}{\pi X} \cos\left(\frac{\pi}{2} X^2\right)$

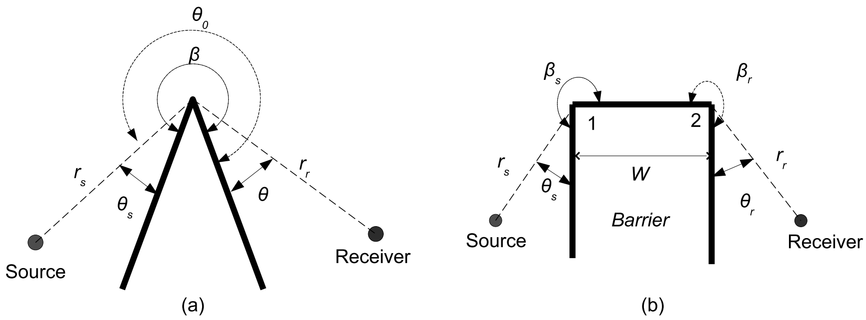

Figure 3.1: Geometry of single-wedge (a) and double-edge (b) diffraction.

has a strong singularity point at $X = 0$. The later means that this approximation can lead to big errors when X is close to 0. To avoid this singularity, the Fresnel Integrals are approximated by [15]:

$$C(X) \approx 0.5 + \frac{0.37}{0.37 + X} \sin\left(\frac{\pi}{2} X^2\right) \tag{3.5}$$

$$S(X) \approx 0.5 - \frac{0.37}{0.37 + X} \cos\left(\frac{\pi}{2} X^2\right) \tag{3.6}$$

The coefficient 0.37 is found by fitting to the solution of the Fresnel Integrals with typical urban geometrical inputs. The largest approximation error still appears when the receiver is on the reflection or shadow boundary, which is indicated by $X \rightarrow 0$ in figure (3.3). Figure (3.2), which is extracted from the urban structure of two European cities (the Gent City in Belgium and Katendrach, Rotterdam in the Netherlands), shows a typical distribution of X-values. Although for a considerable number of cases X is close to 0., the majority of the distribution corresponds to $X > 1$.

Substituting Eq. (3.5) and (3.6) into Eq. (3.3) and (3.4) leads to:

$$f(X) = \frac{0.37}{X + 0.37} \tag{3.7}$$

$$g(X) = 0 \tag{3.8}$$

Then the diffraction function Eq. (3.2) of a single rigid-wedge becomes:

$$D_1(r_s, \theta_{s,1}, r_r, \theta_{r,1}) = \frac{e^{i\pi/4}}{\sqrt{2}} \left[f(X_+) + f(X_-) \right] = \frac{e^{i\pi/4}}{\sqrt{2}} \left(\frac{0.37}{0.37 + X_+} + \frac{0.37}{0.37 + X_-} \right) \tag{3.9}$$

where the definition of X_+, and X_- are the same as in equation (3.2).

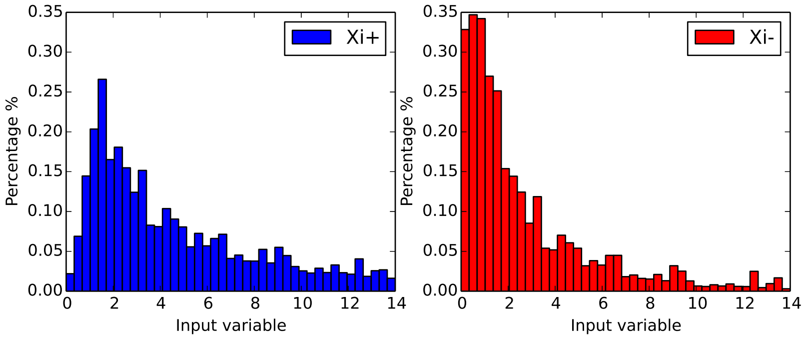

Figure 3.2: Distribution of X *in two European cities.* X_{i+} *and* X_{i-} *are explained in Eq.(3.2). The X values shown in this figure follow a 2.5 D approach to noise mapping considering the typical vertical cross sections that occur during this process.*

Since strict but complicated formulas of single-wedge and double-edge diffraction have been given in Pierce's work, the simplified equations proposed in this work will be compared with Pierce's theoretical solution. Figure (3.4) shows the amplitude difference, $10\log_{10}\left|\frac{p_{dif}}{p_{at,L}}\right|^2 = 10\log_{10}\left(\frac{1}{2}\left\{[g(X_+ + g(X_-))]^2 + [f(X_+ + f(X_-))]^2\right\}\right)$, between the diffracted case and free field propagation. The simplified method properly follows the Pierce's solution. The ratio between wave lengths and the geometrical dimension of urban buildings may differ in the order of 1 to 100. Therefore, in figure (3.4) three groups with different wave lengths are compared.

By using Eq.(3.7) and (3.8), the calculation time is reduced considerably. Figure (3.5) shows the ratio in CPU evaluation time between Pierce's method and the simplified method in case of a single-wedge and double-edged rigid barrier (see in section 3.2.2). CPU time ratios exceeding 10000 should be convincing.

3.2.2 Diffraction function of a double-edge rigid barrier

A double-edge diffraction as shown in figure (3.1 (b)) can be expressed as a single diffracted wave produced from edge 1 and then subsequently diffracted by edge 2 to reach the receiver. More details could be found in [5][18]. Then the corresponding angle of θ and θ_0 diffracted by the path $S \to 1 \to 2$ are 0 and $\beta_S - \theta_S$ respectively. Accordingly, $X_{S+} = \gamma M_\nu(\theta + \theta_0) = \gamma M_\nu(\beta_S - \theta_S)$ and $X_{S-} = \gamma M_\nu(\theta - \theta_0) = \gamma M_\nu(\theta_S - \beta_S)$. Instead of Γ, $\gamma = \sqrt{2r_S(W + r_r)/[\lambda(r_S + W + r_r)]}$ is used to calculate X in the double-edge diffraction case and M_ν is the same as in the single rigid-wedge case. Note that $M_\nu(\theta) \propto \cos\nu\theta$ leading to $X_{s+} = X_{S-}$. For

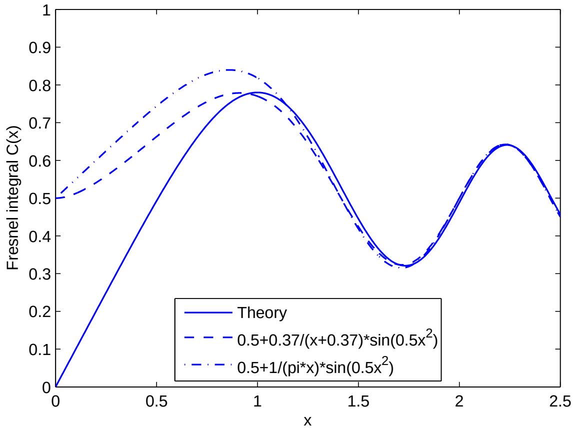

(a) C(x)

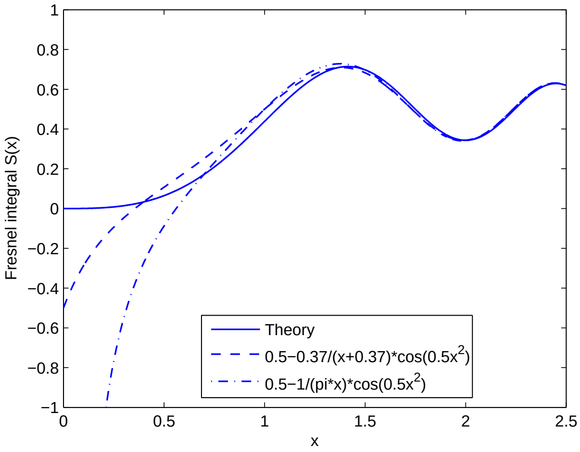

(b) S(x)

Figure 3.3: Comparison of the approximation accuracy of Fresnel Integral $C(x)$ *and* $S(x)$*.*

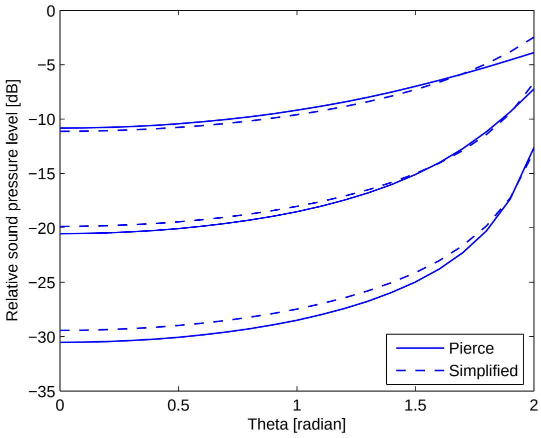

(a) Single diffraction

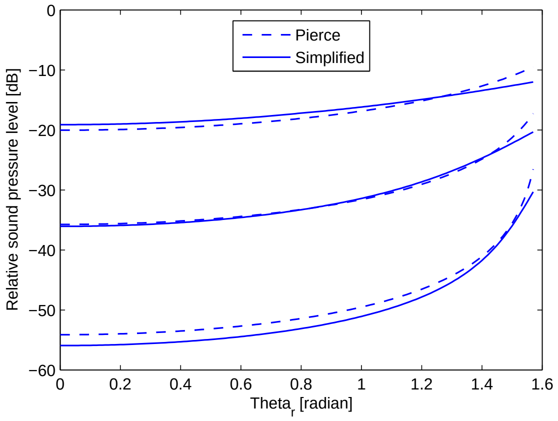

(b) Double diffraction

Figure 3.4: Validation of a single (a) and double (b) diffraction cases. In the legend, "Pierce" is the method presented by Pierce; "Simplified" is the set of equations introduced in this chapter. For single wedge diffraction: $r_s = r_r = 1\lambda, 10\lambda$ *and* 100λ *up to down respectively,* $\beta = 11/6\pi$, $\theta_s = \pi/6$, θ *ranges from 0 to* $5\pi/6$. *For double diffraction,* $r_s = r_r = W = 1\lambda, 10\lambda$ *and* 100λ *up to down respectively,* $\beta_s = \beta_r = 1.5\pi$, $\theta_s = \pi/4$, θ_r *ranges from 0 to* $\pi/2$.

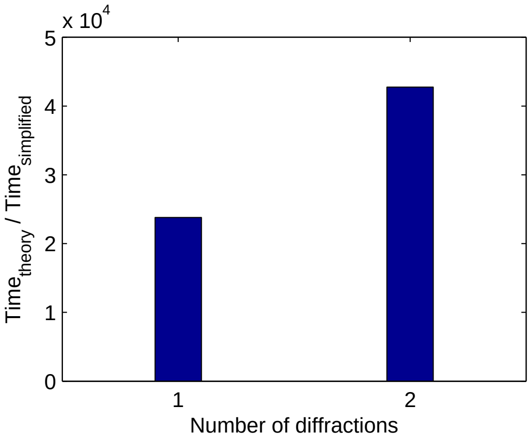

Figure 3.5: Comparison of calculation efficiency between Pierce's solution (labelled by "theory") and the simplified method presented in this work. The results are based on running the algorithms 10000 times. The algorithm used for calculating the Fresnel Integral is based on [19], using 12 terms in the Taylor series expansion.

the second part of the double-edge diffraction: path $1 \to 2 \to R$, $X_{R+} = X_{R-}$. Based on the above analysis, the diffraction function of a double connected edge then reads:

$$\begin{aligned} D &= D_1(r_{s,1}, \theta_{s,1}, r_{r,1}, \theta_{r,1}, \beta_1) D_2(r_{s,2}, \theta_{s,2}, r_{r,2}, \theta_{r,2}, \beta_2) \\ &= \frac{1}{2}\frac{e^{i\pi/4}}{\sqrt{2}}\left[f(BX_{S+}) + f(BX_{S-})\right]\frac{e^{i\pi/4}}{\sqrt{2}}\left[f(X_{R+}) + f(X_{R-})\right] \\ &= i\left(\frac{0.37}{0.37 + BX_{S+}} + \frac{0.37}{0.37 + BX_{S-}}\right)\left(\frac{0.37}{0.37 + X_{R+}} + \frac{0.37}{0.37 + X_{R-}}\right) \end{aligned} \tag{3.10}$$

As shown in figure (3.2), in a double-edge diffraction $r_{s,1} = r_s$, $\theta_{s,1} = \beta_S - \theta_s$, $r_{r,1} = W$, $\theta_{r,1} = 0$, $r_{s,2} = r_s + W$, $\theta_{s,2} = \beta_R$, $r_{r,2} = r_r$ and $\theta_{r,2} = \theta_r$. In this case, $\beta_1 = \beta_2 = 1.5\pi$. The factor 1/2 is used to remove the mirror image on the connecting surface. Because of $X_{S+} = X_{S-}$ and $X_{R+} = X_{R-}$,

$$D = i[f(BX_{S+})f(X_{R+})] = i\left(\frac{0.37}{0.37 + BX_{S+}}\frac{0.37}{0.37 + X_{R+}}\right) \tag{3.11}$$

where $B = \sqrt{WL/[(W + r_S)(W + r_r)]}$ is a character of the barrier width multiplied to the smaller one of X_{S+} and X_{R+} [3] [5]. If B is multiplied to the source term X_S, it indicates the sound propagating from the source to the receiver, whilst

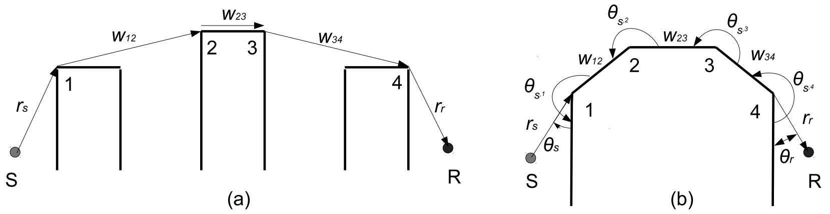

Figure 3.6: Schematic diagram of multiple diffraction.

B is multiplied to the receiver term X_R, it indicates the sound propagating from the receiver to the source. B actually makes the reciprocity principle do not hold in double or multiple diffraction situation. In Eq. 3.11, $X_{S+} < X_{R+}$ is assumed. This assumption is qualified in most urban geometrical conditions. Details can be found in [15].

Figure (3.4(b)) compares double-edge diffraction as predicted by Pierce and the simplified method as calculated by equation (3.11) with the parameters $r_s = 10\lambda$, $r_r = 10\lambda$, $W = 10\lambda$, $\theta_s = \pi/4$, $\beta_s = 3/2\pi$, $\beta_r = 3/2\pi$; θ_r increases from 0 to $\pi/2$. Except for predictions along the extension line of the barrier top, the simplified results match Pierce's solutions quite well for the chosen parameter set.

3.2.3 Generalization to multiple diffraction

Generalization to multiple diffraction is essential in urban cases where sound typically propagates over subsequent buildings.

In Kawai's [5] and Chu's [18] generalization, the double diffraction can be expressed by the product of two single diffraction where the incident wave for the second diffraction comes from the first diffraction edge. Similarly, multiple diffraction can be considered as a series of successive diffraction [18] as. The $(n-1)^{th}$ diffracted sound pressure by path $S1\cdots n$ is:

$$p_{n-1}^{S1\cdots n} = p_{n-2}^{S1\cdots n-1}\frac{L_{n-2}}{L_{n-1}}D_{n-1}e^{ik(L_{n-1}-L_{n-2})} \tag{3.12}$$

where D_n is the diffraction function at the in^{th} edge; L_n is the total diffraction path length. In the figure (3.6) case, $L_1 = r_s + W_{12}$, $L_2 = r_s + W_{12} + W_{23}$. Other path lengths are similar.

According to equation (3.12), $p_{n-2}^{S1\cdots n-1} = p_{n-3}^{S1\cdots n-2}\frac{L_{n-3}}{L_{n-2}}D_{n-2}e^{ik(L_{n-2}-L_{n-3})}$. Therefore, equation (3.12) becomes:

$$\begin{aligned} p_{n-1}^{S1\cdots n} &= p_{n-3}^{S1\cdots n-2}\frac{L_{n-3}}{L_{n-2}}D_{n-2}e^{ik(L_{n-2}-L_{n-3})}\frac{L_{n-2}}{L_{n-1}}D_{n-1}e^{ik(L_{n-1}-L_{n-2})} \\ &= p_{n-3}^{S1\cdots n-2}\frac{L_{n-3}}{L_{n-1}}D_{n-2}D_{n-1}e^{ik(L_{n-1}-L_{n-3})} \end{aligned} \tag{3.13}$$

If the diffracted sound pressure is recursively replaced by equation (3.12), $p_{n-1}^{S1\cdots n}$ becomes:

$$p_{n-1}^{S1\cdots n} = p_1^{S12}\frac{L_1}{L_{n-1}}D_2...D_{n-1}e^{ik(L_{n-1}-L_1)} \tag{3.14}$$

Substituting equation (3.1) to the above, form for the sound pressure at the n^{th} diffraction point or a receiver point after n-1 diffraction then reads:

$$p_{n-1}^{S1\cdots n} = \left(\frac{1}{2}\right)^C S_0\frac{e^{ikL_{n-1}}}{L_{n-1}}\prod_{l=1}^{n-1}D_l \qquad n = 2,3,\cdots \tag{3.15}$$

Equation (3.15), the same as Kim's [6], is the generalized form of multiple diffraction function which equals the product of the divergence of the source and its diffraction function, where the diffraction function D_l is:

$$\begin{aligned} D_l(r_{s,l},\theta_{s,l},r_{r,l},\theta_{r,l},\beta_l) &= \frac{e^{i\pi/4}}{\sqrt{2}}[f(B_lX_{l+}) + f(B_lX_{l-})] \\ = \quad \frac{e^{i\pi/4}}{\sqrt{2}}&\left(\frac{0.37}{0.37 + B_lX_{l+}} + \frac{0.37}{0.37 + B_lX_{l-}}\right) \end{aligned} \tag{3.16}$$

$X_{l+} = \gamma_l M_\nu(\theta_{l+})$. $X_{l-} = \gamma_l M_\nu(\theta_{l-})$. $\theta_{l+} = \theta_{s,l} + \theta_{r,l}$. $\theta_{r,l}$ is the angle from the right diffraction edge and the connecting line between the diffraction edge to the "receiver" and $\theta_{s,l}$ is the angle from the right diffraction edge to the connecting line between the diffraction point to the "source". For the definition of these angles, "source" and "receiver" can be the real source and receiver or can be the adjacent diffraction edges. $\theta_{l-} = \theta_{s,l} - \theta_{r,l}$. γ_l will be discussed later. n is the diffraction number. C is the number of adjacent double diffraction edges. In series of non-connected building blocks, C equals 1 as the diffraction path $S \to 1 \to 2 \to 3 \to 4 \to$ in figure (3.6(a)). As shown in figure (3.6 (a)), the sound pressure at receiver R consist of contributions from different propagation paths. The shortest path with least diffraction, $S \to 1 \to 2 \to 3 \to 4 \to R$, will dominate the sound pressures. In this study, only the shortest path is discussed, which implies $C = 1$ in most conditions. A typical case when C is greater than 1 is a single many-edged building, as shown in Figure (3.6(b)).

For multiple-diffraction, $B(r_s,r_r,W) = \sqrt{W(r_s + r_r + W)/[(W + r_s)(W + r_r)]}$ [5] is generalized to:

$$\begin{aligned}
B_1 &= B(r_s, W_{23} + W_{34} + \cdots + W_{n-1,n} + r_r, W_{12}) \\
B_2 &= B(r_s + W_{12}, W_{34} + \cdots + W_{n-1,n} + r_r, W_{23}) \\
&\vdots \\
B_l &= B(r_s + W_{12} + \cdots + W_{l-1,l}, W_{l+1,l+2} + \cdots + W_{n-1,n} + r_r, W_{l,l+1}) \\
&\vdots \\
B_{n-1} &= B(r_s + W_{12} + W_{23} + W_{34} + \cdots + W_{n-2,n-1}, r_r, W_{n-1,n}) \\
B_n &= 1
\end{aligned}$$

which results in the closed form:

$$B_l = \sqrt{\frac{W_{l,l+1}(r_s + \sum\limits_{j=1}^{n-1} W_{j,j+1} + r_r)}{(r_s + \sum\limits_{j=1}^{l} W_{j,j+1})(r_r + \sum\limits_{j=l}^{n-1} W_{j,j+1})}} \tag{3.17}$$

$\gamma(r_s, r_r, L) = \sqrt{2r_s r_r/(\lambda L)}$ is generalized to :

$$\begin{aligned}
\gamma_1 &= \gamma(r_s, W_{12} + W_{23} + W_{34} + \cdots + W_{n-1,n} + r_r, L) \\
\gamma_2 &= \gamma(r_s + W_{12}, W_{23} + W_{34} + \cdots + W_{n-1,n} + r_r, L) \\
&\vdots \\
\gamma_l &= \gamma(r_s + W_{12} + W_{23} + \cdots + W_{l-1,l}, W_{l,l+1} + W_{n-1,n} + r_r, L) \\
&\vdots \\
\gamma_n &= \gamma(r_s + W_{12} + W_{23} + W_{34} + \cdots + W_{n-1,n}, r_r, L)
\end{aligned}$$

or

$$\gamma_l = \sqrt{\frac{2\left(r_s + \sum_{j=1}^{l-1} W_{j,j+1}\right)\left(r_r + \sum_{j=l}^{n-1} W_{j,j+1}\right)}{\lambda\left(r_s + \sum_{j=1}^{n-1} W_{j,j+1} + r_r\right)}}$$

where r_s is the distance from the source to the first diffraction edge; $W_{l,l+1}$ is the distance between edge l and edge $l+1$; r_r is the distance from the receiver to the last diffraction edge. $M_\nu(\theta) = (\cos\nu\pi - \cos\nu\theta)/(\nu\sin\nu\pi)$ is generalized to

$$M_{\nu l}(\theta_l) = (\cos\nu_l\pi - \cos\nu_l\theta_l)/(\nu_l\sin\nu_l\pi), \tag{3.18}$$

When $n = 3$, Eq. (3.15) models a double-edge diffraction. Since $X_{l+} = X_{l-}$ in this special case, $\prod D = i\left(\frac{0.37}{0.37 + B_1X_{1+}}\frac{0.37}{0.37 + B_2X_{2+}}\right)$, where

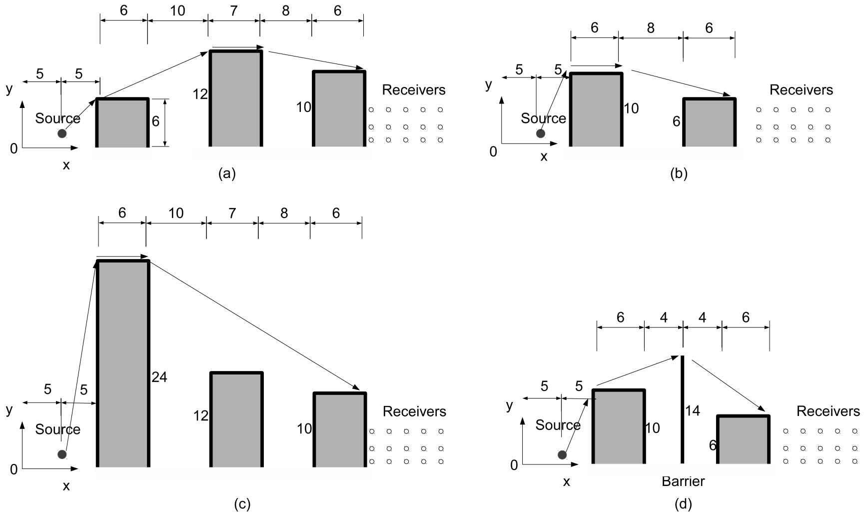

Figure 3.7: Geometries considered to validate multiple diffraction in absence of a source and receiver canyon.

$B_1 = \sqrt{WL/[(W + r_S)(W + r_r)]}$, $B_2 = 1$. B_1 will be multiplied to the smaller one of X_{1+} and X_{2+}. Here $X_{1+} < X_{2+}$ is assumed.

3.2.4 Validation of the multiple-edge simplified diffraction model

The proposed model is validated for the case of sound propagation over successive buildings, involving multiple edge diffraction. Various cases are presented in Figure (3.7), including a high rectangular building in between two lower ones near the source and receiver, a high building directly near the source followed by lower buildings towards the receivers, and a high thin barrier in between two buildings. The last case is not very common in a city, however, it can be used as a good validation case to include a single diffraction as well. Contour plots of the difference between the simplified method and the diffraction formula by Pierce are depicted in figure (3.8) to (3.11), for 250 Hz and 2000 Hz. In these calculations, the shortest propagation path and only diffraction over the roofs were considered. Note that multiple reflections in between the façades are not considered in neither of these models.

At most receiver positions in the shadow zone of the building furthest away from the source, the predicted values by the simplified method are close to the theoretical values. However, a clear zone with overestimations along the (virtual) extension line of the diffraction boundary is observed. The simplified method can thus be used to predict sound propagation diffracted by multiple edges within 2

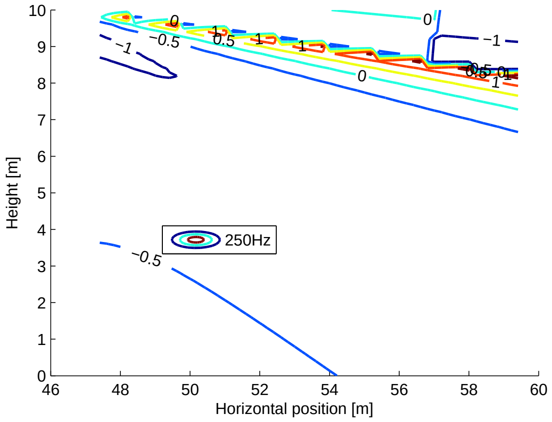

(a) 250 Hz

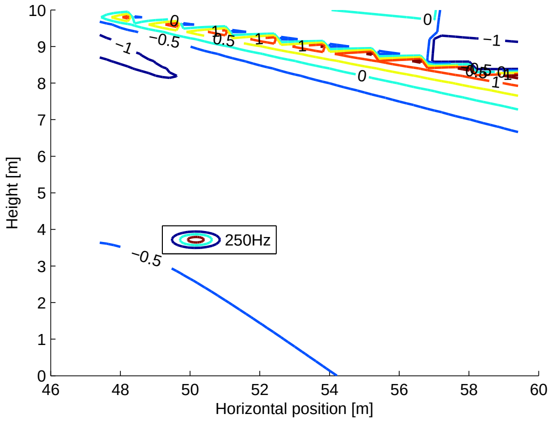

(b) 2000 Hz

Figure 3.8: Contour plots showing the sound pressure level difference between the presented method and Pierce's method ($L_{simplified} - L_{Pierce}$) in the receiver zone as defined in Fig. 3.7, for geometrical configuration (a). Calculations were performed for 250 Hz and 2000 Hz.

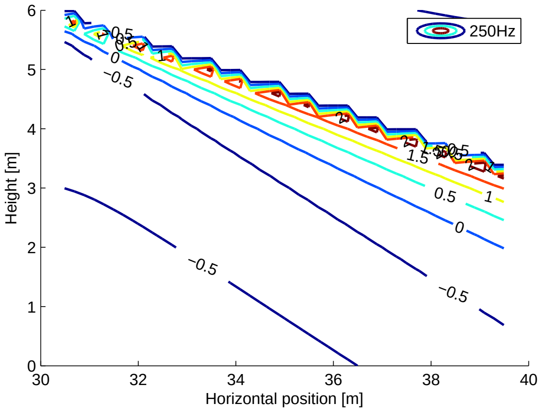

(a) 250 Hz

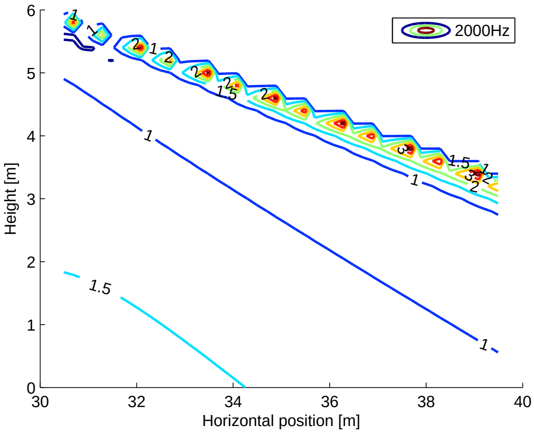

(b) 2000 Hz

Figure 3.9: Contour plots showing the sound pressure level difference ($L_{simplified} - L_{Pierce}$) in the receiver zone as defined in Fig. 3.7, for configuration (b).

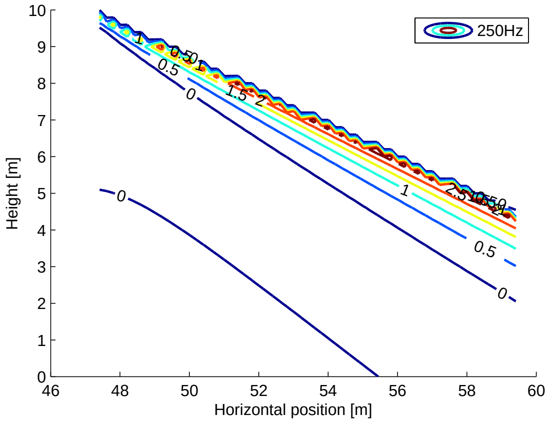

(a) 250 Hz

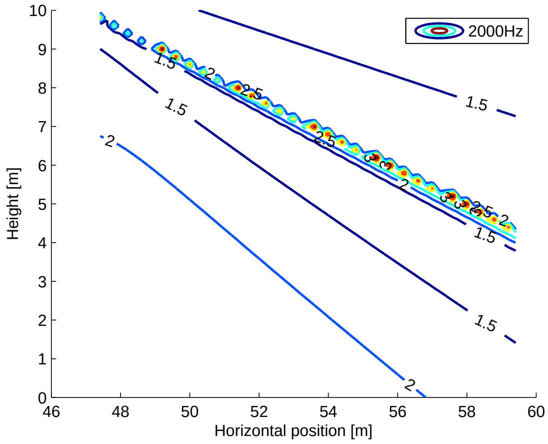

(b) 2000 Hz

Figure 3.10: Contour plots showing the sound pressure level difference ($L_{simplified} - L_{Pierce}$) in the receiver zone as defined in Fig. 3.7, for configuration (c).

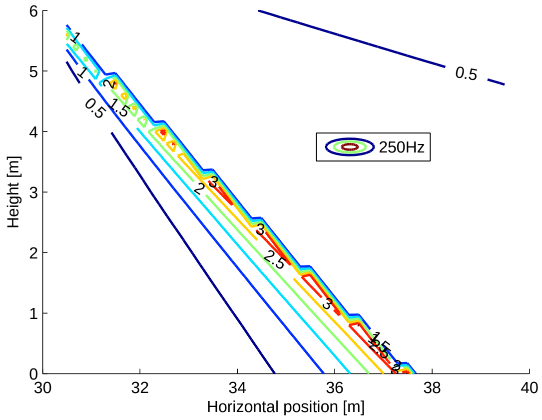

(a) 250 Hz

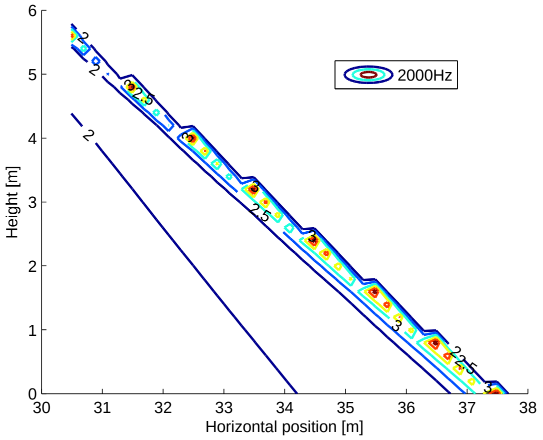

(b) 2000 Hz

Figure 3.11: Contour plots showing the sound pressure level difference $(L_{simplified} - L_{Pierce})$ *in the receiver zone as defined in Fig. 3.7, for configuration (d).*

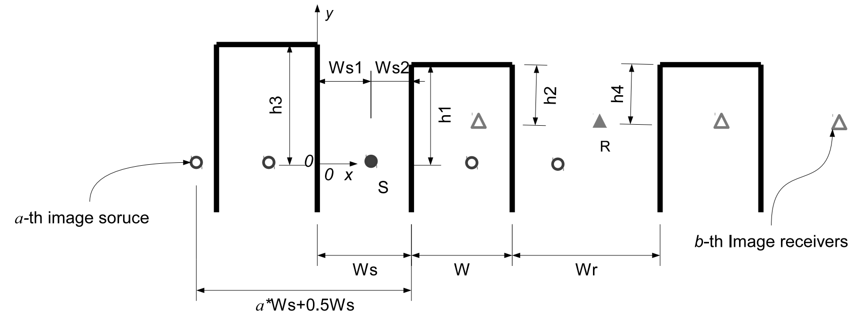

Figure 3.12: Demonstration of image sources and image receivers. Reflections from ground are not considered here. Circles are image sources and triangles are image receivers.

dB at strongly shielded areas. Near the extension line of the diffraction edge, an overestimation of 3 dB is obtained. Note that predicting diffraction in this specific zone is a complicated topic and contradictory to the goal of this work which is rather to simplify models. More theoretical solutions to tackle this problem can be found e.g. in [1, 3].

3.3 Contribution of reflections

When sources and receivers are located in so-called "city canyons", multiple reflections in both the source and receiver canyon become relevant. The latter is typically solved by considering image (mirror) sources and image receivers [20, 21, 22]. The position of the image sources and receivers is easily obtained by geometrical analysis of the problem under study.

In Figure (3.12), the circles and triangles are image sources and image receivers, respectively. Ground reflections are not considered here. The distance from the image source to the façade increases with the order of reflection. The first image source is at W_{s1} from the left façade of the source canyon. The second image source towards the left side is located at $W_{s2} + W_s$; the third one at $W_{s1} + 2W_s$. When generalizing, this yields :

$$d_a = \begin{cases} W_{s1} + (a-1)W_s & a = 1,3,5\cdots \\ W_{s2} + (a-1)W_s & a = 2,4,6\cdots \end{cases}$$

For simplicity, suppose the source is in the center of the canyon, so $W_{s1} = W_{s2}$. Consequently, the distance from the image source to the façade is then $a\ W_s - 0.5W_s$, where a is the ath image source.

Considering an insufficient number of mirror sources will strongly underestimate levels, a series of comparisons is carried out. Calculations show that including 50 image source, relative to only considering two, may add at least 4 dB, strongly depending on the assumed reflection coefficient of the façades in the source canyon as shown in Figure (3.13(a)). Similar estimates can be found in [23, 24]. In Figure (3.13(a)), a fixed configuration is used and only the reflection coefficients of the façades are varied. Figure (3.13(b)) shows the effect of the source canyon width and right-façade building height of the source canyon for a reflection coefficient of 0.97. The underestimation in sound pressure level by only considering the 1^{st} image source ranges from 5 dB to 13 dB.

Increasing the number of image sources increases the computing time considerably. As a result, only one or two image sources are typically considered in urban noise mapping. However, the simplified form as shown in Eq.(3.9) , Eq.(3.11) and Eq.(3.16) gives opportunities to cumulate the contribution of all the image sources as will be discussed in next sections.

3.3.1 Reflections between parallel buildings of equal façade heights

The analysis in this section is based on two assumptions. Firstly, it is assumed that the façades are flat, parallel and of equal height. Secondly, only image sources towards the left are considered. As illustrated in Figure (3.12), image sources and image receivers extend to both the left and right side from the real source or real receiver. However, the image sources going further to the "right" need to be diffracted 3 times to reach the receiver and consequently such contributions are much smaller than those going to the left. According to our calculations, the image sources going to the "left" direction contribute much more than the equivalent image sources going to the "right" direction. When the height of the façades is the same, the contribution of the image sources going to the "right" direction, and similarly, the image receivers going to the "left" direction, can be ignored.

The total contribution is expressed in Eq. (3.19) if the "left" image source and the "right" image receivers are marked by l and j:

$$\sum_{a=0}^{\infty}\sum_{b=0}^{\infty}|p_{a,b}|^2 = |p_{0,0}|^2 + \sum_{a=1}^{\infty}|p_{a,0}|^2 + \sum_{b=1}^{\infty}|p_{0,b}|^2 + \sum_{a=1}^{\infty}\sum_{b=1}^{\infty}|p_{a,b}|^2 \tag{3.19}$$

where, the subscripts indicates the position of the source, the receiver and the image sources and image receivers, $a = 0$ indicates the original source position and $b = 0$ indicates the original receiver position; the $a = 1, 2, 3\cdots$ indicates different image sources; similarly, $b = 1, 2, 3\cdots$ indicates different image receivers. $|p_{0,0}|^2$ is the contribution from the pure diffraction path, so involving no reflections. $|p_{a,0}|^2$ is the contribution from the a^{th} image source to the receiver. $|p_{0,b}|^2$ is the contribution from the source to the b^{th} image receiver. $|p_{a,b}|^2$ is the contribution from the a^{th} image source to the b^{th} image receiver.

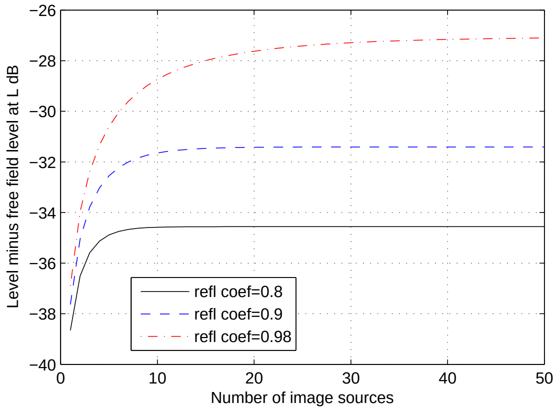

(a)

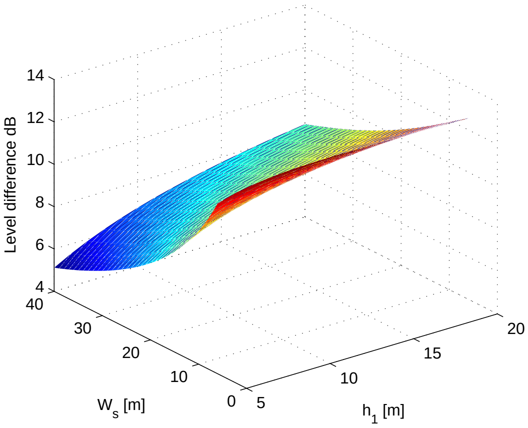

(b)

Figure 3.13: Effect of reflections without ground effect. The geometries are shown in figure (3.14). In (a), $W_s = 22$ *m;* $h_1 = 10$ *m;* $r_r = 7$ *m;* $W_i = 22$ *m;* $\beta_s = \beta_r = 1.5\pi$*; wave length=* 0.68*(500 Hz);source is in the middle of the canyon;. In (b),* r_r*,* W_i*,* β_s*,* β_r *are the same as (a), but the* W_s *and* h_1 *varies in a urban setting range and the reflection coefficient is fixed as 0.97. Level difference is the increase between 50 image sources and one image source.*

With these aforementioned assumptions, the level referenced to free field sound propagation from image source a to the receiver position via the shortest path L_a can be expressed as:

$$\left|\frac{p_{a,0}}{p_{at,L_a}}\right|^2 = \left(\frac{0.37}{X_{a,1}+0.37}\right)^2 \left(\frac{0.37}{X_{a,2}+0.37}\right)^2 \tag{3.20}$$

where $X_{a,1}$ and $X_{a,2}$ indicate the input from a source and a receiver. When $a > 0$, the sources are imagined, therefore, “1” and “2” are used to indicate “S” and “R” in equation (3.11). For most environmental sounds, the coherence length of the sound is rather short. Moreover fast temporal changes in propagation conditions may further destroy coherence. Therefore, the phase effect is neglected in Eq. (3.20) and only the sound power is considered.

For a point source, the sound pressure at distance L_a is $p_{at,L_a} = \dfrac{\rho_s^a S_0}{L_a} e^{-jkL_a}$. $|p_{a,0}|^2$ is rewritten as:

$$|p_{a,0}|^2 = \left(\frac{0.37}{X_{a,1}+0.37}\right)^2 \left(\frac{0.37}{X_{a,2}+0.37}\right)^2 \left(\frac{\rho_s S_0}{L_a}\right)^2 \tag{3.21}$$

where ρ_s is the reflection coefficient of the façade. For the 1^{st} image source, the amplitude decreases to $\rho_s S_0$ and for the a^{th} image source, the amplitude decreases to $\rho_s^a S_0$. For diffraction over buildings, the diffraction edge is often around 1.5π. In these cases, $M_\nu(\beta_s - \theta_s) = \dfrac{\cos\nu\pi - \cos(\beta_s - \theta_s)}{\nu\sin\nu\pi} \approx \dfrac{\sqrt{3}}{2}\cos\theta_s$ by using the approximation $\cos\frac{2\theta_s}{3} - 0.5 \approx 0.5\cos\theta_s$. The total sum can be written as:

$$|p_{a,0}|^2 = (\rho_s^a S_0)^2 \left[\frac{0.37}{\sqrt{\frac{2r_{a,s}W}{\lambda(W+r_{a,s})}}\frac{\sqrt{3}}{2}\cos(\theta_{a,s})L_a + 0.37L_a}\right]^2 \left(\frac{0.37}{X_{a,2}+0.37}\right)^2 \tag{3.22}$$

When $W+r_{a,s} \gg r_r$, $\left(\dfrac{0.37}{X_{a,2}+0.37}\right)^2 = \left(\dfrac{0.37}{\sqrt{\frac{2r_r(W+r_{a,s})}{\lambda(r_{a,s}+W+r_r)}}\sqrt{3}(\cos\frac{2}{3}\theta_r - 0.5) + 0.37}\right)^2$ can be approximated as $\left(\frac{0.37}{\sqrt{\frac{2r_r}{\lambda}}\sqrt{3}(\cos\frac{2}{3}\theta_r - 0.5)+0.37}\right)^2$ and becomes independent of the order of the image source and will be called C_{1s}. Suppose $r_{a,s} >> W$, equation (3.22) then becomes:

$$|p_{a,0}|^2 \approx (\rho_s^a S_0)^2 C_{1s} \left(\frac{1}{3.31\sqrt{\frac{W}{\lambda}}h_1 + r_{a,s} + W + r_r}\right)^2$$

h_1 is the distance from the source to the top of the building. When $r_{a,s}$ is far greater than H_m, $L_a \approx d_a + W_s + W + r_r = a\ W_s + 0.5W_s + W + r_r$. The sum over all image sources can be rewritten in a closed form using Hurwitz-Lerch transcendent:

$$\sum_{a=1}^{\infty} |p_{a,0}|^2 = C_{1s}\,(S_0)^2\,\frac{\rho_s^2}{W_s^2}\Phi\left(\rho_s^2 2, \frac{C_{3s} + W_s}{W_s}\right) \tag{3.23}$$

where, $C_{3s} = 0.5W_s + W + r_r + 3.31\sqrt{\frac{W}{\lambda}h_1}$; W_s is the width of the source canyon. The details can be found in [15].
Similarly ,

$$\sum_{b=1}^{\infty} |p_{0,b}|^2 = C_{1r}\,(S_0)^2\,\frac{\rho_r^2}{W_r^2}\Phi\left(\rho_r^2 2, \frac{C_{3r} + W_r}{W_r}\right)$$

where, $C_{1r} = \left(\frac{0.37}{\sqrt{\frac{2r_s}{\lambda}}\sqrt{3}(\cos\frac{2}{3}\theta_s - 0.5)}\right)^2$, $C_{3r} = 0.5W_r + W + r_s + 3.31\sqrt{\frac{W}{\lambda}h_2}$.
h_2 is the distance from the receiver to the top of the building, ρ_r is the reflection coefficient of the receiver canyon. W_r is the width of the receiver canyon.
The $\sum_{b=1}^{\infty}\sum_{a=1}^{\infty}|p_{a,b}|^2$ part is difficult to write in a condensed form, an approximation is given as:

$$\sum_{b=1}^{\infty}\sum_{a=1}^{\infty}|p_{a,b}|^2 \approx \frac{(1.59)^2(\rho_s\rho_r)^6}{\left(\frac{3.31h_1}{\sqrt{\lambda} + 1.5W_s + W + 1.5W_r}\right)\left(\frac{3.31h_3}{\sqrt{\lambda} + 1.5W_s + W + 1.5W_r}\right)}$$

The details could be found in [15].
To validate the aforementioned approaches and simplifications, a comparison is made with full wave FDTD calculations [25, 26], taking $W_s = 20$, $h_1 = 11$, $W = 10$, $h_3 = 11$, $\beta_s = \beta_r = 1.5\pi$, $\theta_s = 0.25\pi$, $H_r = 0$. Ground reflections are not considered and the source is positioned in the middle of the source canyon. The configuration studied is summarized in in Figure (3.14).
Figure (3.15) shows the difference between FDTD simulation and the results calculated using Eq.(3.23). Since the FDTD simulations are in 2D, in order to limit the computational burden, the simulated time signal is multiplied by $\frac{1}{\sqrt{ct}}$ to transfer the response of a coherent line source to the one of a point source as proposed in [27]. The results of four individual frequencies are listed. The overestimation around the extension line of the roof top is also caused by the diffraction model as mentioned in the previous sections. The errors of the other receiver positions can be considered as the uncertainties caused by the reflection model and diffraction.

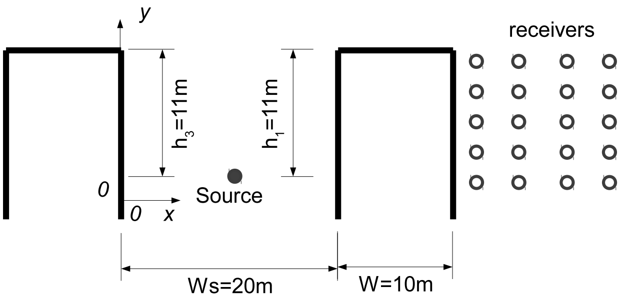

Figure 3.14: Geometry considered to evaluate the simplified strategy to include multiple reflections in between opposing parallel building façades.

3.3.2 Generalize the reflections combined with multiple diffraction

In the previous section, the reflections between two parallel buildings were discussed. The combination of reflections and multiple diffraction will be discussed in this section.

3.3.2.1 Façades with equal height: $h_1 = h_3$

According to Eq.(3.15), the squared sound pressure after $n-1$ diffraction over the squared sound pressure in free field can be written as:

$$\left|\frac{p_{n-1}^{S1\cdots n}}{p_{at,L}}\right|^2 = \left(\frac{1}{2}\right)^{2C} \prod_{l=1}^{n-1} |D_l|^2 \quad n = 2, 3, \cdots \tag{3.24}$$

Substituting Eq.(3.16) and Eq.(3.18) into equation (3.24) and moving the first diffraction term out of the product, leads to:

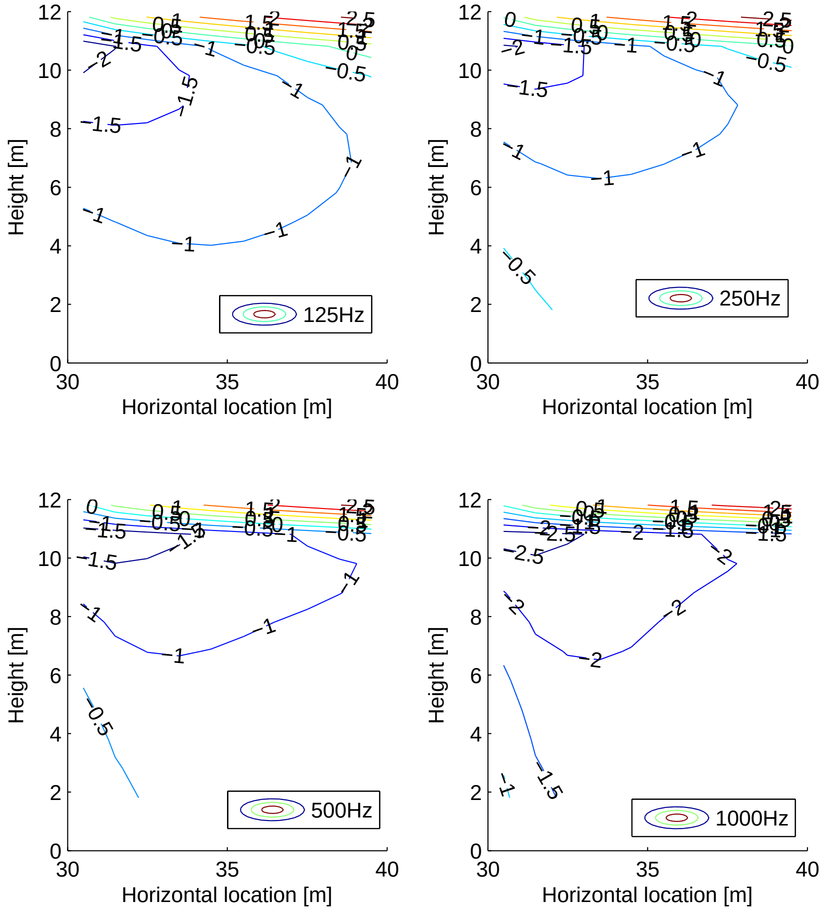

Figure 3.15: Contour plot of level difference between the simplified model (including multiple reflections and double diffraction) and FDTD simulation.

$$\begin{aligned}&\left|\frac{p_{a,0}}{p_{at,L_a}}\right|^2 = \\ &\left(\frac{1}{2}\right)^{2C}\Bigg(\frac{0.37}{0.37+\sqrt{\frac{2W_{12}r_{a,s}}{\lambda(W_{12}+r_{a,s})}}M_{\nu 1}(\theta_{1+})}+\frac{0.37}{0.37+\sqrt{\frac{2W_{12}r_{a,s}}{\lambda(W_{12}+r_{a,s})}}M_{\nu 1}(\theta_{1-})}\Bigg)^2 \\ &\prod_{l=2}^{n-1}\left(\frac{0.37}{0.37+\sqrt{\frac{2W_{l,l+1}(r_{a,s}+\sum_{j=1}^{l-1}W_{j,j+1})}{\lambda(r_{a,s}+\sum_{j=1}^{l}W_{j,j+1})}}M_{\nu l}(\theta_{l+})}\right. \\ + &\left.\frac{0.37}{0.37+\sqrt{\frac{2W_{l,l+1}(r_s+\sum_{j=1}^{l-1}W_{j,j+1})}{\lambda(r_s+\sum_{j=1}^{l}W_{j,j+1})}}M_{\nu l}(\theta_{l-})}\right)^2 \end{aligned} \tag{3.25}$$

If the first two diffraction edges are adjacent to each other, which means that sounds do not propagate over a thin barrier first , $M_{\nu 1}(\theta_{1+}) = M_{\nu 1}(\theta_{1-})$. For a rectangular building, the diffraction angle $\beta_{s,1}$ is 1.5π, $M_\nu(\beta_{s,1}-\theta_{s,1}) = \frac{\cos\nu\pi - \cos(\beta_{s,1}-\theta_{s,1})}{\nu\sin\nu\pi} \approx \frac{\sqrt{3}}{2}\cos\theta_{s,1}$. Also, if $r_s + \sum_{j=1}^{l-1} W_{j,j+1}$ is much greater than $W_{l,l+1}$, $\frac{r_{a,s}+\sum_{j=1}^{l}W_{j,j+1}-W_{l,l+1}}{(r_{a,s}+\sum_{j=1}^{l}W_{j,j+1})}$ approaches to 1. Eq.(3.25) can further reduced to:

$$\begin{aligned}\left|\frac{p_{a,0}}{p_{at,L_a}}\right|^2 \approx &\left(\frac{1}{2}\right)^{2C-2}\left(\frac{0.37}{0.37+\sqrt{\frac{2W_{12}r_{a,s}}{\lambda(W_{12}+r_{a,s})}\frac{\sqrt{3}}{2}\cos\theta_{s,1}}}\right)^2 \\ &\prod_{l=2}^{n-1}\left(\frac{0.37}{0.37+\sqrt{\frac{2W_{l,l+1}}{\lambda}}M_{\nu l}(\theta_{l+})}+\frac{0.37}{0.37+\sqrt{\frac{2W_{l,l+1}}{\lambda}}M_{\nu l}(\theta_{l-})}\right)^2\end{aligned}$$

Timing $|p_{at,L_a}| = \frac{S_0\rho_s^a}{L_a}$ on both sides of the above equation, the total contribution can be written in a generalized form as:

On the condition that the angle of the diffracting edge is 1.5π (rectangular building), the approximation used in Eq.(3.22) is still satisfied, the above equation becomes:

$$\sum_{a=1}^{\infty}|p_{a,0}|^2 =$$

$$C_{1,g}\sum_{a=1}^{\infty}\left[(S_0\rho_s^a)^2\Big(\frac{0.37}{0.37L_a+\sqrt{\frac{2W_{12}r_{a,s}}{\lambda(W_{12}+r_{a,s})}}\frac{\sqrt{3}}{2}\cos\theta_{s,1}L_a}\Big)^2\right]$$

$$= C_{1,g}\sum_{a=1}^{\infty}\left[(S_0\rho_s^a)^2\Big(\frac{1}{L_a+3.31h_1\sqrt{\frac{W_{12}}{\lambda}\frac{(r_{a,s}+\sum_{j=1}^{l-1}W_{j,j+1}+r_r)^2}{r_{a,s}(W_{12}+r_{a,s})}}}\Big)^2\right] \tag{3.26}$$

where,

$$C_{1,g}=\left(\frac{1}{2}\right)^{2C-2}\prod_{l=2}^{n-1}\left(\frac{0.37}{0.37+\sqrt{\frac{2W_{l,l+1}}{\lambda}}M_{\nu l}(\theta_{l+})}+\frac{0.37}{0.37+\sqrt{\frac{2W_{l,l+1}}{\lambda}}M_{\nu l}(\theta_{l-})}\right)^2 \tag{3.27}$$

Suppose $r_{a,s}$ is much greater than $\sum_{j=1}^{l-1}W_{j,j+1}+r_r$, $\sqrt{\frac{(r_{a,s}+\sum_{j=1}^{l-1}W_{j,j+1}+r_r)^2}{r_{a,s}(W_{12}+r_{a,s})}}$ can be approximated as 1. The uncertainties of this assumption will be validated later. With this assumption, equation (3.26) can be similarly calculated as before with the Hurwitz-Lerch transcendent:

$$\sum_{a=1}^{\infty}|p_{a,0}|^2 = C_{1,g}\,(S_0)^2\,\frac{\rho_s^2}{W_s^2}\Phi(\rho_s^2,2,\frac{C_{3,g}+W_s}{W_s}) \tag{3.28}$$

where,

$$C_{3,g}=3.31\sqrt{\frac{W_{12}}{\lambda}}h_1+0.5W_s+r_r+\sum_{j=1}^{n-1}W_{j,j+1}, \tag{3.29}$$

When $n=2$, $C_{1,g}=C_{1,s}$ and $C_{3,g}=C_{3,s}$.

The test case in Figure (3.16) is used to validate the generalized form for $h_1=h_3$. The predicted errors (see Figure (3.17)) are relative large compared to the previous validation cases. The possible reasons will be discussed in section 3.4.

3.3.2.2 Façades with different heights: $h_3 < h_1$

If $h_3 < h_1$, some of the image sources located away from the screening building cannot contribute any more to the total sound pressure level without an additional diffraction as shown by the dashed line in Figure (3.18(a)). Accordingly, the image

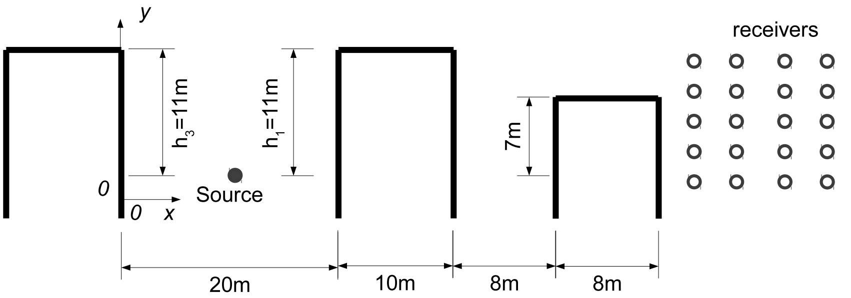

Figure 3.16: Geometry of a typical generalized case including reflections and multiple diffraction.

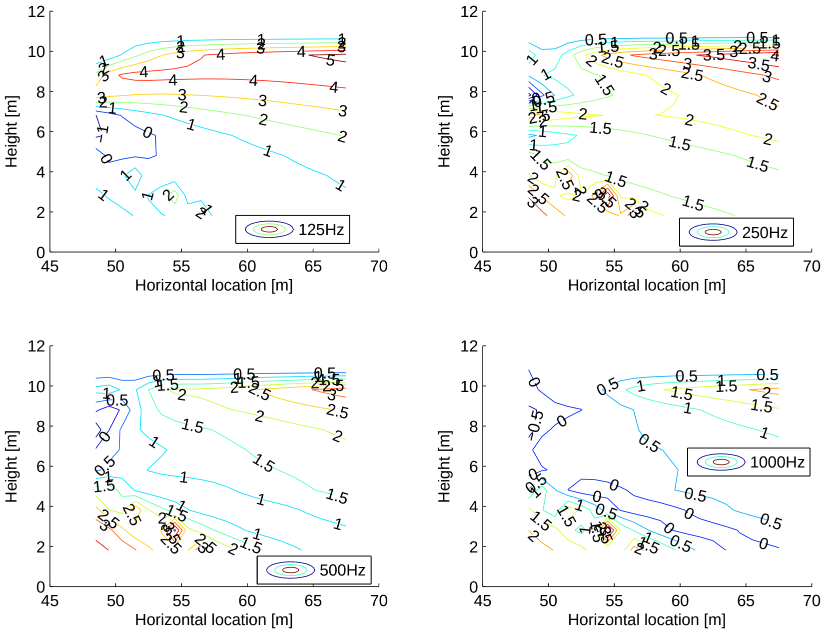

Figure 3.17: Contour plot of the level difference between the generalized model and the FDTD simulations for the geometry as in figure (3.16).

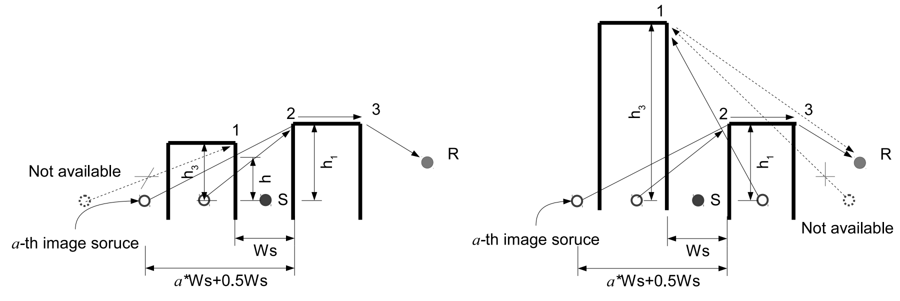

(a) (b)

Figure 3.18: Demonstration in case of $h_3 < h_1$ *or* $h_3 > h_1$

sources located in the direction of the central screening building become more relevant. Assuming that the source lies in the middle of the canyon W_s and according to the simple ratio $\frac{aW_s+0.5W_s}{h_1} = \frac{aW_s-0.5W_s}{h} = 1, 2, \cdots$, the relation between h and h_1 is: $h = \frac{a-0.5}{a+0.5}h_1$, where $h_1 = H_m-$source height. When $h = \frac{a-0.5}{a+0.5}h_1 > h_3$, the ath image source will become unavailable. Specifically, the relation actually is $h = 1/3h_1, 1/3h_1, 3/5h_1, 5/7h_1\cdots$.

Instead of $\sum_{a=1}^{\infty}|p_{a,0}|^2$, the total contribution becomes:

$$\begin{aligned}
&\sum_{a=1}^{N}|p_{a,0}|^2 + \sum_{a=N+1}^{\infty}|q_{a,0}|^2 = \sum_{a=1}^{\infty}|p_{a,0}|^2 - \sum_{a=N+1}^{\infty}|p_{a,0}|^2 + \sum_{a=N+1}^{\infty}|q_{a,0}|^2 \\
= \quad & C_{1,g,1}S_0^2\frac{\rho_s^2}{W_s^2}\Phi(\alpha^2, 2, 1 + \frac{C_{3,g,1}}{W_s}) - C_{1,g,1}S_0^2\frac{\rho_s^{2(N+1)}}{W_s^2}\Phi(\rho_s^2, 2, N+1+\frac{C_{3,g,1}}{W_s}) \\
+ \quad & C_{1,g,2}S_0^2\frac{\rho_s^{2(N+1)}}{W_s^2}\Phi(\rho_s^2, 2, N+1+\frac{C_{3,g,2}}{W_s}) \qquad (3.30)
\end{aligned}$$

Where $|p_{a,0}|^2$ and $|q_{a,0}|^2$ are sound pressure distinguished by different diffracted paths. N is the number from which the image source will have to diffract 3 times to reach the receiver, i.e. the diffraction path changes from $a^{th}\text{image} \rightarrow 2 \rightarrow 3 \rightarrow R$ to $a^{th}\text{image} \rightarrow 1 \rightarrow 2 \rightarrow 3 \rightarrow R$. $p_{a,0}$ is sound diffracted twice and $q_{a,0}$ is sound diffracted 3 times to reach the receiver position. $C_{1,g,x}$ and $C_{3,g,x}$ can be calculated by Eq.(3.27) and Eq.(3.29). The indexes "x" of $C_{1,g}$ and $C_{3,g}$ are used to distinguish different inputs in Eq.(3.27) and Eq.(3.29).

The configuration depicted in Figure (3.19) is used to validate Eq.(3.30). Figure (3.20) shows the comparison results. The errors at most receivers are less than 2 dB. Largest deviations from the full-wave reference calculations appear near the extension line of the building's roof.

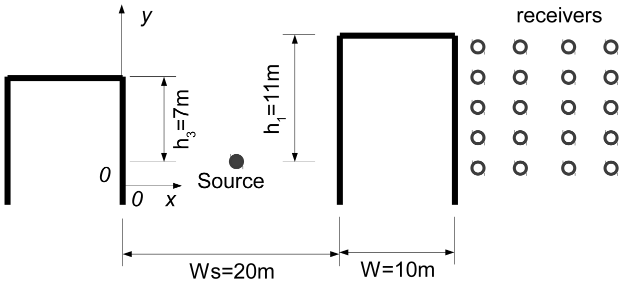

Figure 3.19: Geometry to check the generalized model with different façades heights: $h_3 < h_1$

3.3.2.3 Façades with different heights: $h_3 > h_1$

If $h_3 > h_1$, the contribution of the diffraction following some paths, such as "a^{th}image → 2 → 1 → 3 → R", "a^{th}image → 1 → 3 → R" and "a^{th}image → 1 → R" as shown in figure (3.18), may not be neglected. The recommended formula for a configuration where $h_3 > h_1$ is:

$$\begin{aligned}
&\sum_{a=1}^{\infty}|p_{a,0}|^2+\sum_{a=1}^{M}|q_{a,0}|^2+\sum_{a=M+1}^{N}|q'_{a,0}|^2+\sum_{a=1}^{\infty}|q''_{a,0}|^2\\
=\;& C_{1,g,3}S_0^2\frac{\rho_s^2}{W_s^2}\Phi(\rho_s^2,2,1+\frac{C_{3,g,3}}{W_s})+C_{1,g,4}S_0^2\frac{\rho_s^2}{W_s^2}\Phi(\rho_s^2,2,1+\frac{C_{3,g,4}}{W_s})\\
-\;& C_{1,g,4}S_0^2\frac{\rho_s^{2(M+1)}}{W_s^2}\Phi(\rho_s^2,2,M+1+\frac{C_{3,g,4}}{W_s})\\
+\;& C_{1,g,5}S_0^2\frac{\rho_s^{2(M+1)}}{W_s^2}\Phi(\rho_s^2,2,M+1+\frac{C_{3,g,5}}{W_s})\\
-\;& C_{1,g,5}S_0^2\frac{\rho_s^{2(N+1)}}{W_s^2}\Phi(\rho_s^2,2,N+1+\frac{C_{3,g,5}}{W_s})\\
+\;& C_{1,g,6}S_0^2\frac{\rho_s^2}{W_s^2}\Phi(\rho_s^2,2,1+\frac{C_{3,g,6}}{W_s}) \qquad (3.31)
\end{aligned}$$

Where $|p_{a,0}|^2, |q_{a,0}|^2, |q'_{a,0}|^2$ and $|q''_{a,0}|^2$ are used to distinguish sound pressure diffracted by different paths. $|p_{a,0}|^2$ is path a^{th}image → 2 → 3 → R, $|q_{a,0}|^2$, is path a^{th}image → 1 → R, $|q'_{a,0}|^2$ is path a^{th}image → 1 → 3 → R and $|q''_{a,0}|^2$ is path a^{th}image → 2 → 1 → 3 → R. $C_{1,g,x}$ and $C_{3,g,x}$ can be calculated from the generalized form Eq.(3.27) and Eq.(3.29). The indexes x of $C_{1,g,x}$ and $C_{3,g,x}$ is only used to distinguish different $C_{1,g}$ and $C_{3,g}$. M is the image source number from which the diffraction path changes from a^{th}image → 1 → R to

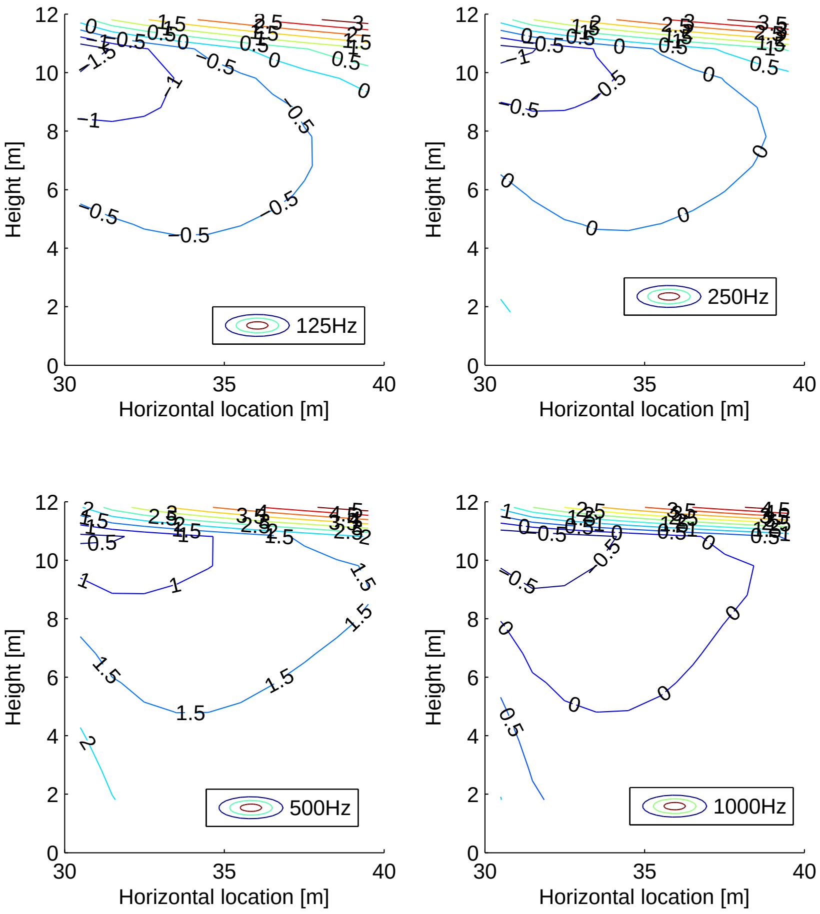

Figure 3.20: Contour plot of the level difference between the generalized model and the FDTD simulations for the geometry as in figure (3.19).

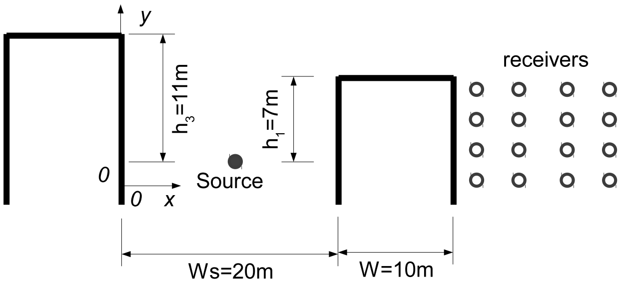

Figure 3.21: Geometry to check the generalized model with different façades heights: $H_s > H_m$

a^{th}image → 1 → 3 → R. N is the image source number from which the diffraction path changes from a^{th}image → 1 → 3 → R to a^{th}image → 2 → 1 → 3 → R. The test case as presented in Figure (3.21) and the results are shown in Figure (3.22)

Levels of most receivers coincide with the simulations well. Different with the conditions $h_1 = h_3$ and $h_3 < h_1$, the predicted levels are smaller than the full-wave simulations.

3.4 Discussion

By introducing several approximations urban sound propagation involving multiple reflections and diffraction is highly simplified and the calculation speed is improved by several orders of magnitude. The most important steps are the introduction of an approximation for the Fresnel Integral, the assumption that the effect of multiple diffraction can be approximated by including only the shortest path connection all rooftops, and finally by compacting the sum over all image sources caused by the source and receiver canyon reflections. The first approximation has been validated by comparison with a full analytical model, the other approximations have been validated by comparison to numerical FDTD simulations.

The error introduced by the approximation of the Fresnel Integral remains smaller than one dB except near the edge of the shadow region. The error introduced by approximating the Fresnel Integral in case of multiple diffraction behaves very similar. It should nevertheless be noted that this does not check the validity of taking into account the shortest path only.

Approximating the sum over multiple image sources allows to obtain a closed analytical form for the sum. Two approximations used to resolve the sum were not found in previous work. The first one allows to eliminate the image source location from all diffraction terms except from the first one. This requires that

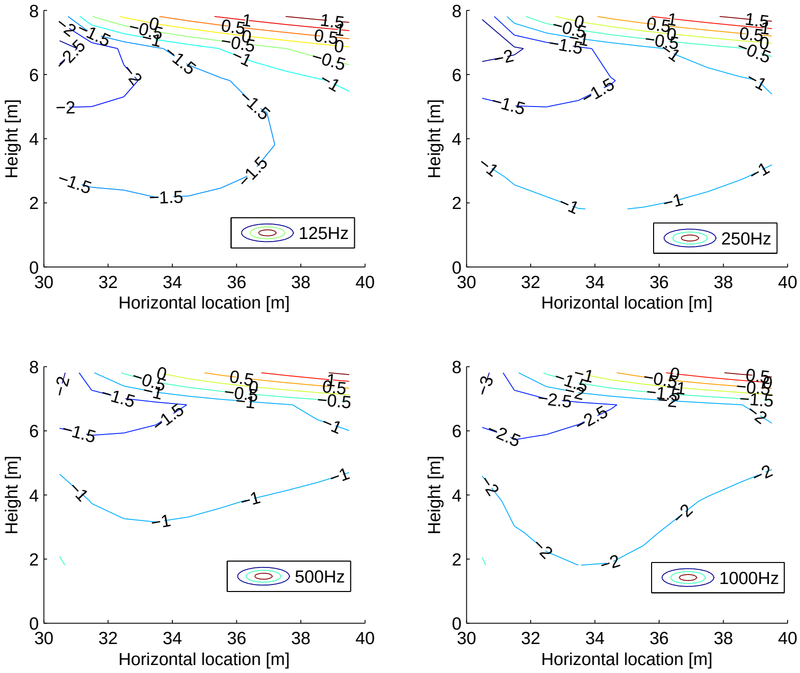

Figure 3.22: Contour plot of the level difference between the generalized model and the FDTD simulations for the geometry as in figure (3.21).

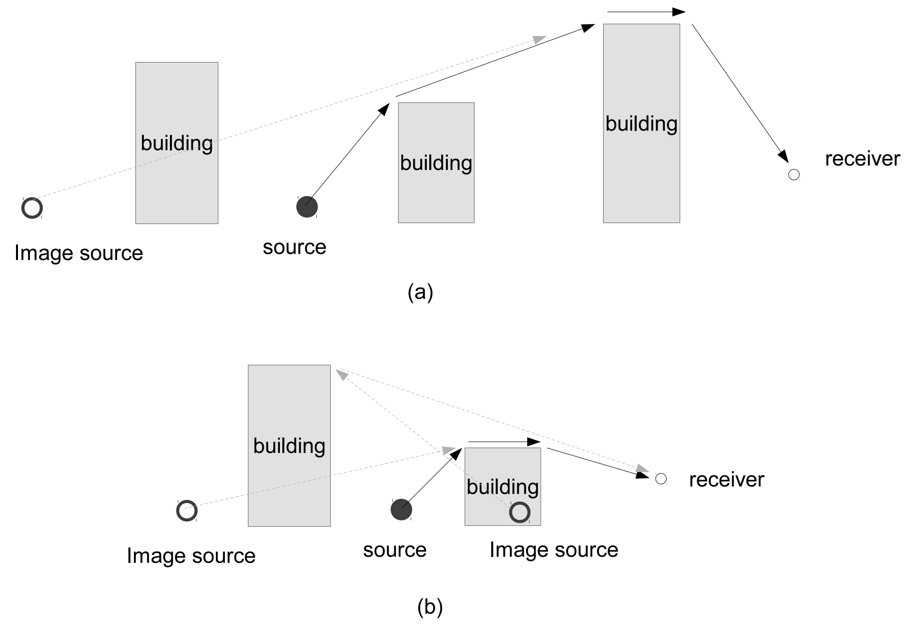

(a)

(b)

Figure 3.23: Special cases influencing the results.

$r_s + \sum_{j=1}^{l-1} W_{j,j+1}$ is much greater than $W_{l,l+1}$. The second assumption states that $r_{a,s} \gg \sum_j^{n-1} W_{j,j+1} + r_r$, which means that $\frac{r_{a,s}+\sum_{j=1}^{n-1} W_{j,j+1}+r_r}{r_{a,s}} \approx 1$. However, this condition maybe not satisfied for long-distance propagation in combination with a source located in a narrow canyon. If $\sum_j^{n-1} W_{j,j+1} + r_r < 500$m, the error caused by $\frac{r_{a,s}+\sum_{j=1}^{n-1} W_{j,j+1}+r_r}{r_{a,s}} \approx 1$ is less than 3 dB in an urban setting.

Moreover, if this distance is larger than 500 m, one will often encounter other noise sources in more closer distances. These sources will dominate the overall noise climate due to the geometrical divergence that is very large in case of long distance propagation. For shorter distances the impact of the approximation was explicitly tested by comparing levels calculated with the simplified analytical model to numerical simulations. This showed that in the deep shadow region errors are generally lower than 1 dB even in the case of multiple intermediate buildings.

In real urban situations, some particular cases may occur that are not explicitly covered by the formulations presented in this chapter. For example, in Figure (3.23(a)), the depicted image source reaches the receiver by interacting with different building edges than e.g. the (original) source. Another typical case is as shown in Figure (3.23(b)); the left building is higher than the right one and the receiver is far away. Some of the image sources could reach the receiver by a single diffraction only. Therefore, carefully analysing the contributions from the different image source is needed when using theoretical diffraction formulas.

While deriving the model an important assumption is that the source is located in the middle of the source canyon, which is representative for typical road traffic noise sources. These assumptions allowed simplifying the presented diffraction model. Deviations from these will lead to less accurate results. Ground reflections are not considered either. However, these can be easily incorporated by using an additional set of image sources located below the ground plane. Similar formulas as represented here can be used.

Compared to an explicit sum of the image sources, the Hurwitz-Lerch transcendent is more efficient if the number of image sources is greater than 3. Figure (3.24) shows a comparison curve. This curve shows the ratio of calculating time between the two methods. This comparison is based on reflections over a rectangular building of 10 m wide. Every data point in the y-axis is the average of 100 times running of the engineering models. Details are shown in the caption of the figure. From this figure, the calculating efficiency is similar among our presented model, ISO9613-2 model, CNOSSOS-EU model and the HARMONIOSE model. The NORD2000 model is slower than others.

Besides, the calculating efficiency, figure (3.25) shows the accuracy of diffracted sound over a thick barrier among our model and some commonly used engineering models. Our presented model, Pierce's model and NORD2000 have good prediction compared with the FDTD simulation. The ISO9613-2, CNOSSOS-EU and HARMONOISE model overestimate the sound pressure levels.

3.5 Conclusion

A simplified method to predict sound pressure levels at shielded areas in typical urban situations are presented and validated. This method is essentially based on Pierce diffraction theory, where the Fresnel Integral is approximated by a special pair of trigonometric functions tuning this approximation to typical situations encountered in urban sound propagation: tall barriers and a specific interest in the deep shadow zone. The new single, double and multiple diffraction functions are validated by theoretical solutions and full-wave simulations. Although the error that is introduced is limited to below 1 dB in most of the space of interest, the gain in calculation time is tremendous (several orders of magnitude). The chapter then focusses in particular on combining the effect of multiple reflections with multiple diffraction. Additional assumptions allow to make a significant part of the sum independent on the reflection order and independent of the infinite sum of the image sources. Thus the contribution of the image source can be relatively easily condensed with the Hurwitz-Lerch transcendent. Once the sum includes over 3 image sources, some additional calculation time is gained by this last step. Generally, the new method can predict sound pressure levels at shielded areas within 2

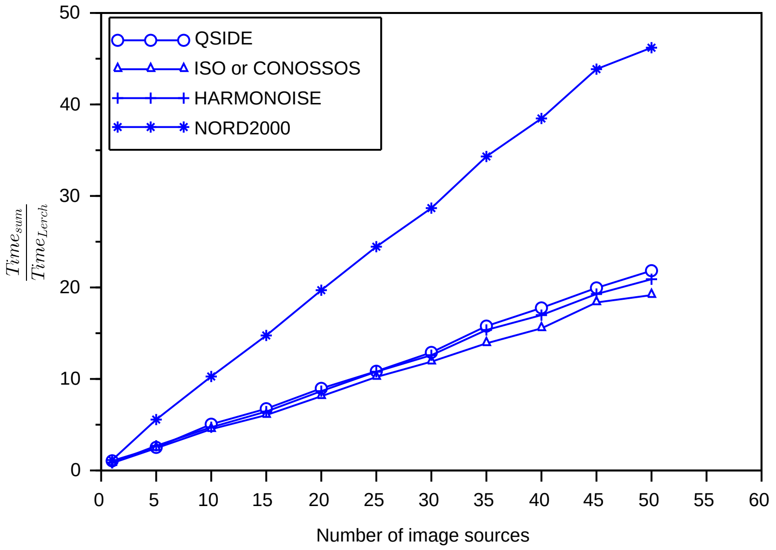

Figure 3.24: Time ratio between explicit sum and Hurwitz-Lerch transcendent. The barrier is 10 m wide and 10 high. The source and receiver is 10 m to the barrier façade and 10 m the barrier top, respectively. Every $y - axis$ value is the average of 100 times running. "QSIDE" indicates the model presented in this chapter. The other legends indicate the name of the engineering models.

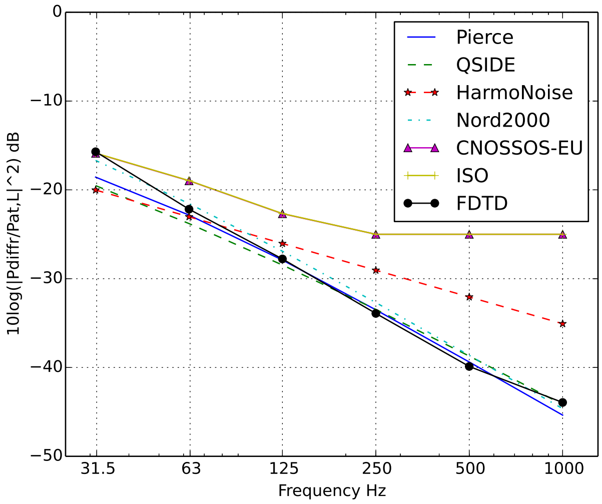

Figure 3.25: Comparison of different engineering models about the diffracted sound pressure level reference to the free field. The barrier is a thick barrier with 10 m width. The source is 4.8 m to the barrier façade and 10 m to the barrier top. Barrier width is 10 m. The receiver is 4.5 m to the barrier façade and 6.6 m to the barrier top.

dB compared with numerical simulations in most of the receiver positions under a low computing cost.

References

[1] JOSEPH B. KELLER. *Geometrical Theory of Diffraction*. Journal of the Optical Society of America, 52(2):116–130, February 1962.

[2] R.G. Kouyoumjian and P.H. Pathak. *A uniform geometrical theory of diffraction for an edge in a perfectly conducting surface*. Proceedings of the IEEE, 62(11):1448 – 1461, November 1974.

[3] Allan D. Pierce. *Diffraction of sound around corners and over wide barriers*. J. Acoust. Soc. Am., 55(5):941–955, 1974.

[4] Allan D. Pierce. *Acoustics: An Introduction to Its Pysical Principles and Applications*. Acoustical Society of America, New York, USA, 1989.

[5] T. Kawai. *Sound Diffraction by a Many-Sided Barrier or Pillar*. J. Sound Vib., 79(2):229–242, 1981.

[6] Hyun-Sil Kim, Jae-Sueng Kim, Hyun-Ju Kang, Bong-Ki Kim, and Sang-Ryul Kim. *Sound diffraction by multiple wedges and thin screens*. Applied Acoustics, 66(9):1102–1119, September 2005.

[7] Hequn Min and Xiaojun Qiu. *Multiple acoustic diffraction around rigid parallel wide barriers*. The Journal of the Acoustical Society of America, 126(1):179–186, 2009.

[8] Y. W. Lam and S. C. Roberts. *A simple method for accurate prediction of finite barrier insertion loss*. The Journal of the Acoustical Society of America, 93(3):1445–1452, 1993.

[9] I. Tolstoy. *Diffraction by a hard truncated wedge and a strip*. IEEE Journal of Oceanic Engineering, 14(1):4 –16, January 1989.

[10] Ivan Tolstoy. *Exact, explicit solutions for diffraction by hard sound barriers and seamounts*. The Journal of the Acoustical Society of America, 85(2):661–669, 1989.

[11] D Ouis. *Noise attenuation by a hard wedge-shaped barrier*. Journal of Sound and Vibration, 262(2):347–364, April 2003.

[12] K.M. Li and H.Y. Wong. *A review of commonly used analytical and empirical formulae for predicting sound diffracted by a thin screen*. Applied Acoustics, 66(1):45–76, January 2005.

[13] Glenn J. Wadsworth and James P. Chambers. *Scale model experiments on the insertion loss of wide and double barriers*. The Journal of the Acoustical Society of America, 107(5):2344–2350, 2000.

[14] Yh Berthelot and Jx Zhou. *Scale-Model Experiments on the Validity of the Matched Asymptotic Expansions Theory for Sound Diffraction by Curved Surfaces of Finite Impedance*. Journal of the Acoustical Society of America, 93(2):605–608, February 1993.

[15] W. Wei, D. Botteldooren, T. Van Renterghem, M. Hornikx, J. Forssén, E. Salomons, and M. Ögren. *Urban Background Noise Mapping: The General Model*. Acta Acust. United Ac, 100(6):1098–1111, 2014.

[16] K. Heutschi. *A simple method to evaluate the increase of traffic noise emission level due to buildings, for a long straight street*. Applied Acoustics, 44(3):259–274, January 1995.

[17] Pieter Thomas, Timothy Van Renterghem, Ellen De Boeck, Laurent Dragonetti, and Dick Botteldooren. *Reverberation-based urban street sound level prediction*. J. Acoust. Soc. Am., 133, 2013.

[18] Dezhang Chu and Timothy K. Stanton. *Higher order acoustic diffraction by edges of finite thickness*. The Journal of the Acoustical Society of America, 116(4):2566–2566, 2004.

[19] Klaus D Mielenz. *Computation of Fresnel Integrals. II*. J. Res. Natl. Inst. Stand. Technol., 105, 2000.

[20] Jérôme Defrance, Erik Salomons, Ingrid Noordhoek, Dietrich Heimann, Birger Plovsing, Greg Watts, Hans Jonasson, Xuetao Zhang, Eric Premat, Isabelle Schmich, François Aballea, Marine Baulac, and Foort de Roo. *Outdoor Sound Propagation Reference Model Developed in the European Harmonoise Project*. Acta Acust. Acust., 93:213–227, 2007.

[21] Erik Salomons, Dirk van Maercke, Jérôme Defrance, and Foort de Roo. *The Harmonoise Sound Propagation Model*. Acta Acust. Acust., 97(1), 2011.

[22] *Environmental Noise and the CNOSSOS-EU initiative*, 2012.

[23] Erik M Salomons, Henk Polinder, Walter J a Lohman, Han Zhou, Hieronymous C Borst, and Henk M E Miedema. *Engineering modeling of traffic noise in shielded areas in cities*. The Journal of the Acoustical Society of America, 126(5):2340–9, November 2009.

[24] Wolfgang Kropp, Jens Forssén, M. Ögren, and Pontus Thorsson. *The failure of traditional traffic noise control for quiet areas*. In Proc. Inter-Noise 2004, Prag, Czech Republic, 2004.

[25] Dick Botteldooren. *Finite-difference time-domain simulation of low-frequency room acoustic problems*. J. Acoust. Soc. Am., 98:3302–3308, 1995.

[26] Timothy Van Renterghem and Dick Botteldooren. *Prediction-step staggered-in-time FDTD: An efficient numerical scheme to solve the linearised equations of fluid dynamics in outdoor sound propagation*. Appl. Acoust., 68:201–216, 2007.

[27] Kurt Heutschi. *Calculation of Refelctions in an Urban Environment*. Acta Acust. Acust., 95:644–652, 2009.

4

Dynamic noise mapping: a map-based interpolation between noise measurements with high temporal resolution

★★★

Submitted to Applied Acoustics

Although these strategic noise maps have their merits, they also have some shortcomings: accuracy in predicted noise levels in shielded or quiet areas is not very high, the maps fail to capture sounds that are less easy to predict, and above all the dynamics of the sound environment is not included. However, these dynamics might be important to evaluate sleep disturbance and noise annoyance. In this chapter, a model to dynamically (every 15 min time interval) update the noise maps based on measurements is proposed. This model relies on reasonable good source and propagation models and a not-very-dense measurement network. The least mean squares method (LMS) is used for tuning model parameters. To avoid an under-determined system, the number of degrees of freedom is reduced by grouping the sources and propagation paths into different categories. Sources and propagations in the same category are corrected by offsetting the same small values from their basic levels. The map based interpolation is performed jointly on L_{Aeq}*,* L_{10} *and* L_{90}*, and takes into account 1/3 octave band spectra. The efficiency of the proposed method was validated in a case study in Katendrecht district of Rotterdam, the Netherlands.*

4.1 Introduction

Strategic noise maps have been calculated in many European countries as obliged by the environmental noise directive issued in 2002. Since then, such maps have become an important noise policy instrument, and allow identification of black points and draw statistics of population exposure to environmental noise [1, 2, 3, 4, 5]. Case studies and in-situ measurement [6, 7, 8] show that discrepancies between calculated and measured acoustical indicators can become quite large, especially at highly shielded urban zones. This inaccuracy mainly stems from assumptions made by the source or propagation models commonly applied. Simplifications implemented to allow fast evaluation could be a reason as well. Among others, the effect of meteorological effects, intermediate city canyons [9, 10], green roofs [11], roof details [12] and terrain details [13, 14] are not sufficiently captured.

Strategic noise maps, by concept, do not attempt to cover all environmental sound sources. For example, traffic on minor roads is seldom considered due to lack of basic data. Other sources such as recreational noise (pubs, music events, ...), (un)loading near shops, construction noise etc. are very difficult to grasp in strategic maps due to their unpredictable and temporal nature. However, these might have a strong impact on the urban soundscape.

Also the temporal variation is neglected in strategic noise maps, aiming at providing yearly averaged noise indicators. This might conflict with the more temporary perception of environmental noise by city dwellers. In addition, in order to estimate health-related impacts resulting from noise exposure, more detailed temporal information could be helpful. Shoulder hours could be important for estimating sleep disturbance [15], which would not be captured by L_{night} and require short-term variations in the map (e.g. 15 minute L_{Aeq}) to be obtained. On a shorter time scale, percentile levels or event counts could allow estimating notice-ability of environmental sounds.

These aforementioned considerations form the starting point of this work. The aim is to develop more accurate and dynamic maps based on continuous noise monitoring. The term “dynamic noise map” is used to refer to a noise map that is updated in short time intervals (e.g. every 15 minutes) based on measurements made in a dense, yet limited network of noise sensors. As a complement to an energy-based noise level indicator as L_{Aeq}, the proposed methodology can also include other indicators that could be relevant for the evaluation of the effect of noise on people such as the percentile levels L_{10} and L_{90}.

Recently, a procedure for obtaining a dynamic map was developed by assuming that sound propagation is independent of time, allowing to update levels at receivers by only considering temporal source power variations [16, 17]. However this method fails when meteorological effect cannot be assumed constant and inaccuracy in modelled propagation becomes observable. To increase spatial detail, one could use mobile measurement stations equipped with GPS to measure in a fine resolution grid [18]. The challenge in the latter lies in combining spatial and temporal detail [19]. Dynamic maps based on microscopic traffic simulations [20, 21] could resolve only part of the aforementioned issues and are moreover very CPU time costly.

In this chapter, a model-based interpolation method to calculate dynamic noise maps based on medium-density noise-monitoring networks is proposed that not only adapts the sound powers over time, but also accounts for temporal variations in the propagation conditions. Both equivalent levels and percentile noise levels are considered in this work. The basic assumption underlying the model-based interpolation is that there is a reasonably good model for predicting the sound indicators in the area under study. Inaccuracy may occur in the emission of the source but also in the calculated propagation. The interpolation will tune the source and propagation on the basis of measurements and in that way improve predictions at locations where no measurements are available.

This model will not be accurate for instantaneous noise level predictions given the 15-minute time frame. Suppose two microphones (A and B), separated by 200 m, near the edge of the same road. At the moment a car passes in front of microphone A, a very short time frame would demand the system to increase the source power level, while near B the opposite would be true. However, when the same car passes somewhat later in front of B, the opposite action would be needed. Given the concept of dynamic source level adaptation, microphones A and B should suggest the same source correction. This results in the fact that A and B share peak levels and background levels. Therefore, to predict the instantaneous event is beyond this study and the prediction of indicators L_{Aeq}, L_{10} and L_{90} will be focused.

This chapter is organized as follows. In section 4.2, the conceptual layout is introduced. In section 4.3, the methodology for correcting the source emission levels and propagation related parameters, based on measurements, is presented. In section 4.4, a case study is described using 8 microphones in a city quarter during a 2-month experiment. Finally, conclusions are drawn in section 4.5.

4.2 Underlying model and reducing degrees of freedom

The proposed method for dynamic interpolation relies on an underlying source and propagation model. This model has to be sufficiently accurate, but as it will be tuned based on measurements, the highest possible accuracy on source categorisation and propagation path calculation is not required. A careful balance between accuracy and efficiency will therefore be sought. Tuning model parameters based on measurements has to be based on a sufficiently small number of the degrees of freedom. The number of degrees of freedom that can be resolved is determined by the number of measurement stations and the assumptions on temporal coherence on the time scale considered in the sources. This section will focus on reducing the degrees of freedom.

4.2.1 Underlying model

4.2.1.1 Temporal aggregation: L_{Aeq} and L_N

It is obvious that models aiming at predicting instantaneous sound pressure levels, for example on a second by second basis, $L_{Aeq,1sec}$, would most likely fail. Moreover, even if interpolation between monitoring stations at a second by second basis were possible, the information obtained would be very hard to interpret. Thus a suitable aggregation period has to be chosen. This requires a careful balance between stability and repeatability at the one hand, and a sufficient degree of dynamics at the other hand. In an urban environment, the short term dynamics are mainly determined by passages of motorized vehicles [20]. A suitable aggregation period depends on the traffic intensity but 10 to 15 minutes have been chosen as an appropriate monitoring period. Sequential monitoring over such time intervals results in low standard errors between measurement periods for continuous traffic flows and still includes enough temporal resolution to capture typical (diurnal) activity patterns [22]. Finally, one should also consider the latency in calculating the updated maps. The shorter the temporal step, the larger the latency. Based on these considerations, a 15 minute temporal interval was chosen to produce the dynamic noise maps. The equivalent sound pressure level $L_{Aeq,15min}$ includes the total sound energy received at a measurement location. Every sound source, fixed or mobile, contributes an amount to this quantity independently. Moreover, the total energy over 15 minutes determines the L_{Aeq} independently of the emission moment. In addition, it is a preferred indicator for noise mapping. Besides L_{Aeq}, percentile noise levels L_N are also of importance when analysing the soundscape. L_{10} indicates the noise level exceeded 10% of the measurement time. L_{10} is therefore indicative for peak levels. L_{90} indicates the noise level exceeded 90% of the measurement time. Consequently, L_{90} can be considered as the background noise level. L_{10} and L_{90} are widely used in studies of noise disturbance and background noise quality. Although the model will be developed for L_{Aeq}, L_{10} and L_{90}, it can readily be extended to other parameters.

4.2.1.2 Model for predicting L_{Aeq}

The model for L_{Aeq} calculates the total contribution from all sources at point p and time t, for frequency f:

$$L_{eq,f}(p,t) = 10\log_{10}\sum_{i}^{N_s}\sum_{j}^{N_h} 10^{0.1[L'_{W,f,i}(t)-A'_{f,i,j}(p,t)]} \tag{4.1}$$

where the sources are labelled by index i and the propagation paths are labelled by index j which allows for different paths between the i^{th} source and location p; N_s is the number of sources and N_h is the total number of propagation paths; the primes stress that the theoretical value is modified based on the measurements.
The actual values for sound emission $L'_{W,f,i}$ and attenuation $A'_{f,i,j}$ now are obtained from their theoretical value $L_{W,f,i}$ and $A_{f,i,j}$ and the measured levels $L_{x,f,meas}(p_{meas},t)$. For this, it is assumed that the actual value deviates only by a "small" amount:

$$L'_{W,f,i}(t) = L_{w,f,i}(t) + \epsilon_{f,i}^{t-1} \tag{4.2}$$

$$A'_{f,i,j}(p,t) = A_{f,i,j}(p) + \delta_{f,i,j}^{t-1} \tag{4.3}$$

where, $L_{W,f,i}(t)$ is the source power level at time t. $L_{W,f,i}(t)$ can be calculated by a source model or it can be obtained from a close-proximity measurement. Both $\epsilon_{f,i}^{t-1}$ and $\delta_{f,i,j}^{t-1}$ are functions of frequency f and time t, but can be functions of several other parameters as well. Note that no explicit dependence of the theoretical attenuation on time is assumed and thus any variation that might occur will need to be captured by the correction term. Extracting $\epsilon_{f,i}^{t-1}$ and $\delta_{f,i,j}^{t-1}$ from the measurements $L_{x,f,meas}(p,t-1)$ will be done by the least mean squares method including restrictions on the size of ϵ_f and δ_f.

4.2.1.3 Model for predicting L_{10} and L_{90}

Fluctuations in noise levels can occur for different reasons: a spatially static sound sources can show a clear temporal pattern (e.g. a cooling unit switching on and off), a source could move or the propagation conditions from a spatially static source can change quickly for example due to wind gusts. The latter type of fluctuation will not be considered here. For spatially fixed sources with fluctuating emission, the relationship between equivalent noise level and percentile noise levels is directly determined by the source. However, for moving sources distance and speed have a strong influence on this relationship. In this work we will mainly consider road traffic as the moving sources. Rail and air traffic often only influence the low indexed percentile levels and can therefore easily be added.
A full microscopic traffic simulation allows to calculate percentile noise levels quite accurately [20, 21, 23, 24]. However, it also requires many parameters that do not relate to measured noise levels in a straight forward way. Steering microscopic traffic simulation from roadside noise measurements in real time is still beyond

the possibilities of today's computers, in particular when it has to be applied to a whole city. Therefore an alternative approach is followed.

The main assumptions behind this approach are (i) that the fluctuation in noise level due to road traffic is mainly caused by the traffic on the closest road, whereas more distant traffic only contributes to a relatively constant background hum, and (ii) that the relationship between L_{Aeq}, L_{10} and L_{90} is mainly influenced by the distance to this road, and by the traffic flow rate, the vehicle speed and the amount of heavy vehicles on this closest road. A simplified simulation model can then be used to estimate these relationships, based on the simulated temporal envelope of the sound level near a single road carrying free flow traffic [25]. For this, a 2 km stretch of a straight road was modelled, on which vehicles were loaded at one end, which then travelled to the other end. The number of vehicle passby's per time unit followed a Poisson distribution, which is typical for free flow traffic, containing platoons of various lengths. The emission of each vehicle was calculated using the Harmonoise/Imagine road traffic noise emission model, and free field propagation was used to calculate the instantaneous sound level at a receiver point next to the road in the middle of the 2 km segment. From the instantaneous sound level that was simulated at the location of the receiver, the relationship between L_{Aeq}, L_{A10} and L_{A90} was derived, and was tabulated for a range of scenarios in which vehicle speed, percentage of heavy vehicles, distance to the road and traffic flow were varied.

Within the dynamic noise mapping approach followed in this chapter, for each receiver, the distance to the closest road segment is determined and the contribution of this road to L_{Aeq} is extracted. Based on the traffic intensity and speed limit on this road, corresponding values for L_{10} and L_{90} are then extracted from the pre-calculated tables. For contributions to the traffic noise level that follow paths that contain multiple reflections, diffraction over buildings, or scattering on atmospheric turbulence, it is assumed that peaks in the sound level smooth out and consequently that L_{10}, L_{Aeq}, and L_{90} are almost equal. For those situations in which the receiver is close to more than one road, multiple contributions will need to be added. As the distribution of the sound level caused by each road separately is not known, a more elaborate derivation has to be made to obtain estimates of L_{10} and L_{90}. Details on this procedure can be found in Appendix A3.

4.2.2 Reducing degree of freedom

From equation (4.1), (4.2) and (4.3), it is clear that the number of unknown ϵ is N_s and the number of unknown δ is $N_s \cdot N_h$ for each immission point, which makes the system of equations - obtained from matching calculations and a limited number of sound observatories - to be solved strongly under determined. Moreover, many sources and propagation paths have extremely low influences on a particular immission point which also makes the system ill-conditioned. Additionally, for every update of the map the double sum has to be recalculated which amounts to $N_s \cdot N_h \cdot N$ calculations, where N is the number of measurement stations.

To limit the size of the sum over all N_s sources and the degrees of freedom in ϵ_f, sources need to be categorized. Categorization and grouping is particularly useful for sound sources that are spread over large areas such as road traffic noise. Categorizations of road traffic noise emission could depend on traffic intensity, speed limit, or other categorization methods. For example, grouping sources to highways, major city roads and minor city roads.

In the underlying noise mapping model, three categories of propagation paths are included for road traffic:

- 2D path, consisting of direct line-of-sight propagation, reflections or diffractions in the horizontal plane (near vertical edges).
- diffraction path, that is the contribution caused by multiple reflections and diffractions over roof tops (excluding the horizontal plane)[10].
- scattered path, this the contribution to the immission due to turbulence scattering and is mainly important in shielded areas [26].

It is essential to keep corrections on the above mentioned three propagations separately. It is expected that the “2D” path is estimated quite accurately, the “diffraction” path could be slightly inaccurate yet not time dependent while the “scattered” path may change significantly over time.

Although several possible propagation paths have been grouped in the above three categories, δ could still depend on the source-receiver positions. In this way, the correction term δ still contains a large degrees of freedom.

Two important assumptions are made to reduce the number of degrees of freedom: 1) it is assumed that the source corrections are identical in the same source category. The source correction $\epsilon_{f,i}$ then becomes $\epsilon_{f,m}$, where i is a source and m is a source category. 2) it is assumed that the propagation corrections are also identical in the same source category and the same propagation path. The propagation correction $\delta_{f,i,j}$ then becomes $\delta_{f,m,n}$, where m is a source category and n is a category of propagation paths.

Based on these categorizations, Equation (4.1) can be split to:

$$L_{eq,f}(p,t) = 10\log_{10}\left\{\sum_{n=1}^{N_n}\sum_{j\in n}\sum_{m=1}^{N_m}\sum_{i\in m}10^{0.1\left[L'_{W,f,i}(t)-A'_{f,i,j}(p,t)\right]}\right\} \tag{4.4}$$

where $i \in m$ refers to i belonging to the source category m and $j \in n$ refers to j belonging to the propagation category n. N_m is the total number of source categories and N_n is the total number of categories of propagation paths. The corrections for the same source or propagation category are supposed to be the same. Therefore the corrections mentioned in equation (4.2) and equation (4.3) can be moved out for the same category. The sum then changes to:

$$L_{eq,f}(p,t) = \\ 10\log_{10}\left\{\sum_{m=1}^{N_m} 10^{0.1\epsilon^t_{f,m}} \sum_{n=1}^{N_n} 10^{-0.1\delta^t_{f,m,n}} \sum_{j\in n}\sum_{i\in m} 10^{0.1[L_{W,f,i}(t)-A_{f,i,j}(p,t)]}\right\} \tag{4.5}$$

The double sum $\sum_{j\in n}\sum_{i\in m} 10^{0.1[L_{W,f,i}(t)-A_{f,i,j}(p,t)]}$ indicates a separate noise map calculated based on source category m and propagation category k. Therefore the most time consuming part can be calculated before hand to save the updating time.

Clearly, the double sum $\sum_{j\in n}\sum_{i\in m} 10^{0.1[L_{W,f,i}(t)-A_{f,i,j}(p,t)]}$ is the total contribution of a source category by a propagation category, which can be calculated and stored in advance. The number of degrees of freedom reduces from $N_s \cdot N_h \cdot N$ to $N_m \cdot N_n \cdot N$, where N is the number of measurement stations.

The discussion on the underlying model and reduction of degrees of freedom explicitly depends on frequency, for example per 1/3 octave band. Although in principle there are no fundamental constrains in performing the fit to measurements on a frequency per frequency basis, the additional freedom jeopardizes the uniqueness of the solution and thus could easily lead to over-fitting. Therefore in this work it is assumed that 1) the traffic source spectrum is reasonably accurate; 2) the spectrum of atmospheric attenuation is reasonably accurate. In that case it can be assumed that the corrections on both sound power and propagation are independent on frequency. For industrial noise, explicitly including frequency dependent corrections is more appropriate unless sound power spectra are explicitly obtained from a separate measurement.

4.3 Calculate the correction term ϵ for sources and δ for propagation path

The correction terms are obtained by minimizing the squared error between the predictions and measurements:

$$e = \min\left\{\sum_{p}^{N}\left(\frac{1}{8}\sum_{f}[L_{eq,f}(p,t)-L_{eq,f,meas}(p,t)]^2+\sum_{x}[L_x(p,t)-L_{x,meas}(p,t)]^2\right)\right\} \tag{4.6}$$

where p is the measurement position; x is the percentile indicator which either is 10 or 90 in this publication; f is frequency. As shown in equation (4.6), the frequency dependency of L_{eq} is explicitly taken into account while this is not the case for the percentile levels where only the overall A-weighted level is used. The main reason for this is that the spectrum of percentile levels is ill-defined, yet one could think of a useful extension of the algorithms in this direction. Assuming that equation (4.6) has a unique minimum, letting the partial derivative with respect to the variables ϵ and δ of the sum in equation (4.6) equal to zero respectively, the minimum is achieved and ϵ and δ can then be resolved. In this publication a slightly different approach is assumed.

Inspired by the least mean squares algorithm (LMS) that is popular in signal processing, equation (4.6) is not resolved explicitly at every time step but on average over a longer time period hereby assuming that ϵ and δ change only slowly with time. As in signal processing it is then assumed that the minimum in the error function will be reached by taking small steps in the direction of the minimum taking into account only the instantaneous values in calculating the derivative. Note that in situations where LMS is used in signal processing the uniqueness of the solution and convergence can be proven, yet this is not the case here. Application will show to what extend convergence can be reached. The correction of sources o category m, ϵ_m, and correction of propagation path of source category m and propagation category n, $\delta_{m,n}$, can be updated in the same way as:

$$\epsilon_m^t \approx \epsilon_m^{t-1} - \frac{\partial}{\partial \epsilon_m^{t-1}} \left\{ \mu_\epsilon \sum_p^N \left(\frac{1}{8} \sum_f [L_{eq,f}(p,t) - L_{eq,f,meas}(p,t)]^2 + \sum_x [L_x(p,t) - L_{x,meas}(p,t)]^2 \right) + \beta'_\epsilon \left(\epsilon_n^{t-1}\right)^2 \right\} \tag{4.7}$$

where μ_ϵ is a small number. β'_ϵ is a regularisation constrain that keeps ϵ_m^{t-1} small. Merging the constant into β_ϵ, equation (4.7) changes to:

$$\begin{aligned} \epsilon_m^t &= \epsilon_m^{t-1}(1-\beta_\epsilon) - \mu_\epsilon \sum_p^N \left\{ \frac{1}{8} \sum_f 2\left[L_{eq,f}(p,t) - L_{eq,f,meas}(p,t)\right] \frac{\partial}{\partial \epsilon_m^{t-1}} L_{eq,f}(p,t) \right. \\ &+ \left. \sum_x 2\left[L_x(p,t) - L_{x,meas}(p,t)\right] \frac{\partial}{\partial \epsilon_m^{t-1}} L_x(p,t) \right\} \end{aligned} \tag{4.8}$$

Similarly,

$$\begin{aligned} \delta_{m,n}^t &= \delta_{m,n}^{t-1}(1-\beta_\delta) - \mu_\delta \sum_p^N \left\{ \frac{1}{8} \sum_f 2\left[L_{eq,f}(p,t) - L_{eq,f,meas}(p,t)\right] \frac{\partial}{\partial \delta_{m,n}^{t-1}} L_{eq,f}(p,t) \right. \\ &+ \left. \sum_x 2\left[L_x(p,t) - L_{x,meas}(p,t)\right] \frac{\partial}{\partial \delta_{m,n}^{t-1}} L_x(p,t) \right\} \end{aligned} \tag{4.9}$$

4.3.1 Calculate source correction ϵ

To quantify the contribution of L_{Aeq} for the correction of source category m, the derivative $\frac{\partial}{\partial \epsilon_m^{t-1}} L_{eq,f}(p,t)$ and $\frac{\partial}{\partial \epsilon_m^{t-1}} L_x(p,t)$ need to be solved. Substituting equation (4.5) into the derivative and using the technique of derivative of implicit functions leads to:

$$\frac{\partial}{\partial \epsilon_m^{t-1}} L_{eq,f}(p,t) = \frac{10}{\ln 10} \frac{1}{10^{0.1 L_{eq,f}(p,t)}} \\ \frac{\partial}{\partial \epsilon_m^{t-1}} \left\{ \sum_{m=1}^{N_m} 10^{0.1 \epsilon_m^{t-1}} \sum_{n=1}^{N_n} 10^{-0.1 \delta_{m,n}^{t-1}} \sum_{j \in n} \sum_{i \in m} 10^{0.1[L_{W,f,i}(t) - A_{f,i,j}(p,t)]} \right\} \tag{4.10}$$

Since the correction for different source categories are independent from each other, the derivative of other categories ($\neq m$) with respect to ϵ_m^{t-1} will vanish, which means $\frac{\partial}{\partial \epsilon_m^{t-1}} \sum_{m=1}^{N_m} 10^{0.1 \epsilon_m^{t-1}} = \frac{\partial}{\partial \epsilon_m^{t-1}} 10^{0.1 \epsilon_m^{t-1}}$. Equation (4.10) is simplified as:

$$\frac{\partial}{\partial \epsilon_m^{t-1}} L_{eq,f}(p,t) = \frac{10^{0.1 \epsilon_m^{t-1}} \sum_{n=1}^{N_n} 10^{-0.1 \delta_{m,n}^{t-1}} \sum_{j \in n} \sum_{i \in m} 10^{0.1[L_{W,f,i}(t) - A_{f,i,j}(p,t)]}}{10^{0.1 L_{eq,f}(p,t)}} \tag{4.11}$$

To explain:

- $L_{W,f,i}(t)$ is power level of i^{th} source, which may be calculated by the traffic source power model;

- $\sum_{j \in n} \sum_{i \in m} 10^{0.1(L_{W,f,i}(t) - A_{f,i,j}(p,t))}$ is the sound power calculated from all source in the same category to the measurement position p by n^{th} propagation path category, where $n = 1$ is the 2D sound path, $n = 2$ is the diffracted sound path and $n = 3$ is the turbulence scattering sound path;

- $10^{0.1 \epsilon_m^{t-1}} \sum\limits_{n=1}^{N_n} 10^{-0.1 \delta_{f,m,n}^{t-1}} \sum\limits_{j \in n} \sum\limits_{i \in m} 10^{0.1[L_{W,f,i}(t) - A_{f,i,j}(p,t)]}$ is the sound power calculated from all the sources in the same category to the measurement position by all propagation paths. This value includes the source correction term ϵ_m^{t-1} and propagation correction term $\delta_{m,n}^{t-1}$

- $10^{0.1 L_{eq,f}(p,t)}$ is the total equivalent energy which can be calculated by equation (4.5)

Similar as the aforementioned analysis, the derivatives $\frac{\partial}{\partial \epsilon_m^{t-1}} L_x(p,t)$ can also be derived. However, L_{10} and L_{90} cannot be calculated as straightforward as $L_{eq,f}$. Details of calculating L_{10}, L_{90} and their derivative to ϵ_m^{t-1} and $\delta_{m,n}^{t-1}$ can be found in Appendix.

According to equation (4.8) and (4.11) in the previous sections and putting the constants into a fitting parameter, the correction term ϵ for a specified source category m becomes:

$$
\begin{aligned}
\epsilon_m^t \quad = \quad & \epsilon_m^{t-1}(1-\beta_\epsilon) - \mu_\epsilon \sum_p^N \Bigg\{ \left[L_{eq,f}(p,t) - L_{eq,f,meas}(p,t)\right] \\
& \frac{10^{0.1\epsilon_m^{t-1}} \sum\limits_{n=1}^{N_n} 10^{-0.1\delta_{m,n}^{t-1}} \sum\limits_{j\in n} \sum\limits_{i\in m} 10^{0.1[L_{W,f,i}(t) - A_{f,i,j}(p,t)]}}{10^{0.1 L_{eq,f}(p,t)}} \\
& + (L_{10} - L_{10,meas}) \frac{\partial}{\partial \epsilon_m^{t-1}} L_{10} + (L_{90} - L_{90,meas}) \frac{\partial}{\partial \epsilon_m^{t-1}} L_{90} \Bigg\}
\end{aligned}
\tag{4.12}
$$

4.3.2 Calculate propagation correction δ

The LMS method is also used to calculate $\delta_{m,n}^t$. Similar procedure is applied as when formulating the ϵ_m^t. Also note that the corrections for different propagation paths are independent, meaning that the derivatives to paths other than n will vanish. The derivative can be simplified to:

$$
\begin{aligned}
& \frac{\partial}{\partial \delta_{m,n}^{t-1}} L_{eq,f}(p,t) = \frac{10}{\ln 10} \frac{1}{10^{0.1 L_{eq,f}(p,t)}} \\
& \frac{\partial}{\partial \delta_{m,n}^{t-1}} \left\{ \sum_{m=1}^{N_m} 10^{0.1\epsilon_m^{t-1}} \sum_{n=1}^{N_n} 10^{-0.1\delta_{m,n}^{t-1}} \sum_{j\in n} \sum_{i\in m} 10^{0.1[L_{W,f,i}(t) - A_{f,i,j}(p,t)]} \right\} \\
= \quad & -\frac{10^{0.1\epsilon_m^{t-1}} 10^{-0.1\delta_{m,n}^{t-1}} \sum\limits_{j\in n} \sum\limits_{i\in m} 10^{0.1[L_{W,f,i}(t) - A_{f,i,j}(p,t)]}}{10^{0.1 L_{eq,f}(p,t)}}
\end{aligned}
\tag{4.13}
$$

According to equation (4.9) and (4.13), the correction term δ for a specified source category m and propagation path n becomes:

$$\delta^{t}_{m,n} = \delta^{t-1}_{m,n}(1-\beta_{\delta}) - \mu_{\epsilon}\sum_{p}^{N}\Bigg\{ -\left[L_{eq,f}(p,t) - L_{eq,f,meas}(p,t)\right] \frac{10^{0.1\epsilon^{t-1}_{m}}\,10^{-0.1\delta^{t-1}_{m,n}}\sum_{j\in n}\sum_{i\in m}10^{0.1[L_{W,f,i}(t)-A_{f,i,j}(p,t)]}}{10^{0.1L_{eq,f}(p,t)}} + (L_{10}-L_{10,meas})\frac{\partial}{\partial\delta^{t-1}_{m,n}}L_{10} + (L_{90}-L_{90,meas})\frac{\partial}{\partial\delta^{t-1}_{m,n}}L_{90}\Bigg\} \tag{4.14}$$

The details of solving $\frac{\partial}{\partial\delta^{t-1}_{m,n}}L_{10}$ and $\frac{\partial}{\partial\delta^{t-1}_{m,n}}L_{10}$ can be found in the Appendix.

4.3.3 Implementation method

To fit these correction parameters, the system is designed as 1) calculate the noise map for propagation paths “2D”, “diffraction” and “scattered” for all the categorized sources and extra sources; 2) query the server for measurement data at a start time stamp; 3) run the LMS method to obtain ϵ and δ; 4) move forward the time stamp (in this case the time step is 15 min). This approach is summarized in the flow-chart shown in figure (4.1). By this method, $\sum_{j\in n}\sum_{i\in m}10^{0.1(L_{W,f,i}(t)-A_{f,i,j}(p,t))}$ can be calculated and stored in advance.

4.4 Case study

The Katendrecht district of Rotterdam, the Netherlands, is considered to validate the proposed dynamic mapping model. This district is located on a peninsula with 1.18 km^2 area and around 4445 residential inhabitants [27]. The main noise source is the road traffic noise during day time. During night, industrial sources to the south of the peninsula may become important. The grouping of noise sources assumes similar uncertainty on the accuracy of the source data within one group. Inaccuracy can be attributed to traffic information or emission data for individual vehicles. The latter in turn depends on the fleet composition (including tires and maintenance) and on the road surface. Fleet maintenance, tires, etc. is expected to be relatively constant over a whole city. Road surface and road maintenance state may differ amongst neighbourhoods or districts. But for the area under study which is relatively small and homogeneous it can be assumed similar for the whole area. Hence, in this particular case, there is no need to categorize the traffic sound sources depending on their location. Uncertainty on traffic information and its effect on sound emission often depends on traffic intensity. Highway traffic and traffic on main arterial roads is know with much higher accuracy than traffic on local access roads for example. Therefore traffic sources are grouped into four

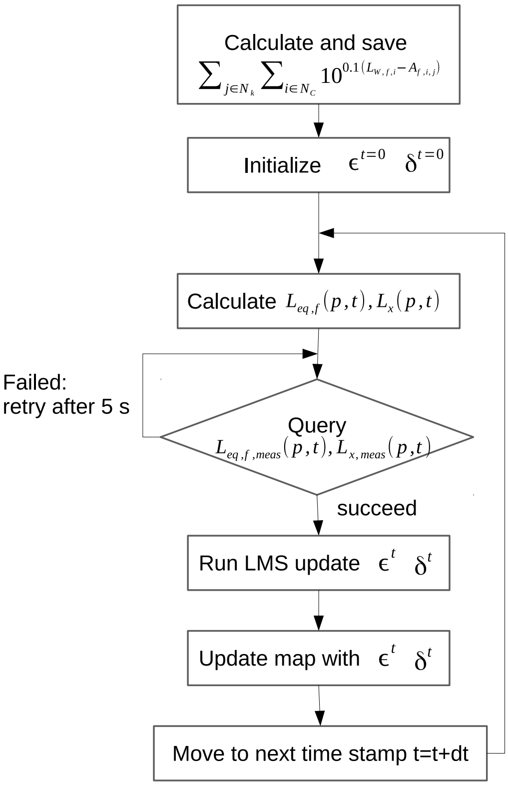

Figure 4.1: Implementation flow of the model.

categories based on traffic intensity or sound power level used in the calculation of strategic noise maps which can be considered a proxy for the latter. For road traffic, sound power levels for every 10m stretch of road are available from strategic noise mapping. Since the sound power levels of the traffic sources are not heavy tailed distributions, categorisation is done by using the Jenks-natural-breaks classification method [28]. This method seeks to minimize the variance inside a group and maximize the variance between groups (4.15) and (4.16):

$$\min\left\{\sum_{a=u}^{v}\left(A[a]-mean_{u,v}\right)^2\right\} \tag{4.15}$$

$$\max\left\{\sum_{b=t}^{s}\left(mean_t-mean_b\right)^2\right\} \tag{4.16}$$

The basic data set does not contain traffic information on a 15 minute resolution. Therefore, diurnal patterns for traffic are extracted from event counts in a couple of sensor nodes that are close to the road side. A similar diurnal pattern is assumed for all other roads. The industrial sources are considered as a separate source category, which are represented by 4 separate point sources with the same source power spectrum. The first estimate for the spectrum of industry source power is determined from far field measurement. The categorized spectrum is shown in figure (4.2) as L_{WAday}, $L_{WAevening}$ and $L_{WAnight}$, respectively.

Eight measurement stations [29, 30] are placed on buildings in the peninsula, as shown in figure (4.3(a)). Six of them are used to calculate the source correction ϵ and propagation correction δ. The two remaining microphones are used to validate the model. In this case study, L_{Aeq} (including spectrum information), L_{10} and L_{90} per 15 min is extracted from the measurement station to create the dynamic map.

Partial noise maps are calculated for the “2D” path [31], the “diffraction” path [10] and the “scattered” path [26] for each of the 5 source categories. For the “2D” path, 1 reflection and 1 diffraction on vertical edges (horizontal plane) are taken into account and the buildings are assumed to have a reflection coefficient of 0.95. When calculating the “diffraction” path, sources within 1500 m from the receiver are considered; when calculating the “scattered” path, the structure parameters of velocity and temperature are $C_v^2 = 0.01$ and $C_t^2 = 0.002$, respectively. For the “diffraction” and “scattering” path, the reflections in the vertical plane are explicitly included, where assuming the length of the street is much longer than the height of the buildings. However, for real measurement, the coherence is very strong when the measurement position is close to a reflector. In this case study, the measurement sensors are often placed on the façade of buildings. Therefore 3 dB are removed from the measurement to avoid the coherence between the direct and reflect sound [10][32][33].

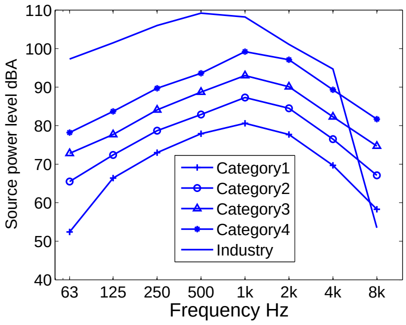

(a) $L_{W\,Aday}$

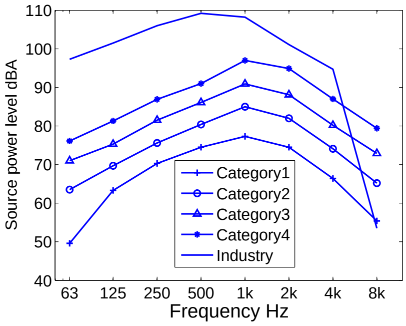

(b) $L_{W\,Aevening}$

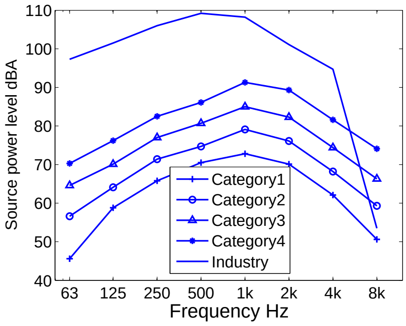

(c) $L_{W\,Anight}$

Figure 4.2: Spectrum of the categorized road traffic noise sources and the industry sources.

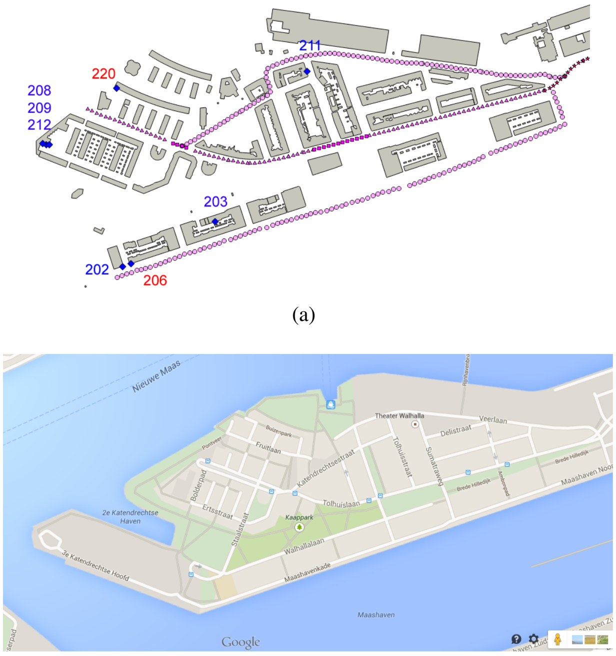

(a)

(b)

Figure 4.3: Building structure with indication of the microphone nodes in the case study region. In (a), the validation positions are indicated in red with ID's 206 and 220. The circles are the sources from category 1; the triangles are for category 2; the squares are for category 3 and the stars are for category 4. In (b), an overview of the validation site is shown by a Google map.

4.4.1 Analysis of fitting parameters

Based on the measured and predicted noise levels, and according to the procedure mentioned in the previous section, the correction coefficients ϵ and δ are found, as shown in figures (4.4) to (4.9). The corrections ϵ and δ are separated to values of “day”, “evening” and “night”. This is required because at the one hand the LMS procedure slowly adapts the corrections to more suitable values and on the other hand, the input data for road traffic has fixed values for day, evening, and night. Moreover, one can expect that the corrections are more similar between subsequent nights than between day and night periods as traffic sound shows a clear diurnal pattern. In other words, there is more similarity between the uncertainty in noise emission at 4 am on Monday and 4 am on Tuesday than there is between 4 am and 8 am on Tuesday for example. Generally, the results show that the source power is overestimated and the attenuations are underestimated. Additionally, the correction during the “day” are greater than during “evening” and “night”. Source category 1 is close to the measurement positions but their strength is low, therefore it seems logical that the corrections on its “2D” path is more important than its “diffraction” and “scattered” path, as shown in figure (4.5) where the δ of “2D” path is above the other two paths. Category 2 is further away from most of the fitting positions and its source power is low. This category then has a very limited contribution to the sound level. Figure (4.4) and figure (4.6) shows that the source correction ϵ and propagation correction δ are consequently very small. The effect of category 3 and category 4 are stronger than category 2 as shown in figure (4.7) and (4.8). These sources are mostly screened so only small adaptations to the direct field are expected. The overestimation of the “scattered” path is probably caused by the strong turbulence strength. The “2D” path and “diffraction” path are fairly calculated. According to equation (4.11) and equation (4.13), the correction of ϵ^t depends on the contribution of all propagation paths in one specific category, whilst, the correction of δ^t only depens on the contribution of a specific propagation path in one specific category. Therefore, the change of sources are assumed more quickly than the propagations. It is logical that the sources have strong dynamic patten than the propagations. In this fitting system $\mu_\epsilon > \mu_\delta$ is recommended.

For road traffic source category 1, its correction of the propagation path “diffraction” and “scattered” are smaller compared to the “2D” path correction which does not necessarily imply that the diffraction and scattered paths are more accurately predicted but could also be caused by the “2D” path dominating the overall propagation. From road traffic source category 2 and 3, the corrections on the “diffraction” and “scattered” increase to be dominant. According to the source positions in the case study (as shown in figure (4.3(a))), the multiple reflections and scattering would probably dominate the propagation and thus are more likely to be adapted. Similarly, the ϵ and δ for the industrial source powers and their propagation are

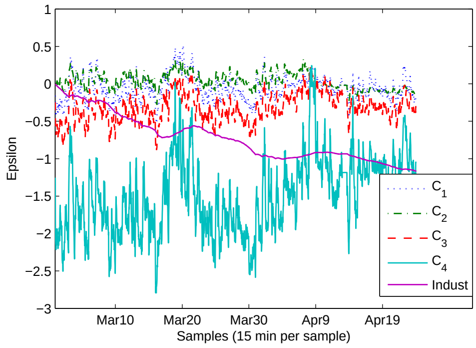

(a) day

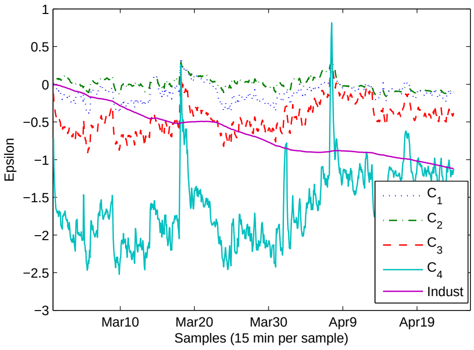

(b) evening

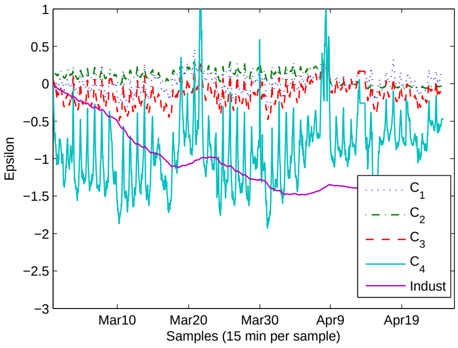

(c) night

Figure 4.4: Adapting curve of the categorized traffic sources. C_1, C_2, C_3 *and* C_4 *indicates the category number.*

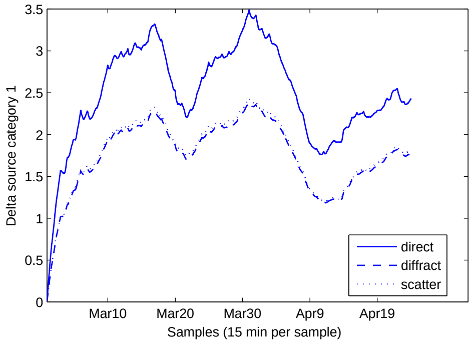

(a) day

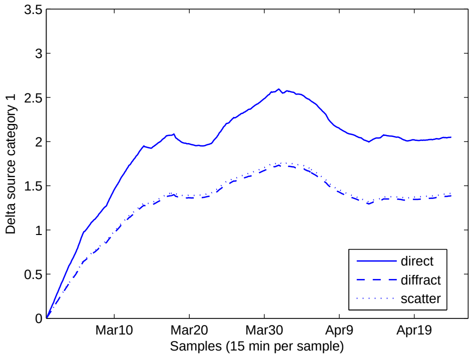

(b) evening

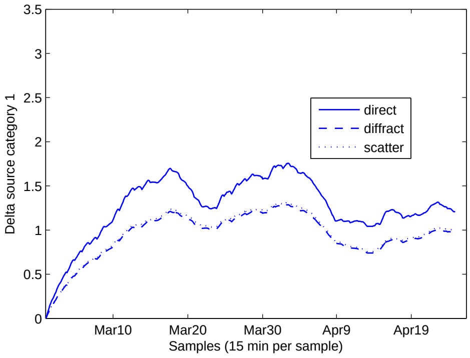

(c) night

Figure 4.5: Adapting curve of the propagation term δ for the traffic sources category 1. "direct" indicates the propagation correction for the direct sound path; "diffraction" indicates the diffraction path and "scattered" indicates the turbulence scattering path.

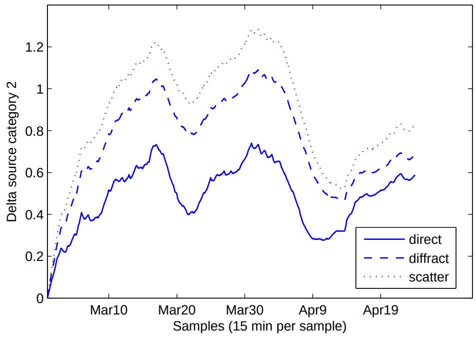

(a) day

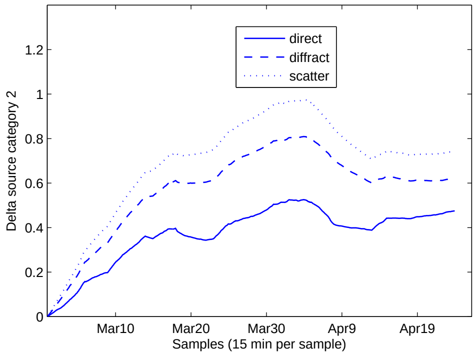

(b) evening

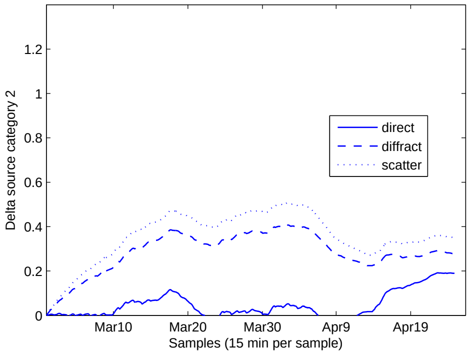

(c) night

Figure 4.6: Adapting curve of the propagation term δ for the traffic sources category 2.

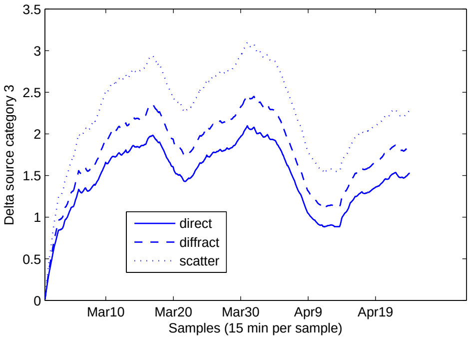

(a) day

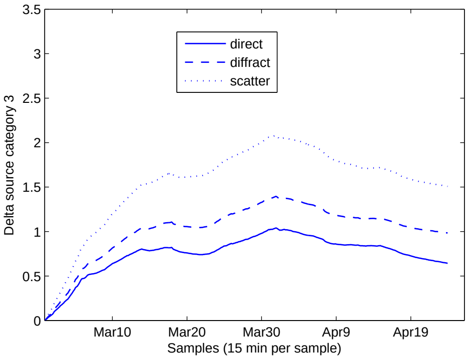

(b) evening

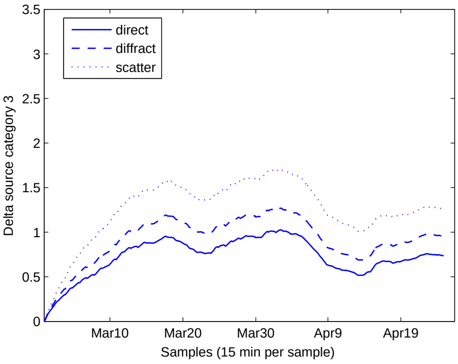

(c) night

Figure 4.7: Adapting curve of the propagation term δ for the traffic sources category 3.

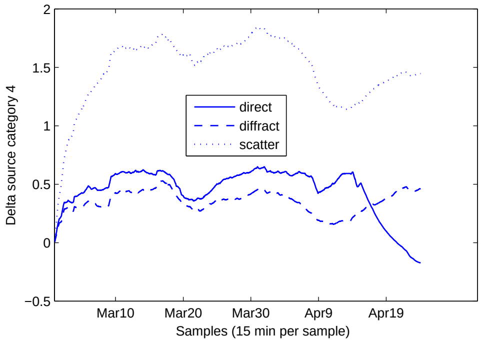

(a) day

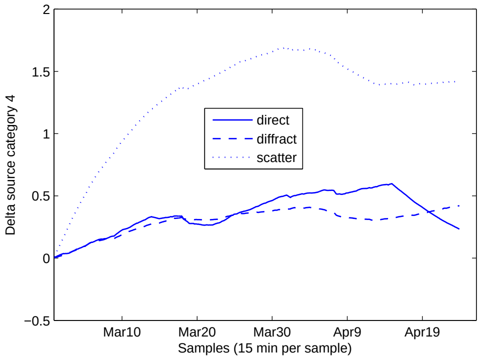

(b) evening

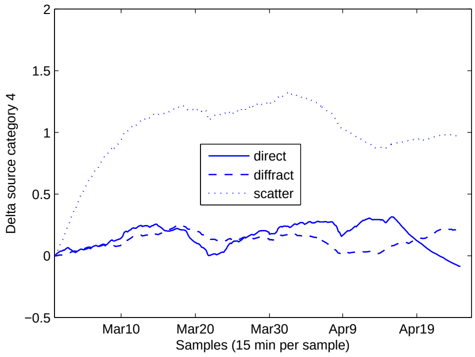

(c) night

Figure 4.8: Adapting curve of the propagation term δ for the traffic sources category 4.

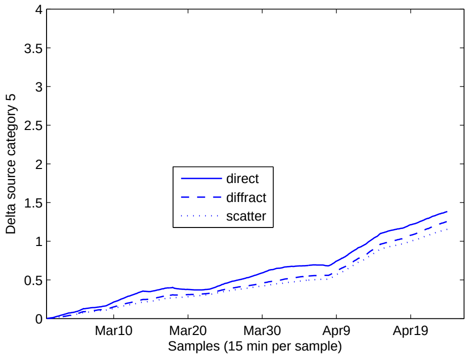

(a) day

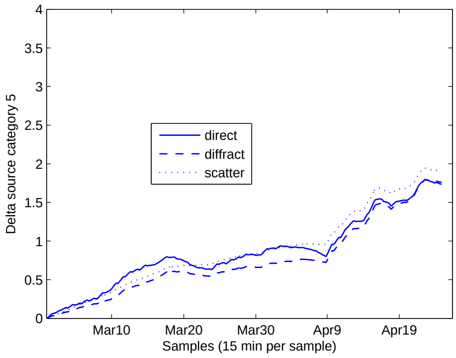

(b) evening

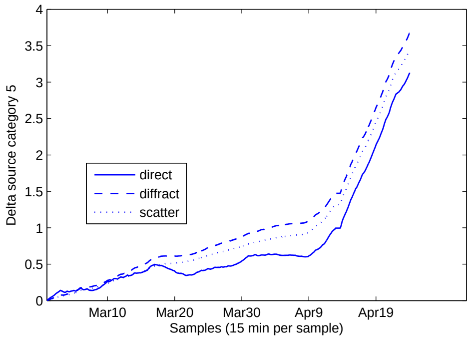

(c) night

Figure 4.9: Adapting curve of the propagation term δ for the industry sources category.

also adapted. Figures (4.4) and (4.9) show the source and propagation corrections which do not seem to converge over the period of several weeks that is considered here. According to equations (4.12) and (4.14), if the contribution of the non-traffic sources are mainly caused by one propagation path and the non-traffic sources are simplified by only a few points sources, the source correction ϵ and propagation correction δ would be difficult to distinguish from each other. In this case, the model might not recognize whether the source or the propagation is responsible for the mismatch between the predicted and measured sound pressure level. More measurement positions closer to the sources that can separate the contribution strength of sources and different propagation paths are therefore necessary.

4.4.2 Validation

Using the corrections adapted from measurements, the predicted, L_{Aeq}, both at the fitting locations and checking locations are improved, as shown in figures (4.10), (4.11) and (4.12) which are based on 45 days of fitting. Figure (4.10) shows that more than 75% percent of the $L_{Aeq,15min}$ at the validation positions matches measurements better than before correction. According to figure (4.10), the improvement of L_{Aeq} ranges typically from 0 dB to 5 dB. Also for L_{90}, similar improvement is achieved as shown in figure (4.12). However, the improvement of L_{10} is not as good as for L_{Aeq} and L_{90}. The main reason is that the original predictions using the model mentioned in section 4.2.1.3 were already quite accurate. Figure (4.13) shows the relation between the adapted and original predictions of L_{10}. Clearly, the errors of many original predictions are already less than 5 dB. If the difference $L_{Aeq} - L_{Aeq,meas}$ and $L_{90} - L_{90,meas}$ push the corrections to the opposite direction compared to $L_{10} - L_{10,meas}$, the prediction of L_{10} would become worse. Moreover, at moments and locations where the difference between measured and predicted L_{10} are high, non-mapped sound sources may also contribute to the sound environment. However, the improved predictions still outweigh the worsened ones.

Figures (4.14) to (4.16) show an L_{Aeq} noise maps at 5:00 am, 6:00 am and 7:00 am. Some dynamic changes between the noise map of 5:00 am and 6:00 am were captured by this model. Expected significant changes between 6:00 am and 7:00 due to rush hour are easily observed.

4.5 Discussion and conclusion

An improved noise mapping based technique for interpolating between noise measurements in urban noise sensing networks is proposed. The underlying model distinguish between 2D propagation, diffraction over buildings including multiple

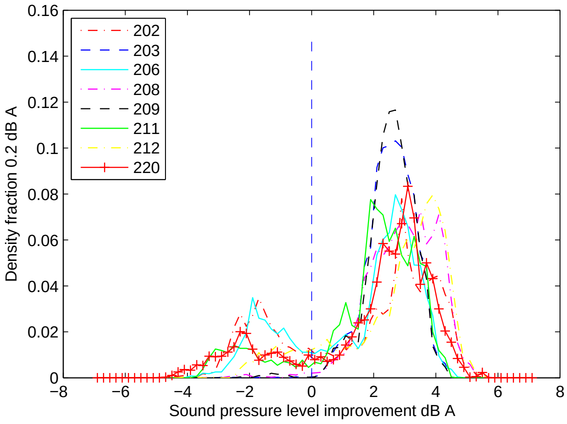

(a) Density function

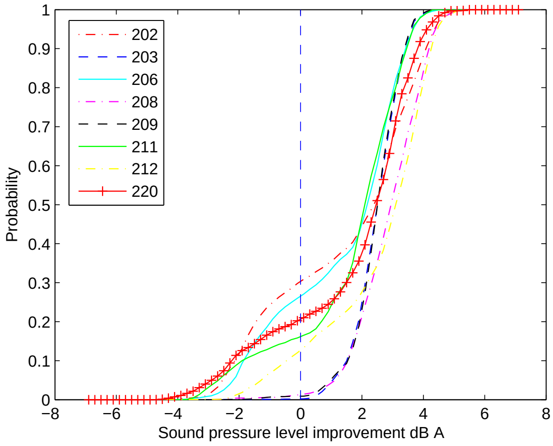

(b) Cumulative probability function

Figure 4.10: Density function and cumulative probability function of the improvement on the predicted L_{Aeq}. Negative values indicate that predictions become worse and positive values indicate the prediction is improved after correcting. 206 and 220 are the two validating positions.

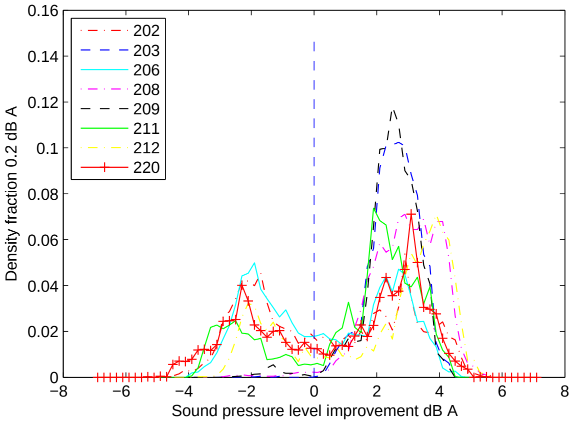

(a) Density function

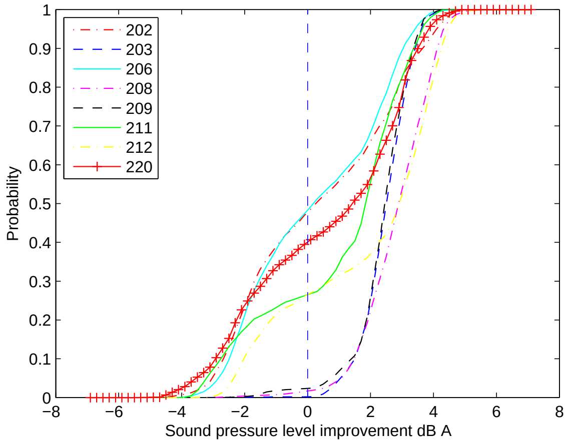

(b) Cumulative probability function

Figure 4.11: Density function and accumulative probability function of the improvement on the predicted L_{10}.

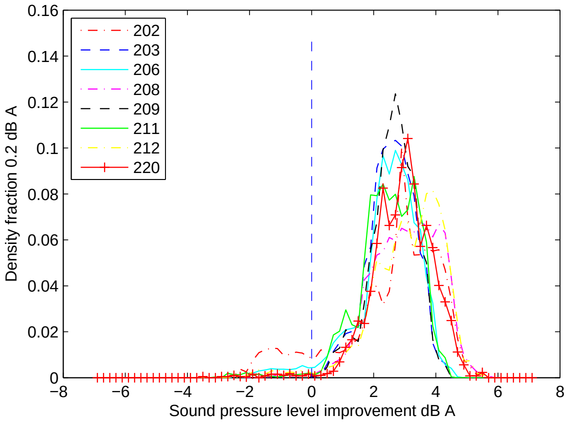

(a) Density function

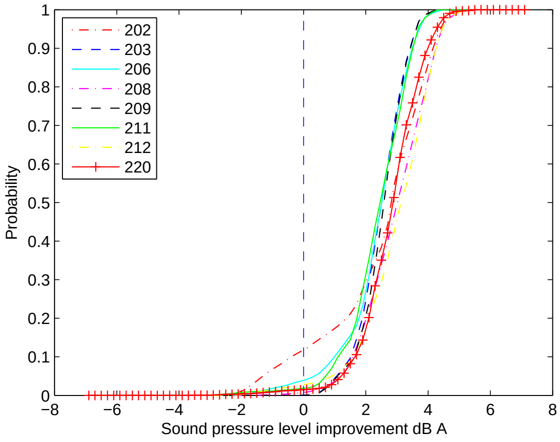

(b) Cumulative probability function

Figure 4.12: Density function and accumulative probability function of the improvement on the predicted L_{90}.

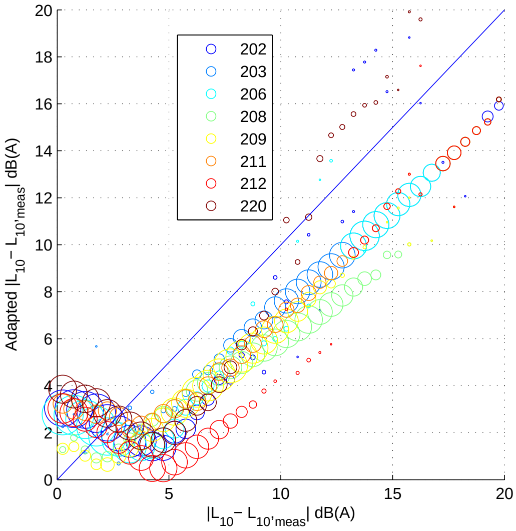

Figure 4.13: Original and adapted predictions of L_{10}. Circle positions indicate the predicted errors; the circle radii indicate the number of predictions with this accuracy.

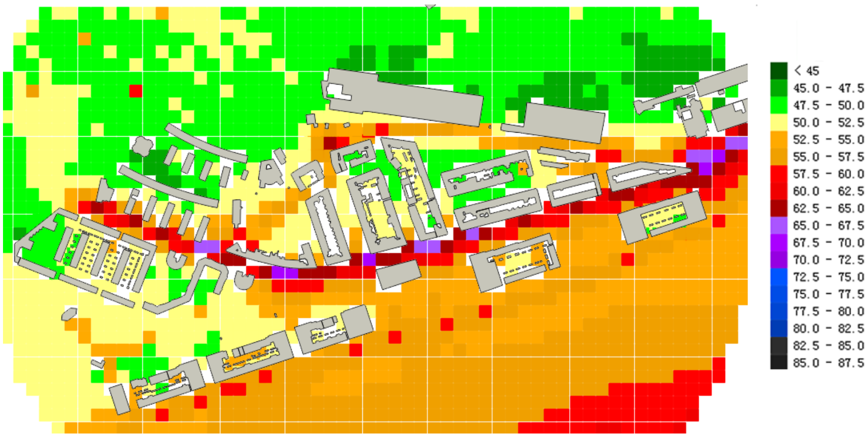

Figure 4.14: Noise map at 5:00 am.

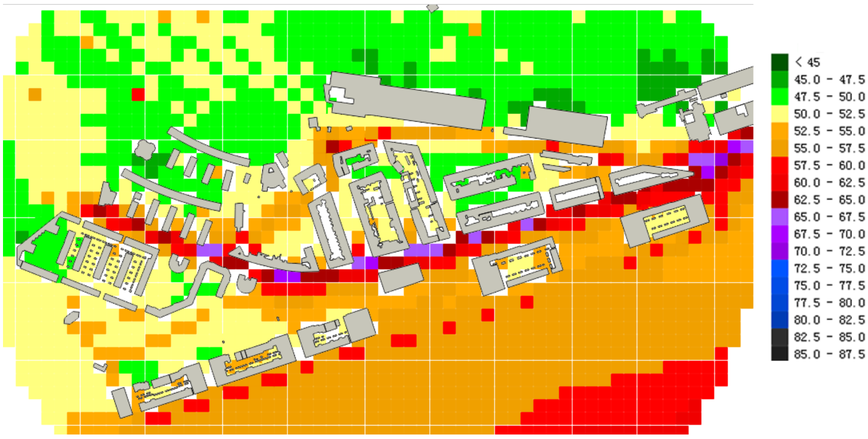

Figure 4.15: Noise map at 6:00 am.

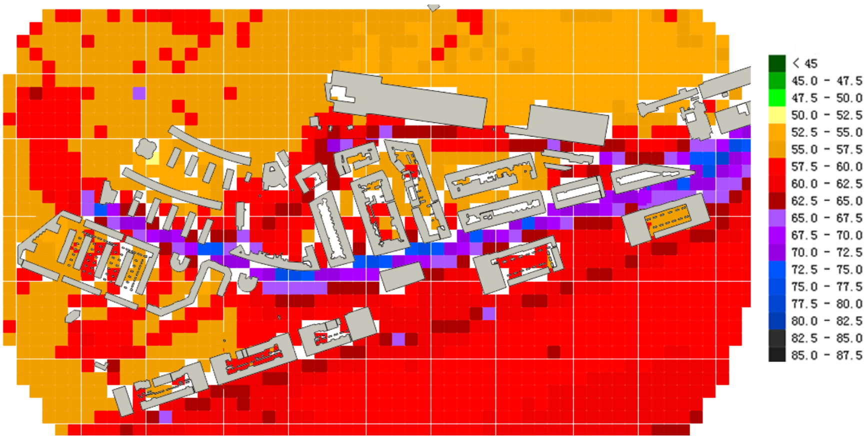

Figure 4.16: Noise map at 7:00 am.

reflections in street canyons, and turbulence scattering. In doing so calculation speed and accuracy are combined. In contrast to earlier work, the interpolation adapts not only source powers but also propagation. For this, it relies on optimal source grouping and an LMS adaptation algorithm that slowly adapts the corrections needed taking into account a regularization parameter that prevents over-fitting. Dynamic noise maps are obtained not only for L_{Aeq} but also for percentile noise levels, giving L_{10} and L_{90} as an example. The analysis of the case study shows that this method could considerably increase correspondence between models and measurements for L_{Aeq} and L_{90}. The main improvement range is between 0 dB and 5 dB with a peak at 3 dB. The improvement on L_{10} is not as good as for L_{Aeq} or L_{90}. The reason could be that the presented method to calculate L_{10} is already accurate but also that non-mapped sources could contribute. Although increasing the source power or decreasing of the attenuation can both increase the predicted noise level at receivers, this model can determine which should play a more important role due to the regularisation parameter. Additionally, this model can efficiently update the map every time step due to the use of pre-calculated partial maps. In this case study with 25498 sources and 3220 receivers updating took less than 0.5 s on an Intel(R) Xeon(R) CPU E5620 2.4 GHz.

In this study, the QSIDE model [10], [26] has been introduced from the start to improve noise prediction in shielded areas compared to common-practice in strategic noise mapping. Hence the corrections are expected to be smaller than those that could be expected if a standard strategic noise maps is used as a starting point. In this case study, the corrections ϵ and δ fall in the range [-5, 5] dB. The proposed model outperforms other approaches in its flexibility in the choice of measurement locations. Nevertheless, the uniqueness of the solution is improved if measurement stations are chosen in such a way that they characterise individual sources. Thus in an ideal situation one or more measurement stations should be close to each category of road traffic sources or industrial sources. As the measurements in Katendrecht were the result of a participatory process, the choice of measurement locations could not be optimised. The range of either source or propagation corrections can be controlled by μ and β. For example, in the center of an urban area, the traffic intensity is typically not available. Therefore, the source correction should be amplified (with bigger μ or smaller β) and the propagation correction should be depressed (with smaller μ and bigger β). By doing so, the dynamic patten of temporary sources or traffic can be captured. If the traffic intensity are known, such as some areas close to highways, the source correction should be depressed and the propagation correction should be amplified. In this study, combinations of different μ and β were compared. One of the best combinations is used in the case study. The proposed approach for interpolating percentile noise levels is a first order approximations. Better performance could be obtained if the local dynamics in traffic noise is accounted for explicitly, taking into account for example vehicle platoons formed by the operation of traffic lights [34, 19]. This would require more dense sensor networks - that are currently being deployed in new case studies - and a refined approach for source corrections. In the Katendrecht case study, neither traffic lights nor traffic jams are present at close proximity to the dwellings and hence these factors are not of importance and free traffic flow could be assumed. The validation only provided a general idea of the model, since the input information of the traffic is not sufficient. Some further validation work is necessary and some further modification of the model e.g. including more fitting parameters could improve the prediction.

Acknowledgement

The measurement data used in this work was obtained through a pilot study commissioned by DCMR Milieudienst Rijnmond, Rotterdam, carried out within the framework of the Smart Sound Monitoring (SSM) research valorisation project, supported by the Industrial Research Fund (IOF) of Ghent University (IOF Advanced Grant 201).

Appendix Analysis of L_{10} and L_{90}

A3.1 Adding different contributions to overall L_{10} and L_{90}

As introduced in section 4.2, the total sound pressure level at receivers is obtained as a sum of independent source categories and propagation paths. To calculate L_{10} or L_{90} of the sum of all contributions, the distribution of each of the individual contributions and their mutual correlations needs to be known. As this information is generally not available, a simplified methodology is proposed. For each contribution, it is either assumed that the sound is constant or that its levels are normally distributed and independent from all other contributions. From the look-up table, the traffic sound sources are considered as constant if the $|L_{10,m,n} - L_{eq,m,n}| < 1dB$ and $|L_{eq,m,n} - L_{90,m,n}| < 1dB$ where m is source category and n is propagation path category. For a constant sound, $L_{eq} = L_{10} = L_{90}$. When summing constant sounds, all percentile levels are simply equal to the energetic sum of all individual L_{Aeq}'s.

Another common situation is that one contribution can be considered as constant and the other one is fluctuating. In these situations, a good approximation for the percentile level of the total sound is obtained as:

$$L_x = \begin{cases} L_{eq,const} & \text{if} \quad \mathrm{L_{eq,const} \geq L_{x,fluctuating}} \\ L_{x,fluctuating} & \text{if} \quad \mathrm{L_{eq,const} < L_{x,fluctuating}} \end{cases} \tag{4.17}$$

where $L_{eq,const}$ is the equivalent level of the constant source and $L_{x,fluctuating}$ is the percentile level of the fluctuating source.

If two or more contributions are fluctuating, it is assumed that the sound intensity at the receiver position satisfies the normal distribution, then the relation between L_{10} and L_{eq} is: $10^{0.1L_{10}} - 10^{0.1L_{eq}} = 1.28\sigma$, where σ is the standard deviation of the normal distribution. Generally, a source (road) m propagating to a receiver by path n is:

$$10^{0.1L_{10,m,n}} - 10^{0.1L_{eq,m,n}} = 1.28\sigma_{m,n} \tag{4.18}$$

According to the properties of normal distribution, the total L_{10} and L_{90} are:

$$L_{10} = 10\log_{10}\left(\sum_m\sum_n 10^{0.1L_{eq,m,n}} + 1.28\sqrt{\sum_m\sum_n \sigma^2_{m,n}}\right) \tag{4.19}$$

$$L_{90} = 10\log_{10}\left(\sum_m\sum_n 10^{0.1L_{eq,m,n}} - 1.28\sqrt{\sum_m\sum_n \sigma^2_{m,n}}\right) \tag{4.20}$$

As a result, to calculate L_{10} and L_{90}, the following procedure is followed 1) group all contributions into two classes: "constant" and "fluctuating" 2) sum contributions within one class according to equation and (4.19) and (4.20) respectively; 3) calculate the overall L_{10} and L_{90} by equation (4.17).

A3.2 Calculation of $\frac{\partial}{\partial\epsilon_m^{t-1}}L_{10}$, $\frac{\partial}{\partial\epsilon_m^{t-1}}L_{90}$, $\frac{\partial}{\partial\delta_{m,n}^{t-1}}L_{10}$ and $\frac{\partial}{\partial\delta_{m,n}^{t-1}}L_{90}$

According to the formulation of L_{10} and L_{90} as well as equation (4.17), the derivative respect to ϵ_m^{t-1} and $\delta_{m,n}^{t-1}$ equals to zero for the source category m and propagation category n for which the contribution is eliminated by this equation. If the dominating contribution to L_{10} and L_{90} belongs to the "constant" class, the derivative becomes the derivative of L_{Aeq}, for which formulas have already been derived. If the dominating contribution belongs to the "fluctuating" class levels, according to equation (4.19, 4.20) the derivatives $\frac{\partial}{\partial\epsilon_m^{t-1}}L_{10}$ and $\frac{\partial}{\partial\delta_{m,n}^{t-1}}L_{90}$ become:

$$\frac{\partial}{\partial\epsilon_m^{t-1}}L_{10} = \frac{10}{\ln 10}\frac{\frac{\partial}{\partial\epsilon_m^{t-1}}\sum_m\sum_n 10^{0.1L_{eq,m,n}} + 1.28\frac{\partial}{\partial\delta_{m,n}^{t-1}}\sqrt{\sum_m\sum_n\sigma^2_{m,n}}}{\sum_m\sum_n 10^{0.1L_{eq,m,n}} + 1.28\sqrt{\sum_m\sum_n\sigma^2_{m,n}}} \tag{4.21}$$

Since $\sum_m\sum_n 10^{0.1L_{eq,m,n}}$ is actually $\sum_i^{N_s}\sum_j^{N_h}10^{0.1[L'_{W,f,i}(t)-A'_{f,i,j}(p,t)]}$ and according to equation (4.10):

$$\begin{aligned}&\frac{\partial}{\partial\epsilon_m^{t-1}}\sum_m\sum_n 10^{0.1L_{eq,m,n}} = \\ &\frac{\ln 10}{10}10^{0.1\epsilon_m^{t-1}}\sum_{n=1}^{N_n}10^{-0.1\delta_{m,n}^{t-1}}\sum_{j\in n}\sum_{i\in m}10^{0.1[L_{W,f,i}(t)-A_{f,i,j}(p,t)]}\end{aligned} \tag{4.22}$$

The second part in the nominator of equation (4.21) is $\frac{\partial}{\partial \epsilon_{m,n}^{t-1}} \sqrt{\sum_m \sum_n \sigma_{m,n}^2} = \frac{\sigma_{m,n}}{\sqrt{\sum_m \sum_n \sigma_{m,n}^2}} \left(\sum_n \frac{\partial}{\partial \epsilon_m^{t-1}} \sigma_{m,n} \right)$. For “diffraction” path $n = 2$ and “scattered” path $n = 3$, it will always be assumed that the contribution belongs to the “constant” group and thus these terms will never occur in the summation. Therefore $\sum_n \frac{\partial}{\partial \epsilon_m^{t-1}} \sigma_{m,n} \approx \frac{\partial}{\partial \epsilon_m^{t-1}} \sigma_{m,1}$. Substituting this approximation and equation (4.18) to equation (4.21)leads to:

$$\begin{aligned}
\frac{\partial}{\partial \epsilon_m^{t-1}} \sigma_{m,1} &= \frac{1}{1.28} \frac{\partial}{\partial \epsilon_m^{t-1}} \left[10^{0.1(L'_{eq,m,1} + \Delta_{10,m,1})} - 10^{0.1 L'_{eq,m,1}} \right] \\
&= \frac{1}{1.28} \frac{\partial}{\partial \epsilon_m^{t-1}} \Big\{ 10^{\epsilon_m^{t-1} - \delta_{m,1}^{t-1}} \Big[\sum_{i \in m} 10^{0.1(L_{W,f,i} - A_{f,i,1} + \Delta_{10,m,1})} \\
&\quad - \sum_{i \in m} 10^{0.1(L_{W,f,i} - A_{f,i,1})} \Big] \Big\} \\
&= \frac{\ln 10}{12.8} 10^{\epsilon_m^{t-1} - \delta_{m,1}^{t-1}} (10^{0.1 \Delta_{10,m,1}} - 1) \sum_{i \in m} 10^{0.1(L_{W,f,i} - A_{f,i,1})} \qquad (4.23)
\end{aligned}$$

where, $L_{eq,m,1}$ is the equivalent level of source category m by propagation path 1 (“2D” path) and $\Delta_{10,m,1}$ is the level difference obtained from the tabulated results of typical traffic situations as explained before. While deriving Eqs. (4.23), it is assumed that $\sigma_{m,1}$ is constant. This implies that the traffic intensity and speed are assumed constant and thus the difference between L_{10} and L_{eq} is constant. In other words, all inaccuracy is assumed to be related to the sound power emitted by each single vehicle.
Similarly, $\frac{\partial}{\partial \epsilon_m^{t-1}} L_{90}$ can also be resolved.

$$\frac{\partial}{\partial \epsilon_m^{t-1}} L_{90} = \frac{10}{\ln 10} \frac{\frac{\partial}{\partial \epsilon_m^{t-1}} \sum_m \sum_n 10^{0.1 L_{eq,m,n}} - 1.28 \frac{\sigma_{m,n}}{\sqrt{\sum_m \sum_n \sigma_{m,n}^2}} \frac{\partial}{\partial \epsilon_m^{t-1}} \sigma_{m,1}}{\sum_m \sum_n 10^{0.1 L_{eq,m,n}} - 1.28 \sqrt{\sum_m \sum_n \sigma_{m,n}^2}} \qquad (4.24)$$

The $\frac{\partial}{\partial \delta_{m,n}^{t-1}} L_{10}$ and $\frac{\partial}{\partial \delta_{m,n}^{t-1}} L_{90}$ can be solved as above

$$\frac{\partial}{\partial \delta_{m,n}^{t-1}} L_{10} = \frac{10}{\ln 10} \frac{\frac{\partial}{\partial \delta_{m,n}^{t-1}} \sum_m \sum_n 10^{0.1 L_{eq,m,n}} + 1.28 \frac{\sigma_{m,n}}{\sqrt{\sum_m \sum_n \sigma_{m,n}^2}} \frac{\partial}{\partial \delta_m^{t-1}} \sigma_{m,1}}{\sum_m \sum_n 10^{0.1 L_{eq,m,n}} + 1.28 \sqrt{\sum_m \sum_n \sigma_{m,n}^2}} \qquad (4.25)$$

$$\frac{\partial}{\partial \delta_{m,n}^{t-1}} L_{90} = \frac{10}{\ln 10} \frac{\frac{\partial}{\partial \delta_{m,n}^{t-1}} \sum_m \sum_n 10^{0.1 L_{eq,m,n}} - 1.28 \frac{\sigma_{m,n}}{\sqrt{\sum_m \sum_n \sigma_{m,n}^2}} \frac{\partial}{\partial \delta_m^{t-1}} \sigma_{m,1}}{\sum_m \sum_n 10^{0.1 L_{eq,m,n}} - 1.28 \sqrt{\sum_m \sum_n \sigma_{m,n}^2}} \qquad (4.26)$$

where

$$\frac{\partial}{\partial \delta_{m,n}^{t-1}} \sum_m \sum_n 10^{0.1 L_{eq,m,n}} = -10^{0.1\epsilon_m^{t-1}} 10^{-0.1\delta_{m,n}^{t-1}} \sum_{j \in n} \sum_{i \in m} 10^{0.1[L_{W,f,i}(t) - A_{f,i,j}(p,t)]}$$

$$\frac{\partial}{\partial \delta_{m,n}^{t-1}} \sigma_{m,1} =$$

$$\begin{cases} 0 & \text{if} \quad \mathrm{n} \neq 1 \\ -\frac{\ln 10}{12.8} 10^{\delta_{m,j}^{t-1} - \delta_{m,1}^{t-1}} (10^{0.1\Delta_{10,m,1}} - 1) \sum_{N_{m-1}}^{N_m} 10^{0.1(L_{W,f,i} - A_{f,i,1})} & \text{if} \quad \mathrm{n} = 1 \end{cases} \tag{4.27}$$

A3.3 Comparison between source correction and source & propagation correction

As mentioned in the previous sections, it is possible to update a noise map by only correcting sources. As this is the most common approach in map based interpolation today, the impact of including also corrections on propagation is investigated in more detail in this appendix. Figures (4.17) to (4.19) show the improvements by updating both sources and propagations compared to only updating the sources. For this purpose, the proposed model is run twice on the same measurement period, once allowing ϵ and δ to adapt, once keeping $\delta = 0$. This results in an improvement with respect to measurements of $\Delta_{\epsilon,\delta}$ and Δ_ϵ respectively. The distribution for all time intervals during 45 days is shown as a function of $\Delta_{\epsilon,\delta} - \Delta_\epsilon$ in figure (4.17). The positive values mean better predicting obtained by updating both sources and propagations. The negative values mean the opposite.

Figure (4.17) shows that correcting the sources and the propagations get better prediction of L_{Aeq} around 80% percent in average. Most of the improvements fall in the range $[0, 1.2]$ dB. For L_{10}, the propagation correction does not affect the prediction considerably, as shown in figure (4.18). This is because sound peaks are assumed to be caused by the closest road and the direct propagation path that is least likely to be incorrect. Therefore only modifying the source can achieve similar improvement compared with correcting both sources and propagation paths. The propagation correction improves the L_{90} prediction considerably. More than 90% in average are better if both corrections are applied. The reason could be that L_{90} is governed by the overall noise environment and not only by the traffic on the closest road, which is often a minor road in the residential area under study. The contribution of the distant sources to L_{90} play more important role and propagation corrections, such as diffraction and turbulent scattering may improve these.

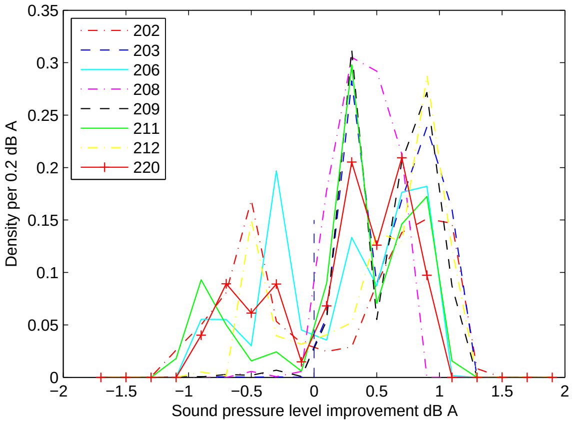

(a) Density function

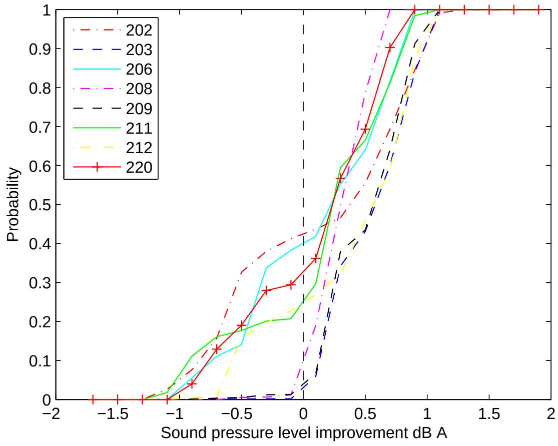

(b) Cumulative probability function

Figure 4.17: Comparison of L_{Aeq} between updating only sources and sources & propagations

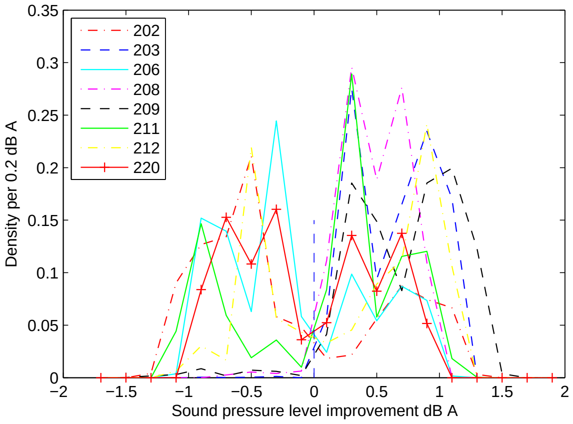

(a) Density function

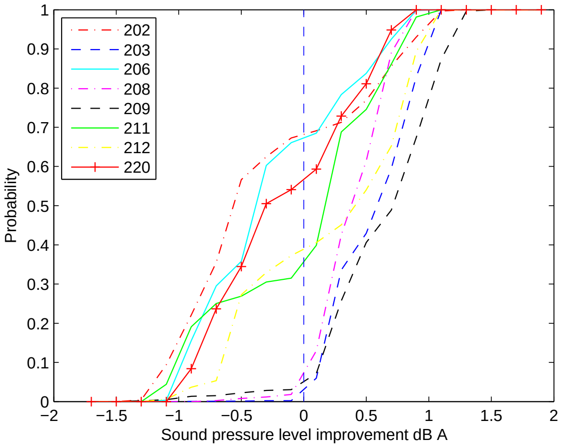

(b) Cumulative probability function

Figure 4.18: Comparison of L_{10} between updating only sources and sources & propagations

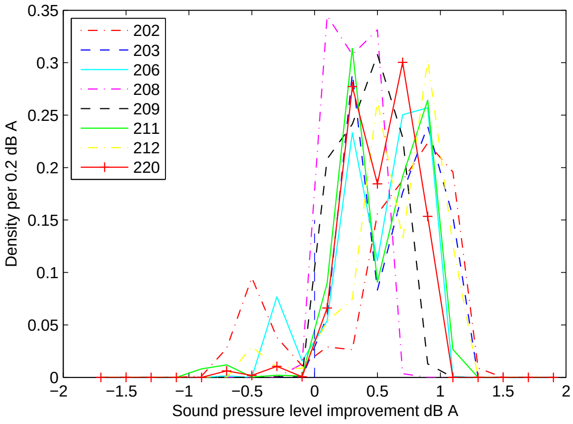

(a) Density function

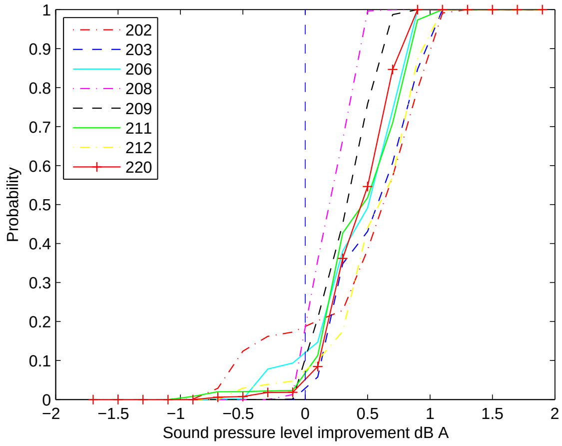

(b) Cumulative probability function

Figure 4.19: Comparison of L_{90} *between updating only sources and sources & propagations*

References

[1] M. Ángeles Martín, Ana I. Tarrero, María Machimbarrena, Julio González, and Valentín González De Garibay. *A methodology to study noise annoyance and to perform Action Plans follow up using as input an existing survey and noise map: Application to the city of Málaga (Spain)*. Applied Acoustics, 72(8):495–504, July 2011.

[2] Paulo Henrique Trombetta Zannin and David Queiroz De SantAna. *Noise mapping at different stages of a freeway redevelopment project A case study in Brazil*. Applied Acoustics, 72(8):479–486, July 2011.

[3] Joon Hee Ko, Seo Il Chang, and Byung Chan Lee. *Noise impact assessment by utilizing noise map and GIS: A case study in the city of Chungju, Republic of Korea*. Applied Acoustics, 72(8):544–550, July 2011.

[4] Kang Ting Tsai, Min Der Lin, and Yen Hua Chen. *Noise mapping in urban environments: A Taiwan study*. Applied Acoustics, 70(7):964–972, 2009.

[5] Bo Wang and Jian Kang. *Effects of urban morphology on the traffic noise distribution through noise mapping: A comparative study between UK and China*. Applied Acoustics, 72(8):556–568, July 2011.

[6] Piotr Mioduszewski, Jerzy a. Ejsmont, Jan Grabowski, and Daniel Karpiski. *Noise map validation by continuous noise monitoring*. Applied Acoustics, 72(8):582–589, July 2011.

[7] J M Barrigón Morillas and C Prieto Gajardo. *Uncertainty evaluation of continuous noise sampling*. 75:27–36, 2014.

[8] Mikael Ögren and Erik Salomons. *QSIDE: http://www.qside.eu*, October 2010.

[9] Martin Schiff, Maarten Hornikx, and Jens Forssén. *Excess attenuation for sound propagation over an urban canyon*. Applied Acoustics, 71(6):510–517, June 2010.

[10] W. Wei, D. Botteldooren, T. Van Renterghem, M. Hornikx, J. Forssén, E. Salomons, and M. Ögren. *Urban Background Noise Mapping: The General Model*. Acta Acust. United Ac, 100(6):1098–1111, 2014.

[11] Timothy Van Renterghem and Dick Botteldooren. *In-situ measurements of sound propagating over extensive green roofs*. Building and Environment, 46(3):729–738, 2011.

[12] Timothy Van Renterghem and Dick Botteldooren. *The importance of roof shape for road traffic noise shielding in the urban environment*. J. Sound Vib., 329(9):1422–1434, 2010.

[13] M. Arana, R. San Martin, M. L. San Martin, and E. Aramendia. *Strategic noise map of a major road carried out with two environmental prediction software packages*. Environmental monitoring and assessment, 163(1):503–513, 2010.

[14] Miguel Arana, Ricardo San Martín, Iñaki Nagore, and David Pérez. *What precision in the Digital Terrain Model is required for noise mapping?* Applied Acoustics, 72(8):522–526, July 2011.

[15] Barbara Griefahn. *Environmental noise and sleep. ReviewNeed for further research*. Applied Acoustics, 32(4):255–268, January 1991.

[16] Gabor Gereb. *Real-time updating of noise maps by source-selective noise monitoring*. NOISE CONTROL ENGINEERING JOURNAL, 61(2):228–239, March 2013.

[17] Maciej Szczodrak, Józef Kotus, Boena Kostek, and Andrzej Czyewski. *Creating Dynamic Maps of Noise Threat Using PL-Grid Infrastructure*. Archives of Acoustics, 38(2):235–242, January 2013.

[18] Dae Seung Cho, Jin Hyeong Kim, and Douglas Manvell. *Noise mapping using measured noise and GPS data*. Applied Acoustics, 68(9):1054–1061, September 2007.

[19] A. Can, L. Leclercq, J. Lelong, and D. Botteldooren. *Traffic noise spectrum analysis: Dynamic modeling vs. experimental observations*. Applied Acoustics, 71(8):764–770, August 2010.

[20] Bert De Coensel, Dick Botteldooren, Filip Vanhove, and Steven Logghe. *Microsimulation Based Corrections on the Road Traffic Noise Emission Near Intersections*. Acta Acust. Acust., 93(2):241–252, 2007.

[21] Ma Xia-lin and Cai Ming. *Rendering of Dynamic Road Traffic Noise Map based on Paramics*. Procedia - Social and Behavioral Sciences, 96(Cictp):1460–1468, November 2013.

[22] Arnaud Can, Timothy Van Renterghem, Michael Rademaker, Samuel Dauwe, Pieter Thomas, Bernard De Baets, and Dick Botteldooren. *Sampling approaches to predict urban street noise levels using fixed and temporary microphones*. Journal of environmental monitoring : JEM, 13(10):2710–9, October 2011.

[23] Bert De Coensel, Tom De Muer, Isaak Yperman, and Dick Botteldooren. *The influence of traffic flow dynamics on urban soundscapes*. Applied Acoustics, 66(2):175–194, 2005.

[24] Bert De Coensel, Filip Vanhove, Steven Logghe, Isabel Wilmink, and Dick Botteldooren. *Noise emission corrections at intersections based on microscopic traffic simulation*. In Proceedings of Euronoise 2006, 2006.

[25] Bert De Coensel, Dick Botteldooren, Tom De Muer, Birgitta Berglund, Mats E. Nilsson, and Peter Lercher. *A model for the perception of environmental sound based on notice-events*. J. Acoust. Soc. Am., 126(2):656–665, 2009.

[26] Jens Forssén, Maarten Hornikx, T. Van Renterghem, W. Wei, D. Botteldooren, and M. Ögren. *A Model of Sound Scattering by Atmospheric Turbulence for Use in Noise Mapping Calculations*. Acta Acust. United Ac, 100(5):810–815, 2014.

[27] Bert De Coensel and Dick Botteldooren. *Smart sound monitoring for sound event detection and characterization.* In Proc. of the 43rd International Congress and Exposition on Noise Control Engineering (Internoise 2014), Melbourne, Australia, 2014, 2014.

[28] George F Jenks. *The data model concept in statistical mapping*. International yearbook of cartography, 7(1):186–190, 1967.

[29] Timothy Van Renterghem, Pieter Thomas, Frederico Dominguez, Samuel Dauwe, Abdellah Touhafi, Bart Dhoedt, and Dick Botteldooren. *On the ability of consumer electronics microphones for environmental noise monitoring*. Journal of environmental monitoring: JEM, 13(3):544–552, March 2011. PMID: 21157618.

[30] Timothy Van Renterghem, Pieter Thomas, Dick Botteldooren, Samuel Dauwe, Bart Dhoedt, F Dominguez, and A Touhafi. *The use of cheap microphones in extensive outdoor noise monitoring networks*. In Proceedings of The Institute OF Acoustics, volume 32, pages 374–377. Institute of Acoustics, 2010.

[31] Bram De Greve, Tom De Muer, and Dick Botteldooren. *Outdoor beam tracing over undulating terrain*. In Proceedings of Forum Acusticum 2005, pages 1011–1016, 2005.

[32] G. Memoli, M. Paviotti, S. Kephalopoulos, and G. Licitra. *Testing the acoustical corrections for reflections on a façade*. Appl. Acoust., 69(6):479 – 495, 2008.

[33] Siu Hong Tang and Kai Ming Li. *The prediction of façade effects from a point source above an impedance ground*. The Journal of the Acoustical Society of America, 110(1):278–288, 2001.

[34] Arnaud Can, Ludovic Leclercq, and Joël Lelong. *Dynamic estimation of urban traffic noise: Influence of traffic and noise source representations*. Applied Acoustics, 69(10):858–867, October 2008.

5

Conclusions and future work

5.1 Conclusions

This research work is inspired by the underestimation of sound pressure levels at shielded urban locations commonly observed in strategic noise map and the bonus of the presence of a quiet side with relation to the perception of environmental noise. With the proposed urban background model (QSIDE model), better predictions at shielded locations were achieved and this model was also used as a propagation category to reduce the degrees of freedom in a dynamic mapping technique.

Previous commonly used engineering models for noise mapping at shielded locations either suffered from lack of accuracy such as ISO9613-2 or limited computational efficiency such as NORD2000. The QSIDE model emerged to fill the gap between these two. Achieving a good prediction for diffraction over roof tops in a canyon often requires more than 10 reflections, which leads to extremely long CPU time even with the simple algorithm mentioned in ISO9613-2. On the other hand, the QSIDE model handles the sum of reflections from 1 to infinity into an explicit Hurwitz-Lerch transcendent due to the simplification of the diffraction function over a thick barrier. Both FDTD simulations and theoretical solutions showed that the simplified diffraction function has a good accuracy. Therefore, the QSIDE model can improve the predictions without considerably increasing the calculating time, which can potentially provide a guide for predicting models in the future.

Including the effect of roughness and diffusion is another advantage of the QSIDE model. After obtaining the basic form of the QSIDE model based on a flat façade surface, a few parameters were fitted from a large number of FDTD simulations to consider the roughness of the façades. These parameters represented the average roughness of a canyon in a city. In case the diffraction over the roof top in the strategic noise maps is removed, the QSIDE correction could be directly applied to the strategic noise map. Even though the strategic noise map included one diffraction over the roof top, adding the QSIDE model to the strategic noise map could still be a first estimation. A case study in Gent, Belgium showed the aforementioned concept.

The QSIDE model is still a 2.5 D approach where 2D tracing is combined with propagation in vertical cross sections. The total contribution is the energetic sum of all the cross sections which is the same as the latest noise mapping algorithm. To predict propagation over different roof shapes or over multiple city canyons, the QSIDE model was generalized. The generalized model can deal with a few typical canyon configurations such as canyons formed by buildings of both the same height and different height. The generalized form was also validated by FDTD simulations. Additionally, the generalized QSIDE model depends only on the vertical heights of buildings leading to a very stable calculation methodology for the background noise level. The required input arguments, such as the geometrical information of the section planes, can be provided directly by the 2.5 D noise mapping approach.

As shown in some studies, the turbulent scattering sometimes dominate the contribution to a receiver specifically for high frequencies. The total contribution would then be the sum of the QSIDE model correction and the turbulent correction.

Based on the developed background model, a dynamic noise mapping method for interpolating noise maps between measurement stations is explored by implementing the Least-Mean Squares method (LMS). Moreover, compared to only updating source powers, the LMS fitting allowed to correct both the sources and the propagation paths. By grouping the sources and propagation paths in a few categories, the number of degrees of freedom in the system to be solved reduced to a very small number and the interpolation procedure could be ran in a very short time interval. This dynamic noise mapping technique allowed updating not only the L_{eq} but also the percentile levels which is very useful for soundscape or noise perception studies.

5.2 Suggestions for future work

The advantage of the QSIDE model and the dynamic mapping strategy were highlighted in the dissertation. The following are some suggestions for future work.

The QSIDE model is validated as a nice tool to calculate the background noise level. However, to become part of the future guidelines (hopefully), additional validations and implementations are also needed. The model has already been checked by a researcher from Chalmers University with "SoundPlan" software by designating different reflections and absorption coefficients of the façades. To run a few calculating campaigns would also be very helpful to further validation of the model.

The generalized QSIDE model had offered options to handle non-flat roof shapes. However, it is difficult for the current 2.5 D approach to provide roof shape information in the vertical dimension. How to integrate the information of the vertical dimension will be a long term research topic. The effect of the turbulent scattering of the QSIDE model is strongly related to the meteorological condition. Detailed meteorological measurements are still not available now in many cities. In the future, finding a way to interpolate the data between different weather stations could be one option to get the turbulent strength and increasing the density of the weather stations could be another option.

The street canyon may not be the same between newly developed regions having a lot of skyscrapers and historically grown cities having clusters of low buildings. Situations will be quite different when implementing the QSIDE model in these regions.

The QSIDE model focused on the reflections over building roof, however, the multiple reflections could also affect the receivers inside the canyon. To find a simple solution for reflections inside the canyon could also be an interesting research topic in the future.

Although the dynamic mapping method was developed mainly based on road traffic sources, other sources are open to add as separate categories. Two special sources, a church bell and and a open party, have been checked in Gent Belgium by this method. Different regions may have varied special sources which could be the major reasons to cause annoyance and sleep disturbance. The dynamic noise mapping method could be an option to quantify these effects. Adding extra sources would increase the number of degrees of freedom. In this research, the number of measurement positions is 8, so it is difficult to include so many local sources. Luckily, a dense measurement network with around 30 measurement stations is deploying in Paris now. It would be possible to implement the method to do further study about the dynamic pattern to perception etc.

The method used in the dynamic noise mapping offers a pilot study to interpolate L_{eq} and L_{10} and L_{90} between measurements. Other acoustic indicators or even sound events can also be interpolated similarly. In the future, the effect of meteorological changes and number of intermediate buildings could possibly be integrated into the fitting system as a separate correction term. Additionally, the detailed information of vehicles such as speed and traffic flow could also be integrated into the fitting system. Indeed, the increase of DOF would call for a dense measurement network.

A

Appendix

This appendix contains the comparison of the road traffic source power model proposed by the HARMONOISE project and the CNOSSOS-EU project and evaluates the diffraction functions of ISO9613-2, HARMONOISE, CNOSSOS-EU, NMPB2008, NORD2000, QSIDE and Pierce. The background noise model presented in this work is based on a large number of full-wave simulations performed with the finite-difference time-domain technique. The basic geometry and parameters used for the latter are described in the second part of this Appendix.

A.1 Comparison of source model between CNOSSOS-EU and HARMONOISE

In the HARMONOISE road traffic source power model, the vehicles are divided into 3 main categories and other 2 special categories according to their engine type and number of axles. A single vehicle is simplified to two point sources. One is 0.01 m above the ground and the other one is positioned either 0.3 m (for a light vehicle) or 0.75 m (for a heavy vehicle) above the road surface. These two points are used to describe the rolling and propulsion noise, respectively. The emission strengths of the rolling and propulsion noise depend on the source category and the speed of the vehicle, as shown in the following equations:

$$L_{WR} = A_R(f) + B_R(f)\log(\frac{v}{v_{ref}}) \tag{A.1}$$

$$L_{WP} = A_P(f) + B_P(f) \times \frac{v - v_{ref}}{v_{ref}} \tag{A.2}$$

where L_{WR} is the emission power level of the rolling noise; L_{WP} is the emission power level of the propulsion noise; $A_R(f)$ and $B_R(f)$ are coefficients to calculate the emission of rolling noise; $A_P(f)$ and $B_P(f)$ are coefficients to calculate the emission propulsion noise; v is the speed of the vehicle and v_{ref} is the reference speed which equals 70 km/h.

The values of coefficients $A_R(f)$, $B_R(f)$, $A_P(f)$ and $B_P(f)$ depends on the type of categories and frequency f. The frequency f in HARMONOISE can be in 1/3 octave bands.

CNOSSOS-EU is a recently developed noise assessment method for strategic noise mapping, which is currently recommended to be used in the EU member states. This model has a similar structure as HARMONOISE. However, the difference in the road traffic source emission model are significant. In CNOSSOS-EU, a single vehicle is now simplified as a single point source at the height of 0.05 m above the road surface instead of two point sources as mentioned above. The emission calculation of the rolling noise part and propulsion noise part are similar as HARMONOISE:

$$L_{WR} = A_R(f) + B_R(f)\log(\frac{v}{v_{ref}}) + \Delta L_{WR}(v) \tag{A.3}$$

$$L_{WP} = A_P(f) + B_P(f) \times \frac{v - v_{ref}}{v_{ref}} + \Delta L_{WP}(v) \tag{A.4}$$

where $\Delta L_{WR}(v)$ is an extra correction for special roads and vehicle conditions and $\Delta L_{WP}(v)$ is an extra correction for the specific driving conditions or actual regional conditions. The total emission power level should then be the energetic sum of the two parts $L_W = 10\log_{10}(10^{L_{WR}/10} + 10^{L_{WP}/10})$.

While 1/3 octave bands were used in HARMONOISE, the coefficients to calculate the rolling and propulsion noise are only available in octave bands in CNOSSOS-EU. As a newer model, the CNOSSOS-EU may include some new measurement data for some new vehicles . Two types of comparisons will be presented. 1) Comparison of total rolling and total propulsion noise under the reference conditions (CNOSSOS-EU):

- a constant vehicle speed
- a flat road

- an air temperature 20^oC
- a virtual reference road surface, consisting of an average of dense asphalt concrete 0/11 and stone mastic asphalt 0/11, between 2 and 7 years old and in a representative maintenance condition
- a dry road surface
- no studded tyres

Figure (A.1) shows the total emission power level caused by the rolling noise. The rolling noise power level in the CNOSSOS-EU model is less than the HARMONOISE model for category 1, passenger cars. For the heavy vehicles, the two model have very similar predictions. Figure (A.2) is the total emission power level caused by the propulsion noise. The predictions of the CNOSSOS-EU model is considerably lower than the HARMONOISE model.
From figure (A.3) to figure (A.14) are comparison of these coefficients. For the coefficients in the HARMONOISE model, the coefficients values of all underlying 1/3 octave bands are energetically summed to produce every octave bands.

A.2 Comparison of diffraction functions among different models

A concise comparison of attenuation caused by diffraction between different models is listed below. The additional attenuation caused by sound diffracting over an obstacle of ISO9613-2 and CNOSSOS-EU are very similar. For ISO9613-2 the barrier attenuation D_z in a downward refraction condition is:

$$D_z = 10\log_{10}[3 + \frac{C_2C_3}{\lambda}zK_{met}] \tag{A.5}$$

where, C_2 = 20 for including the ground effect; C_2 = 40 for excluding the ground effect; C_3 = 1 for single diffraction, otherwise $C_3 = \frac{1+(5\lambda/e)^2}{1/3+(5\lambda/e)^2}$, e is the width of a double barrier, λ is the wavelength; z is the difference between the diffracted and direct path; K_{met} is correction for meteorological condition. ISO9613-2 suggests that D_z should be no greater than 20 dB and 25 dB for single and double diffraction respectively in any octave band. Only the pure diffraction formula without ground reflection is discussed in the following text. After ISO9613, numerical methods usually offer both downward and non-refracting-atmosphere conditions for formulas of diffraction. In the following parts only the propagation formulas in non-refracting-atmosphere conditions are discussed. The CNOSSOS-EU and NMPB2008 use a similar method to calculate D_z in non-refracting-atmosphere conditions:

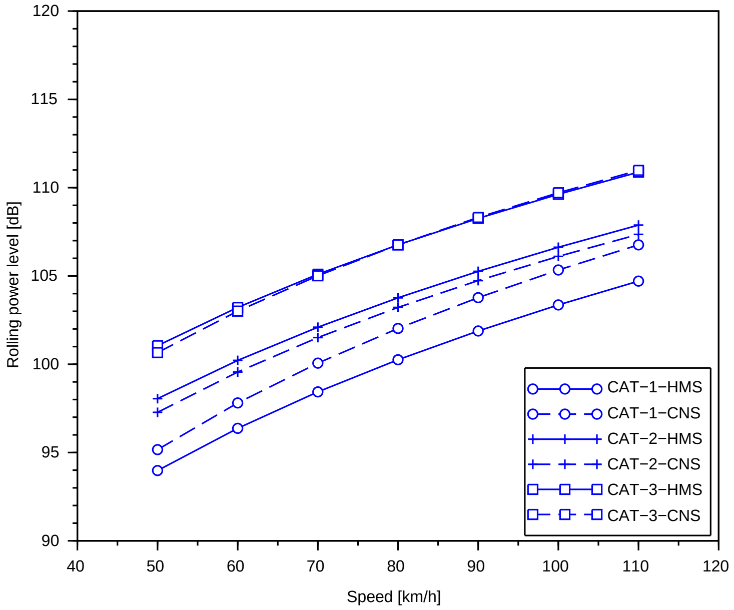

Figure A.1: Rolling noise of the default condition where "CAT" is the category; "CNS" is CNOSSOS-EU; "HMS" is Harmonoise. category $m = 1$ *indicates the "light vehicles"; category* $m = 2$ *indicates medium heavy vehicles; category* $m = 3$ *indicates the heavy vehicles.*

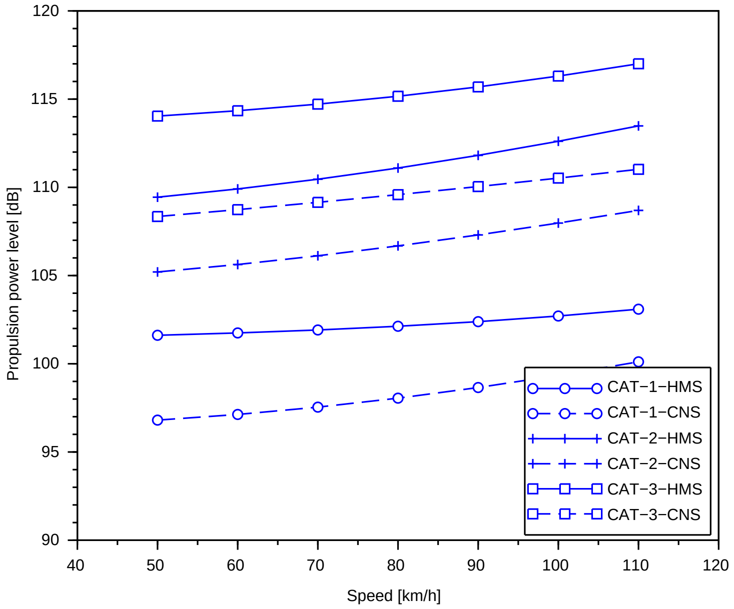

Figure A.2: Propulsion noise of the default condition.

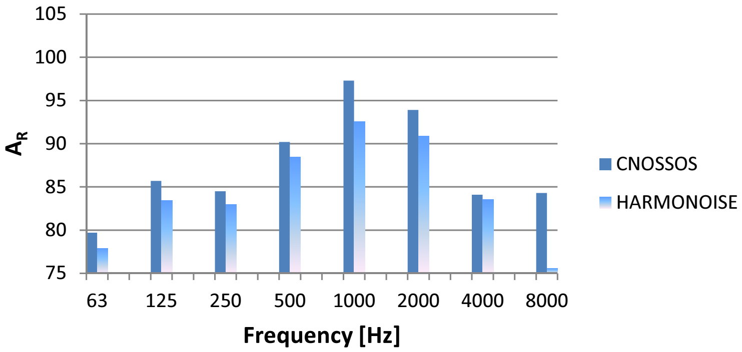

Figure A.3: A_R of category m = 1, light vehicles.

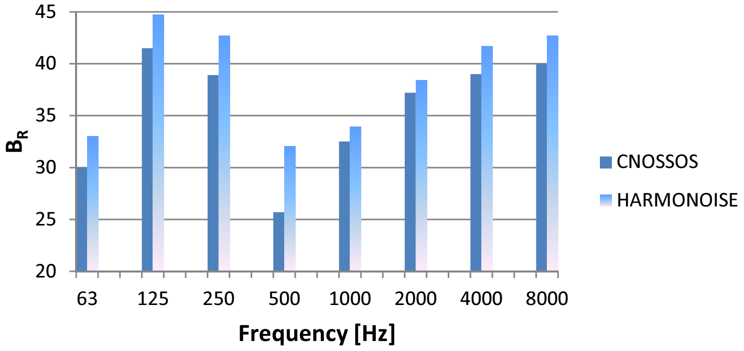

Figure A.4: B_R *of category* $m = 1$.

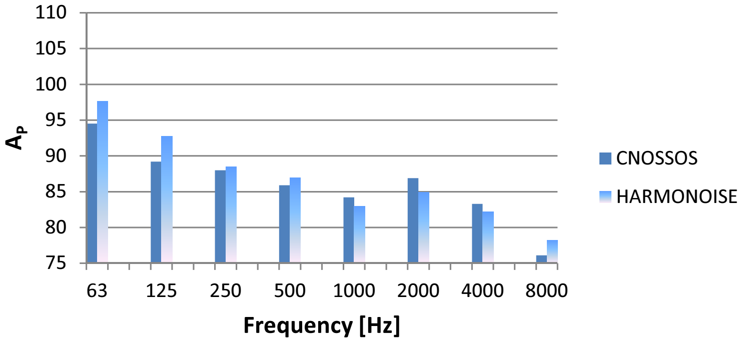

Figure A.5: A_P *of category* $m = 1$.

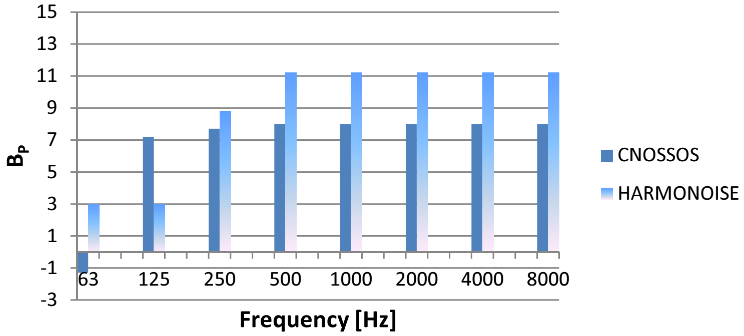

Figure A.6: B_P *of category* $m = 1$.

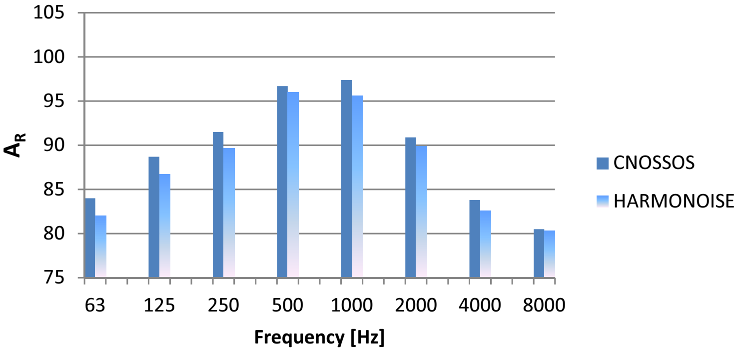

Figure A.7: A_R *of category* $m = 2$*, medium heavy vehicles.*

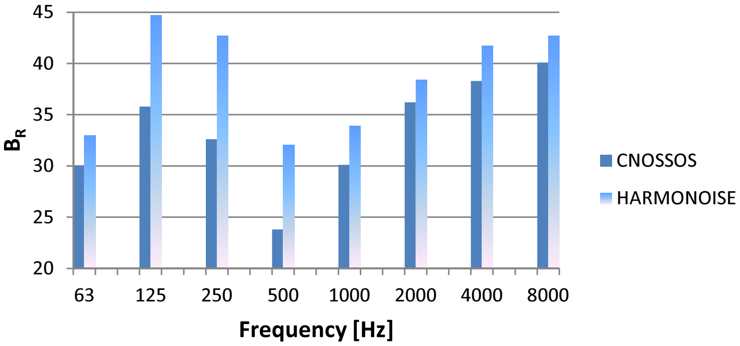

Figure A.8: B_R *of category* $m = 2$.

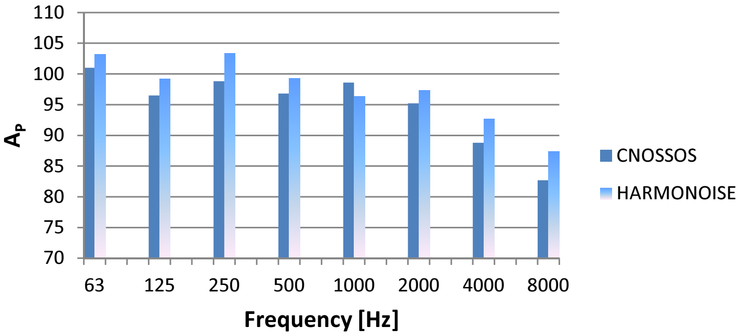

Figure A.9: A_P *of category* $m = 2$.

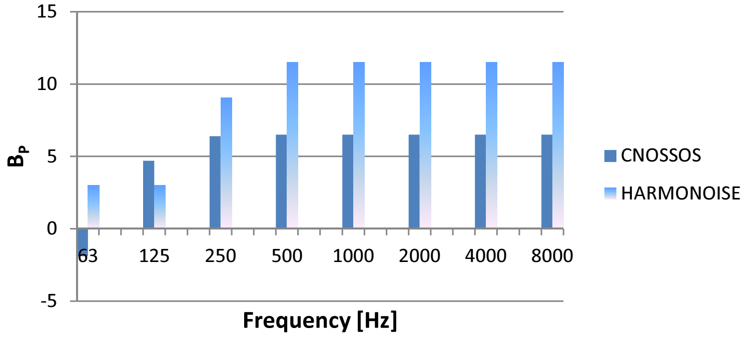

Figure A.10: B_P *of category* $m = 2$.

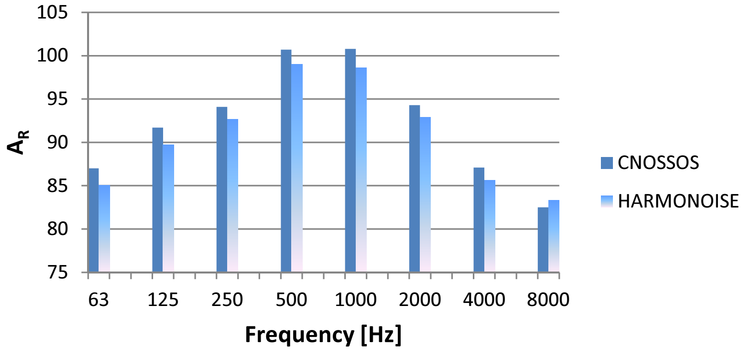

Figure A.11: A_R *of category* $m = 3$*, heavy vehicles.*

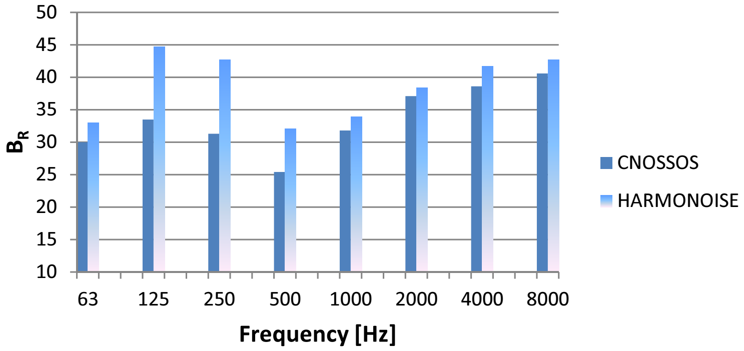

Figure A.12: B_R *of category* $m = 3$.

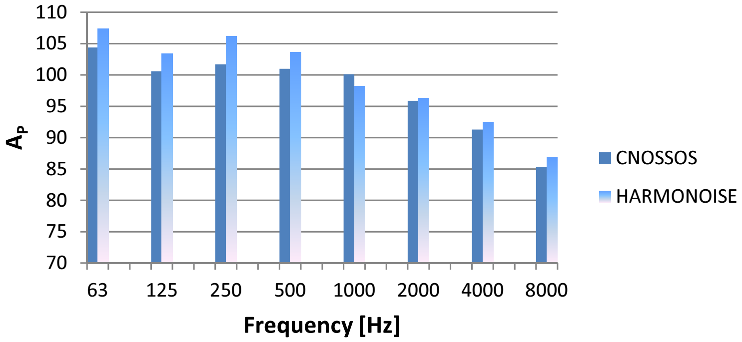

Figure A.13: A_P *of category* $m = 3$.

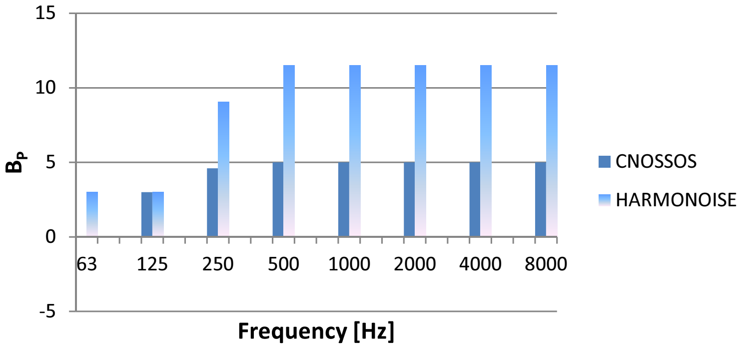

Figure A.14: B_P *of category* $m = 3$.

$$D_z = 10C_h \log_{10}[3 + \frac{40C_3}{\lambda}\delta] \tag{A.6}$$

where $C_h = \min\{\frac{f_m h_0}{250}, 1\}$, f_m is the central frequency of an octave band, h_0 is the maximum height from the barrier edge to the equivalent ground, δ is the length difference between the diffraction path and the direct path. CNOSSOS-EU suggests a 25 dB limit for D_z. HARMONOISE uses Deygout's diffraction model which is a step-wise function.

$$D_z(N_F) = \begin{cases} 0 & \text{for } N_F < -0.25 \\ -6 + 12\sqrt{-N_F} & \text{for } -0.25 \le N_F \le 0 \\ -6 - 12\sqrt{N_F} & \text{for } 0 \le N_F \le 0.25 \\ -8 - 8\sqrt{N_F} & \text{for } 0.25 \le N_F \le 1 \\ -16 - 10\log N_F & \text{for } N_F > 1 \end{cases} \tag{A.7}$$

with Fresnel number $N_F = 2\delta/\lambda$, where δ is the difference between diffracted path and the direct path.

The diffraction function in the NORD2000 is fitted by a 12 order polynomial series as:

$$A_D(X) = sign(X)[f(|X|) - j\, g(|X|)] \tag{A.8}$$

where $f(x) = \sum_{n=0}^{12} a_n x^n$, $g(x) = \sum_{n=0}^{12} b_n x^n$

Based on the above equation, the attenuation of NORD2000 for a double diffraction is:

$$D_z = -10\log_{10}\left\{[f(|X_S|)^2 + g(|X_S|)^2][f(|X_R|)^2 + g(|X_R|)^2]\right\} \tag{A.9}$$

where X_S is parameter related to the source side which can be found in NORD2000 report; X_R is parameter related to the receiver side.

The diffraction model in ISO9613-2 or CNOSSOS-EU leads to considerable differences compared to full-wave reference simulations in the case of thick barriers corresponding to the dimensions of a house or building. The step-wise function of HARMONOISE is highly above the simulation curve in high frequencies as shown in figure (A.16).The new model to calculate the diffraction over a thick barrier is presented in this dissertation as:

$$A_D = j\left(\frac{0.37}{0.37 + BX_{S+}}\frac{0.37}{0.37 + X_{R+}}\right) \tag{A.10}$$

where $B = \sqrt{wL/[(w + r_S)(w + r_r)]}$ is a scalar multiplied to the smaller one of X_{S+} and X_{R+}. Here, $X_{S+} < X_{R+}$ is assumed. X_{S+} and X_{R+} are geometrical related parameters which will be explained in detail in the following chapters. We

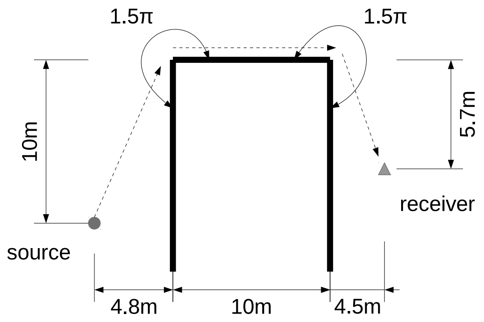

Figure A.15: Configuration of the comparison.

call this model as “QSIDE” model. The corresponding attenuation of a double diffraction is:

$$D_z = -10\log_{10}\left[\left(\frac{0.37}{0.37 + BX_{S+}}\right)^2\left(\frac{0.37}{0.37 + X_{R+}}\right)^2\right] \tag{A.11}$$

Figure (A.16) shows a comparison between the aforementioned methods for a typical building configuration in urban situations. The configuration is shown in figure (A.15)

Results of “Pierce”, “NORD2000” and “QSIDE” are very close to the “FDTD” simulations. Others strongly deviate from the reference simulations. Although “Pierce” method is slightly more accurate, it requires much longer calculating time than the “QSIDE” method. A comparison of the computational cost between these models is shown in chapter 3.

A.3 Configurations of FDTD simulations

In this research, the canyon-to-canyon propagation approach was applied. Therefore, a lot of typical canyon geometries were simulated. Then, the engineering model was tuned based on these simulations. These simulations cover a wide range of building widths, canyon widths and building heights, as well as different source and receiver positions. The façades are modelled with different protrusions and regressions to simulate the diffusion of soudn by surface irregularities. The normalized impedance of windows and brick walls were chosen to be $Z_n = 77$ and $Z_n = 10$ respectively. The effect of air absorption is added to the simulated impulse response afterwards.

The cell size used in the FDTD simulation is smaller than 2 cm (most of them are 2 cm and others are 1 cm) which is suitable for simulations frequency higher than 1500 Hz. Perfectly matched layers (PML) were assigned in the outer boundaries as

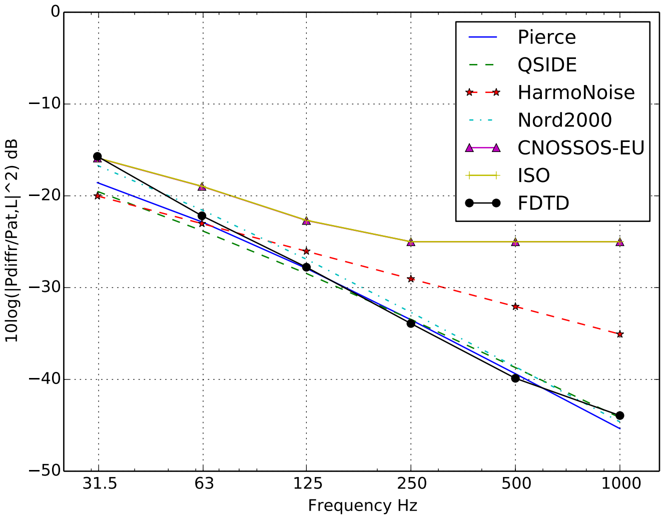

Figure A.16: Comparison of the diffraction term in different engineering methods for a typical urban setting. Source to barrier façades 4.8 m; source to barrier top 10 m; receiver to barrier façades 4.5 m; receiver to barrier top 5.7 m; rigid barrier with external angle 1.5π (the angle from façade to the barrier top).

a perfect absorbing boundary condition with the thickness 40 times cell size . The distance from the building top to the closest boundary of the PML is greater than 12 m, which is approximately 3 times the wave length of 80 Hz sound. Because the 3 D FDTD simulations would take too much time to run over many common urban geometrical configurations, the simulations in this work are only 2 D cases. The time step, governed by the Courant number stability criterion, were 0.00002 s and 0.00004 s for the 1 cm cell grid and 2 cm cell grid, respectively. The number of time steps is determined by the geometrical size so that simulation times were sufficiently long so convergence was reached for the sound pressure levels. The source was a Gaussian pulse with the central frequency 850 Hz. The main goal of these FDTD simulations is to correct for the roughness and diffusion caused by non-flat façades inside a canyon, therefore, the effect of wind was not included. The velocity v at discrete time t and position x is in a simple form:

$$v_{x(x+0.5)}^{t+0.5} = v_{x(x+0.5)}^{t-0.5} - \frac{dt}{\rho_0}\left[\frac{p_{(x+1)}^{t} - p^{t}}{dt}\right] \tag{A.12}$$

The sound pressure p at the cell center is:

$$p^{t+1} = p^{t} - dt\, c^2 \rho_0 \sum_{x} \frac{v_{x(x+0.5)}^{t+0.5} - v_{x(x-0.5)}^{t+0.5}}{dx} \tag{A.13}$$

where x is the group of the spacial indices (i, j, k); $x(x+0.5)$ indicates the position x at the positive direction of a cell surface; $x(x - 0.5)$ indicates the position x at the negative direction of a cell surface; the sum over x runs over all the (i, j, k) indices; $t + 0.5$ indicates an intermediate time; c is the speed of sound; ρ_0 is the density of ambient air. The solutions of the simulations follow the above form of pressure and velocity. A typical sound pressure p as a function of t in the simulations is depicted in figure (A.17):

To formulate the background noise model, 566 FDTD simulations were considered. Different parameters H_s, H_i, H_r, W_s, W_i and W_r (which is illustrated in figure 2.2) are plotted in pie charts from figure (A.18) to figure (A.19).

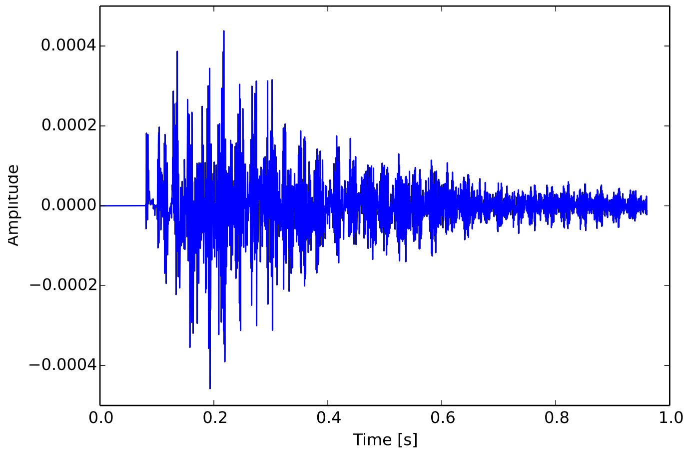

Figure A.17: An impulse response of a typical FDTD simulation case. In this plot, the time step is 0.00002 s

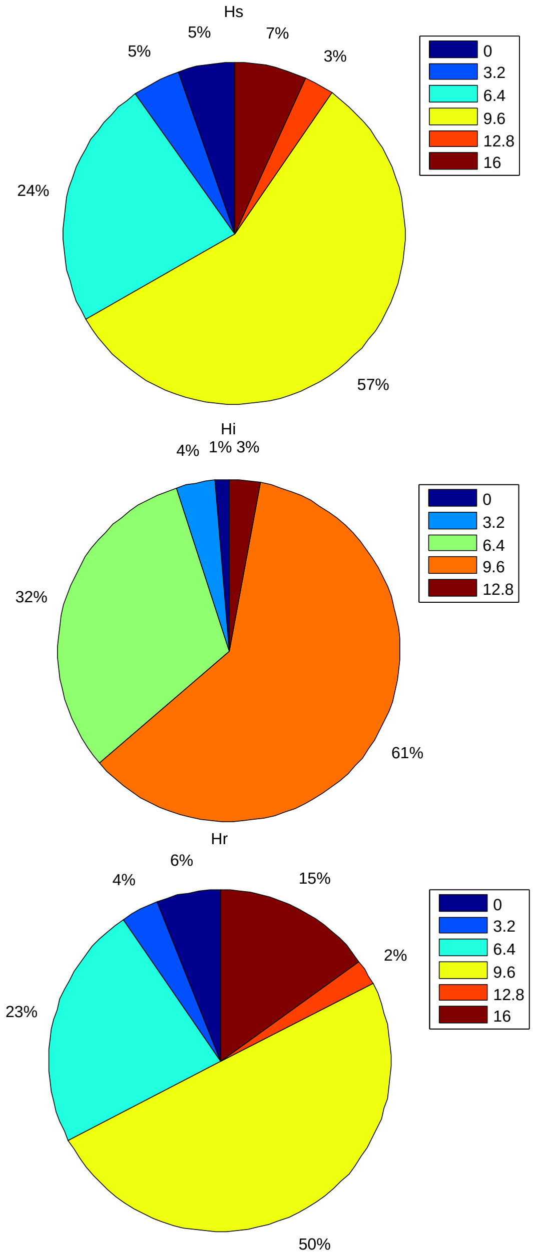

Figure A.18: Percentage of different H_s, H_i and H_r.

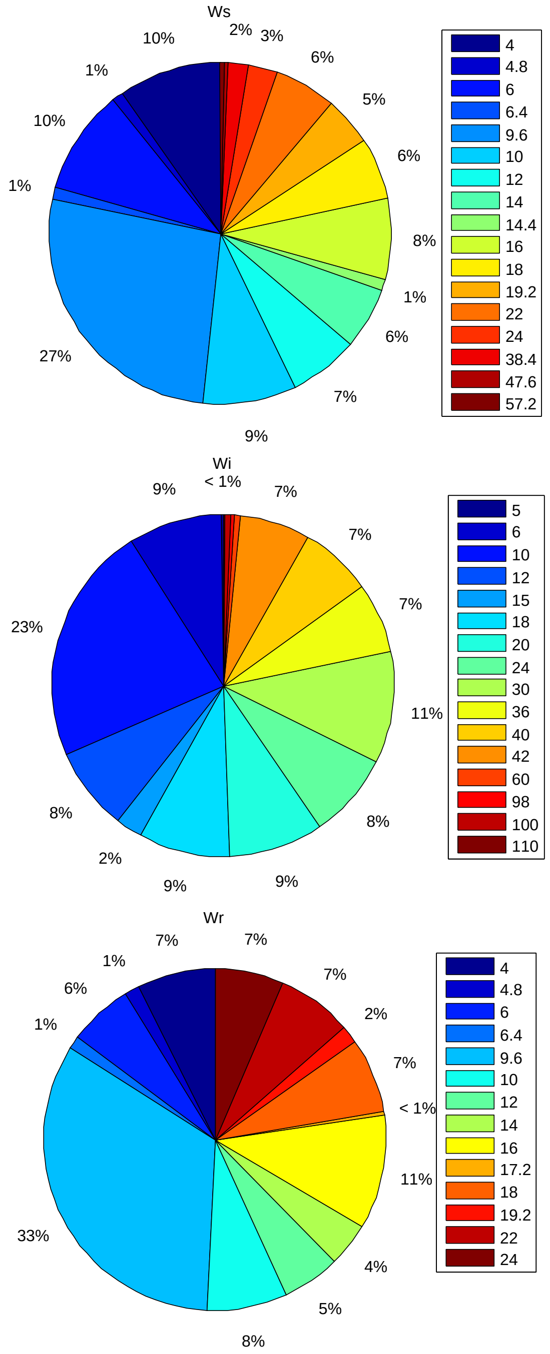

Figure A.19: Percentage of different W_s, W_i and W_r.